Compressed Air Energy Storage and its Application in Solar Photovoltaic Efficiency Improvement

by

Marcus King

A thesis submitted in partial fulfilment of the requirements for the degree of

Doctor of Philosophy in Engineering

School of Engineering

University of Warwick

July 2022

Table of Contents

List of Figures

List of Tables

Acknowledgement

I would like to express my deep appreciation towards my supervisor Professor Jihong Wang for her guidance throughout my research, as well as the financial support that she provided that allowed the completion of my research and thesis. I am immensely thankful for the opportunities that she has generously provided and encouraged.

I would additionally like to express my gratitude to Dr Dacheng Li for his expertise and assistance in technical matters that aided the project; his advice and feedback was greatly valued.

Furthermore, I extend my thanks to Dr Oleh Kiselychnyk, Dr Wei He, Dr Mark Dooner as well as my fellow PhD students within the Power and Control Systems Research Laboratory for their support throughout my research. In addition to technical guidance, their friendly and warm nature ensured that undertaking my research was a wholly enjoyable experience.

I would like to acknowledge EPSRC and the University of Warwick School of Engineering for the studentship that allowed me to pursue a PhD and finally, I would like to thank the organisers of the Joint UK-India Clean Energy Centre project that provided funding so that I could undertake a placement at the Malaviya National Institute of Technology in Jaipur, India to progress my research.

Marcus King

July 2022

Declaration

This thesis is submitted to the University of Warwick to support the author's application for the degree of Doctor of Philosophy. The work contained in this thesis has not been previously submitted to any university for the application of any degree. The work contained within this thesis has been carried out entirely by the author, Mr Marcus King, under supervision by Prof. Jihong Wang.

Published Work Arising from Thesis

Sections of this thesis have been previously presented in peer-reviewed publications; the published papers that contribute work to included thesis chapters are listed here:

M. King, A. Jain, R. Bhakar, J. Mathur, J. Wang, "Overview of current compressed air energy storage projects and analysis of the potential underground storage capacity in India and the UK" in *Renewable and Sustainable Energy Reviews,* vol. 139, pp. 110705, 2021.

D. Li, **M. King**, M. Dooner, S. Guo, J. Wang, "Study on the cleaning and cooling of solar photovoltaic panels using compressed airflow" in *Solar Energy,* vol. 221, pp. 433-444, 2021.

M. King, D, Li, M. Dooner, S. Ghosh, J.N. Roy, C. Chakraborty, J. Wang, "Mathematical Modelling of a System for Solar PV Efficiency Improvement Using Compressed Air for Panel Cleaning and Cooling" in *Energies,* vol. 14(14), pp. 4072, 2021.

M. King, D. Li, M. Dooner, J. Wang, "Modelling and control of the charging process of a PV-compressed air system for efficiency improvement from panel cleaning and cooling" in *Automation and Computing (ICAC), 2021 26th International Conference on*, 2021.

Where chapters contain previously published material, it is indicated in the introduction of the respective chapter.

Patent

Furthermore, a patent, titled '*Compressed Air Energy Storage (CAES) based self-powered active cleaning and cooling system for solar photovoltaic panels*' has been applied for, by the author, supported by work contained within the thesis. The patent is under review by the UK patent office at the time of thesis submission.

Additional Author Contributions to Published Work

The author has also contributed to the following peer-reviewed publications throughout the PhD period of study, though none of the material within these works are submitted as part of the final thesis:

W. He, M. Dooner, **M. King**, D. Li, S. Guo, J. Wang, "Techno-economic analysis of bulk-scale compressed air energy storage in power system decarbonisation" in *Applied Energy,* vol. 282, pp. 116097, 2021.

D. Li, S. Guo, W. He, **M. King**, J. Wang, "Combined capacity and operation optimisation of lithium-ion battery energy storage working with a combined heat and power system" in *Renewable and Sustainable Energy Reviews,* vol. 140, pp. 110731, 2021.

S. K. Mitra, S.B. Karanki, **M. King**, D, Li, M. Dooner, O. Kiselychnyk, J. Wang, "Application of Modern Non-Linear Control Techniques for the Integration of Compressed Air Energy Storage with Medium and Low Voltage Grid" in *Energies,* vol. 14(14), pp. 4097, 2021.

W. He, **M. King**, X, Luo, M. Dooner D. Li, J. Wang, "Technologies and economics of electric energy storages in power systems: Review and perspective" in *Advances in Applied Energy,* vol. 4, pp. 100060, 2021.

Abstract

As the penetration of power generation from renewable energy sources in electrical grids increases, the challenges of system stability and uncertainty are exacerbated. Electrical Energy Storage (ESS) provides an energy buffer to detach the power generation and usage and is regarded as one of the foremost solutions to mitigate the effects of the increasing adoption of variable renewable energy technologies. Within competing EES technologies, Compressed Air Energy Storage (CAES) is an established solution for providing large-scale, long-duration energy storage. The work presented in the thesis explores the potential of using CAES to support power generation from renewable energy sources and to develop a new technology for improving energy conversion efficiency through EES integration.

CAES uses high-pressure air as its working medium and therefore possesses low energy storage density, leading to the requirement of large storage volumes for high-capacity systems. The research begins with an assessment of the suitable underground storage resources for CAES in the UK and India. A geographic study of Indian renewable generation potential and CAES geological resource distribution establishes the limitations for India to adopt the technology, even though the total storage capacity is shown to be sufficient to meet the Indian EES requirements; there are limited regions where there is coincidence between renewable generation potential and CAES suitability. This analysis provides essential information for evaluating economic viability in formulating the suitable energy strategy of exploitation of CAES in different countries.

In addition to CAES acting as a buffer to aid intermittence of renewable power generation, this thesis proposes a new integrated PV-CAES system, whereby high-pressure air of a CAES system can be utilised as a secondary resource for panel cleaning and cooling. High-pressure air is directed to the PV panel surfaces through a series of pipes and nozzles, with the action of air release across the panel at a high velocity removing present dust and lowering the panel operating temperature through convective effects. The whole system dynamic model is established through deriving individual mechanism and component mathematical models. The model provides a valuable tool for analysing the soiling mechanisms, cleaning and cooling effect and their relationship with air flow and key parameters of system design.

A laboratory test rig is constructed for model verification and for a feasibility investigation of utilising high-pressure air to improve PV generation efficiency through cleaning and cooling. The validated system model is then utilised in a study to inform a system operation strategy. The results indicate that the efficiency of PV generation can be improved using CAES for cleaning and cooling, however only cleaning effects have a beneficial impact when considering energy required for the CAES system operation.

List of Abbreviations

A-CAES	Adiabatic Compressed Air Energy Storage
CAES	Compressed Air Energy Storage
CSP	Concentrating Solar Power
D-CAES	Diabatic Compressed Air Energy Storage
EB	Electrochemical Battery
EDS	Electrodynamic Dust Shield
EES	Electrical Energy Storage
FB	Flow Battery
FES	Flywheel Energy Storage
GES	Gravity Energy Storage
HES	Hydrogen Energy Storage
HEX	Heat Exchanger
I-CAES	Isothermal Compressed Air Energy Storage
I-V	Current-voltage
LCOE	Levelised Cost of Electricity
LRC	Lined Rock Cavern
MPP	Maximum Power Point
MPPT	Maximum Power Point Tracking
PCM	Phase Change Material
PHS	Pumped Hydroelectric Storage
P&O	Perturb and Observe
PMSM	Permanent Magnet Synchronous Motor
PtG	Power to Gas

PV	Photovoltaic
PV-T	Photovoltaic-thermal
P-V	Power-voltage
SEM	Scanning Electron Microscope
TEM	Thermoelectric Module
TES	Thermal Energy Storage

Chapter 1 – Introduction

1.1 Background

The average global temperature has increased at a rate of 0.18°C per decade since 1981 [1], with Earth's surface temperature projected to continue to increase in the coming decades. A significant contributor to the rapid rate of warming in the global temperature is the combustion of fossil fuels for electrical power generation. It is estimated that between 20-30% of global greenhouse gas emissions are directly attributable to electrical power generation [2–4].

As a greater understanding and awareness of the negative impacts of global warming permeates nations worldwide, actions are being taken to address the impacts of climate change. In 2015, 196 parties signed the Paris Agreement and agreed to be bound to a target-limit of a global rise in temperature of 1.5°C compared to pre-industrial levels [5]. To meet these aims, many nations are transitioning away from conventional thermal power plants combusting fossil fuels, to renewable electrical power generation. However, as this process occurs the balance between power supply and load demand in electrical grids becomes more complex. Energy storage systems are considered as one of the feasible solutions to aid this shift, as they provide energy buffers to detach power generation and the time of use. Large-scale energy storage systems allow for the storage of surplus electrical generation from renewable sources, in times of high availability but low demand, with this stored energy supplying the grid during periods of low available generation but high demand. Compressed air energy storage (CAES) is one of the most promising, suitable and established technologies for large-scale and long-duration energy storage. However, a limitation of CAES is the low energy storage density of the medium, compressed air. Because of this, to generate high-capacity systems, large storage volumes are a necessity. Utilising underground formations is the most feasible method of creating these large volumes. However, in many instances, there is a lack of information pertaining to geological features suitable for the forming of CAES caverns; this provides motivation for the initial presented work.

Of the available renewable power generation technologies, solar photovoltaics (PV) are experiencing rapid growth in worldwide installed capacity. In 2020, PV accounted for 39% of all additions to generation capacity [6]. However, solar PV are subject to numerous sources of inefficiencies, primarily panel soiling and temperature effects. Panel soiling and heating are compounded as locations with a significant solar resource tend to be hot and arid environments where dust is also prevalent. With an increasing number of large-scale solar power plants being constructed in arid environments, cleaning panels to maintain efficiency is extremely challenging with no access to convenient water sources [7].

The research presented in this thesis explores the potential benefit to PV generation that CAES can provide, firstly by a quantification of capacity for CAES through and examination of underground features and proximity to renewable electrical power generation potential in India and then through the investigation of a proposed novel-integrated PV-CAES mechanism, whereby the CAES system can be used for panel cleaning and cooling. The secondary resource that is the high-pressure air used as the energy storage medium can be used to blow over the surface of PV panels, to remove adhered particles and cool the panels to improve the overall generation efficiency.

1.2 Objectives

The aim is to investigate the potential of using CAES to support power generation from renewable energy sources. Furthermore, this thesis aims to investigate the benefits to PV generation efficiency by the proposal of a novel integrated PV-CAES mechanism. Therefore, the inefficiencies introduced to PV generation from panel soiling and high temperatures, in addition to the promising potential to ameliorate these issues through the integration of CAES provided the motivation for the research. The primary aim of the research is to investigate the novel PV-CAES system for panel cleaning and cooling to assess the feasibility of such a system and the potential benefit to PV generation be achieved. A dynamic mathematical model will be derived and validated which can then be used for a wider study of the system.

1.3 Thesis Structure

The thesis proceeds with the following structure:

Chapter 2 introduces electrical energy storage technologies and their benefits to renewable power generation, with a focus on CAES. Methods for the underground storage of compressed air are reviewed and a geographical study of the underground storage potential for CAES in India is conducted and compared with renewable electrical power generation potential; these results are compared with the potential for CAES utilisation in the UK.

Chapter 3 specifies PV power generation and the issues arising from panel soiling and temperature effects. Current strategies for addressing these challenges are reviewed and a novel technological solution of integrating CAES with PV generation for panel cleaning and cooling is introduced and outlined.

Chapter 4 derives a dynamic mathematical model of the key mechanisms in the proposed PV-CAES system. These are PV panel generation, panel temperature modelling for natural and forced convective heat transfer, particle adhesion and detachment mechanisms from air blowing, the soiling losses from particle deposition and compressed air system mechanisms. The chapter concludes with the presentation of a control strategy for the charging process of the PV-CAES system using the developed dynamic mathematical model.

Chapter 5 describes the experimental test rig that has been designed and constructed to validate the mechanisms outlined in the modelling study. The test rig is used to assess the feasibility of using compressed air for the cleaning and cooling of solar PV panels. The hardware, instrumentation and test-rig control system are explained.

Chapter 6 presents experimental results and the mechanisms introduced in the modelling study are validated. The validated mathematical model is subsequently used to demonstrate the potential for the PV-CAES system in improving the power generation because of reduced losses from soiling and heating and an overall system performance analysis is conducted.

Chapter 7 concludes the work presented in the previous chapters and provides recommendations for additional work for the continuation of the project.

Chapter 2 – Overview of Electrical Energy Storage and Analysis of Compressed Air Energy Storage Potential in the UK and India

In this chapter, electrical energy storage (EES) systems are introduced and their roles in mitigating against the intermittency, variability and uncertainty in renewable generation are highlighted. Key EES technologies are discussed with a focus on compressed air energy storage (CAES). Recent major CAES projects are highlighted and mechanisms for creating large-capacity CAES systems utilising underground reservoirs are introduced. Finally, an assessment of the potential for underground CAES capacity for India and the UK is conducted and areas are identified where CAES integration can most benefit renewable power generation in India through a proposed methodology.

This chapter is largely based upon the published work "*Overview of current compressed air energy storage projects and analysis of the potential underground storage capacity in India and the UK*" published in Renewable and Sustainable Energy Reviews by the author, M. King, and A. Jain, R. Bhakar, J. Mathur and J. Wang [8].

2.1 Overview of Current Development in Electrical Energy Storage Technologies

Renewable electrical power generation methods are dependent upon a natural resource as their primary source of energy, predominantly the sun and wind. This greatly effects the characteristics by which they operate when compared to conventional thermal generation. Firstly, there is a high degree of variability in the availability of the primary energy source across several timescales, from instantaneous changes to regular daily and seasonal variability. Furthermore, although forecasters make attempts to predict the future sun and wind availability, there remains a large amount of error in forecasts, compounding the variable nature of renewable generation. Another result of the dependence on natural resources is the discrepancy between good renewable generation potential and the local demand for power. For example, high potential renewable generation areas, such as offshore locations for wind power, or deserts for solar power, typically do not possess large urban areas with high power demands in proximity to them. These factors: variability, uncertainty and location restraints, make the operation of grids with a high proportion of renewable generation more difficult to manage.

To ensure stability and a constant operating frequency, power generation must follow demand in electrical grids. However, the aforementioned variability and uncertainty of renewable generation threatens stability with power shortfalls, because of instantaneous lack of power, or leads to curtailment and loss in potential generation, because there is no instantaneous demand for power.

Implementing electrical energy storage (EES) technologies, is seen as one of the most promising solutions to mitigate the challenges imposed by renewable generation. Electrical power, in times of high renewable generation but no demand, can be stored and used to supply the grid during periods when potential generation has dropped but demand has increased. The alleviates some uncertainty of renewable generation and reduces the amount of curtailment required as all available renewable generation potential can be harnessed.

At present, there are a multitude of viable technologies for storing large quantities of energy at the grid level, varying greatly in maturity, scale, response time, storage duration and cost. The most investigated EES technologies are introduced here.

2.1.1 Technologies for Electrical Energy Storage

2.1.1.1 Pumped Hydroelectric Storage

The EES technology that has experienced the widest implementation in electrical grids is Pumped Hydroelectric Storage (PHS) [9], accounting for 93% of all implemented EES at present [10]. In PHS systems, energy is stored in the form of gravitational potential energy by pumping water between reservoirs at different elevations. Electrical power is regenerated when water in the elevated reservoir is allowed to flow down to the lower reservoir, through a turbine, which drives a generator. A typical PHS system can be seen in Figure 2-1. PHS systems currently demonstrate the largest achievable power ratings and storage capacity of feasible EES systems. Implementation of PHS in developed nations is becoming limited by the availability of suitable locations for forming the necessary reservoirs [11]. Furthermore, environmental damage caused by the construction and operation of PHS remains of concern.

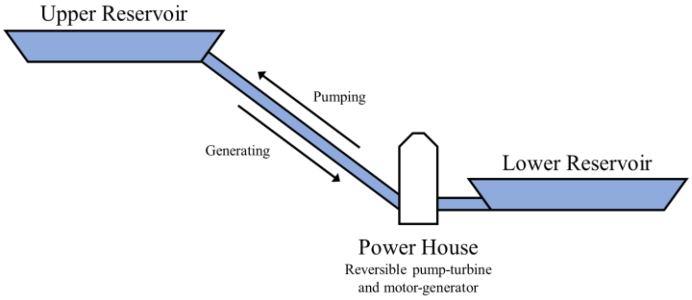

Figure 2-1. PHS plant operation

2.1.1.2 Compressed Air Energy Storage

Compressed Air Energy Storage (CAES) has been implemented at the grid level for over 40 years [12], with two such CAES facilities operational at present, the Huntorf plant, in Germany, constructed in 1978, and the McIntosh plant, Alabama, USA, operational from 1991 [13]. These can be seen in Figure 2-2[1].

(a) **(b)**

Figure 2-2. Huntorf CAES plant, Germany, commissioned 1978 [14] **(b) McIntosh CAES plant, Alabama, USA, commissioned 1991** [15]

The complete cycle of conventional CAES operation is comprised of two processes, the charging and discharging processes. During the charging process, electricity from the grid is used to power a motor, which drives a turbine or series of turbines, compressing air into a large underground cavern as the heat of compression is rejected to the environment [16]. Later, during the discharging process, the high-pressure air from the storage cavern is mixed with gas and combusted to drive a turbine or series of turbines. This work is used to drive an electrical generator with the produced electricity supplied to the grid. Because of the rejection of heat and the necessity for an external heat source during the expansion stage, this CAES implementation is referred to as D-CAES (diabatic-CAES).

---

[1] The key technical characteristics of the Huntorf and McIntosh CAES plants are contained within Appendix A

The typical configuration of conventional D-CAES systems is given in Figure 2-3. The rejection of heat and necessity of the fuel input requirement in D-CAES during the discharging means overall efficiencies of traditional D-CAES systems are relatively low and is one of the main constraints of CAES as a storage option. Efficiencies of D-CAES systems can be improved significantly with the integration of recuperators, as in the McIntosh plant, in which the hot exhaust gas during the compression stage is directed to preheat the pressurised air from the cavern prior to the expansion stage [17]. This greatly reduces the thermal energy input required and results in improved efficiencies with less fuel consumption [18].

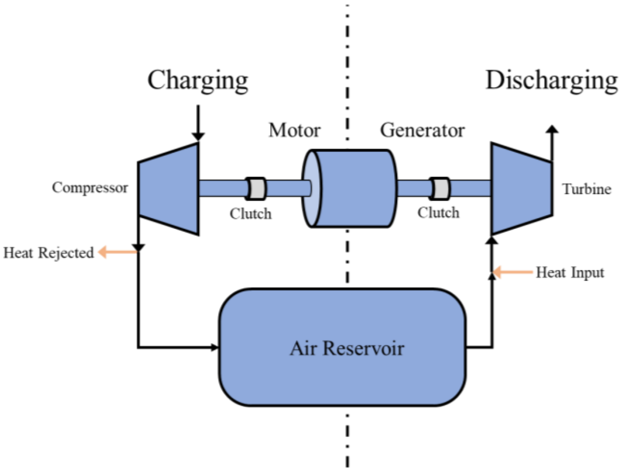

Figure 2-3. D-CAES operation principle

CAES possesses advantages over competing large-scale energy storage systems, excelling in technology lifetime, energy storage duration, possessing negligible self-discharge, as well as being scalable in terms of capacities and power output. Albawab et al. compared large-scale energy storage technologies across a wide range of factors to determine the overall sustainability of the competing technologies with CAES outperforming the other candidates [19]. Moreover, under current conditions in the United States market, CAES has been shown to be the most economically attractive grid-integrated energy storage technology, along with PHS, both in terms of cost per kW and cost per kWh [20].

However, aside from the relatively low efficiencies when compared to other established energy storage technologies, the greatest limitation of CAES as a large-scale energy storage technology is the low energy storage density. CAES energy density is comparable to PHS systems but is an order of magnitude smaller than existing energy storage technologies that are beginning to be implemented at the grid level, particularly electrochemical batteries (EB). Owing to the low energy storage densities, large storage volumes are required to create systems with large capacities. At present, the most viable option for constructing chambers with sufficient volumes is the use of underground storage caverns. Although over-ground manufactured storage vessels can be used for the implementation of small-scale CAES with very high pressures [21] or for demonstration plants, large capacity systems cannot be constructed in this manner. The use of underground storage also provides the benefits of isolation from external influences, with the only surface features being connecting valves, and much lower specific costs for storage capacity when compared to the use of above-ground tanks [22]. Therefore, the availability of suitable geographic features for the formation and locations of underground storage caverns are the major constraint to the rate of adoption of CAES as a bulk energy storage technology.

2.1.1.2.1 Adiabatic CAES

A progression of the use of recuperators is the emergence of Adiabatic CAES (A-CAES). In A-CAES systems, heat rejected during the compression stages is stored in a thermal energy store (TES) and used to heat the compressed air before expansion. Therefore A-CAES systems can achieve higher system efficiencies, up to 80% expected to be achievable [23,24] with no external heat from the combustion of a fuel. TES are the limiting factor in the progression of A-CAES because of the high temperatures that are generated during compression, which are difficult to store [25]. Thermal energy is traditionally stored in the form of sensible heat or latent heat: Sensible heat stores are a mature technology and economically attractive but latent heat technologies can store higher temperatures and achieve better system efficiencies [26]. There are examples of attempts to integrate chemical and thermochemical heat storage into CAES systems, though at present these are economically unattractive under the current technological state [27]. A representation of an A-CAES system is given in Figure 2-4.

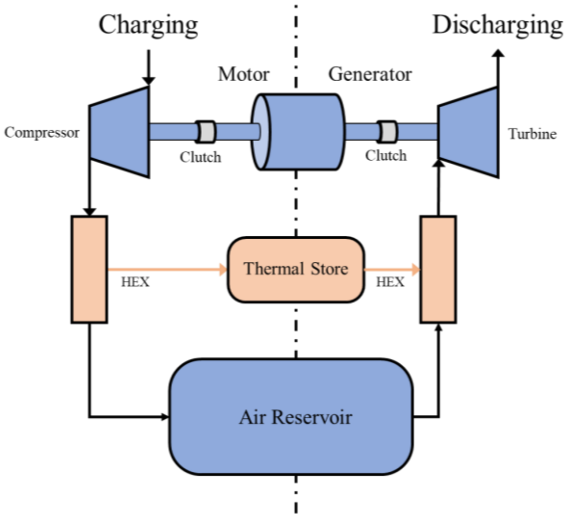

Figure 2-4. A-CAES operation principle

2.1.1.2.2 Isothermal CAES

Although the progression of CAES as an EES is trending towards improving A-CAES systems, a competing approach to improve round trip efficiencies of conventional CAES facilities is the development of isothermal-CAES (I-CAES) [28]. When traditional turbomachinery is employed for compressing air to high pressures, very high temperatures are achieved and as a result the air cannot be practicably stored, thus heat must be rejected, cooling the air and energy is lost. Conversely heat must then be added to the system at the expansion stage to account for this. I-CAES systems aim to achieve slow compression and expansion such that these processes occur at a constant temperature. This requires continuous heat transfer during the compression and expansion stages but could result in considerably higher round trip efficiencies and additionally removes the requirement of a secondary TES. The most demonstrated methods of achieving the necessary slow expansion and compression are through the use of liquid pistons or hydraulic pumps [29,30].

2.1.1.3 Gravity Energy Storage

Similar to PHS, in Gravity Energy Storage (GES), electrical energy can be stored as gravitational potential energy but with a solid object being the mass that is moved to a higher elevation rather than water. A motor provides the work to elevate the mass, then the mass can be allowed to fall to a lower altitude and convert the potential energy to electrical power with the motor now acting as a generator; this is represented by Figure 2-5. There have been different implementations of this technology at the pilot scale with systems working upon hill-based rail carts moving up and down an elevated profile [31], lift-based systems with masses moving vertically up and down tracks [32] and crane-based systems with suspended masses inserted in boreholes allowing a large variation in mass altitude [33]. GES has not been widely adopted in electrical grids and is limited to a small number of pilot plants attempting to demonstrate the feasibility of the solution. The greatest advantage of GES as a storage solution appears to be the storage duration, which theoretically could be indefinite with negligible losses over a long period of time.

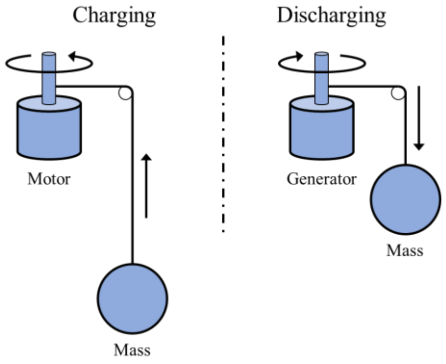

Figure 2-5. GES operation principle

2.1.1.4 Flywheels

Flywheels or Flywheel Energy Storage (FES) can be used to store electrical energy as kinetic energy, proportional to the moment of inertia and rotational velocity of a spinning disc. An integrated motor-generator is used to accelerate a disc and then is disengaged via a clutch. The key features of an electricity storing flywheel is shown in Figure 2-6. The motor-generator can then be reengaged and is driven by the rotating disc to produce electricity. FES are highly efficient with up to 95% system round trip efficiencies, excellent response times and good cycling capabilities [34]. However, current systems cannot be employed as bulk storage technologies owing to poor scaling. Also, flywheels cannot be used to store energy over long periods because of high self-discharge rates. FES for electricity storage employ magnetic bearings and vacuum casings to reduce friction losses but still are limited to a maximum of a few minutes of discharge. Consequently, applications of flywheels best lie in transport systems (primarily in energy recovery), uninterruptable or back-up power supplies, as well for the potential of power stabilisation and smoothing for short term variability in renewable generation [35]. The case for flywheels as a bulk energy storage solution is therefore restricted though may prove vital in small-scale distributed generation systems.

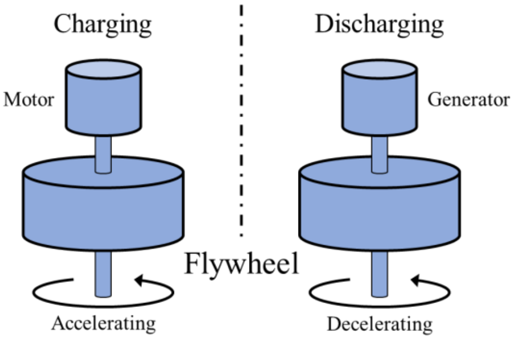

Figure 2-6. FES operation principle

2.1.1.5 Electrochemical Batteries

Electrochemical batteries (EB) have fallen in cost rapidly in recent years, driven by developments in electric vehicles and consumer electronics. As such they are increasingly being implemented as a large-scale store of electrical energy. Electricity is stored in the form of an electrochemical potential between two electrodes connected by an electrolyte to facilitate ion transfer. A schematic of a conventional lithium-ion battery is demonstrated in Figure 2-7. The total installed capacity of grid connected EB arrays now stands at approximately 1 GW [36], the most dominant type of which being lithium ion, with lead-acid, nickel-cadmium and sodium-sulphur cells having all been suggested for large-scale use [37]. The scale of individual EB arrays has additionally increased rapidly in recent years, for example, the largest completed EB facility in 2017 was capable of supplying 100MW for 3 hours [38], by 2021, the largest battery facility can deliver 400MW for 4 hours [39]. The response times of EB are excellent, although EB technologies are limited by the short lifespan, materials required for manufacture, self-discharge and end of life concerns. Furthermore, even though the scale of individual plants is increasing, they are still not as large as existing PHS or CAES systems. Therefore, EB technologies may show greater promise as a technology for integration with distributed generation and storage, for example in Vehicle-to-grid systems [40].

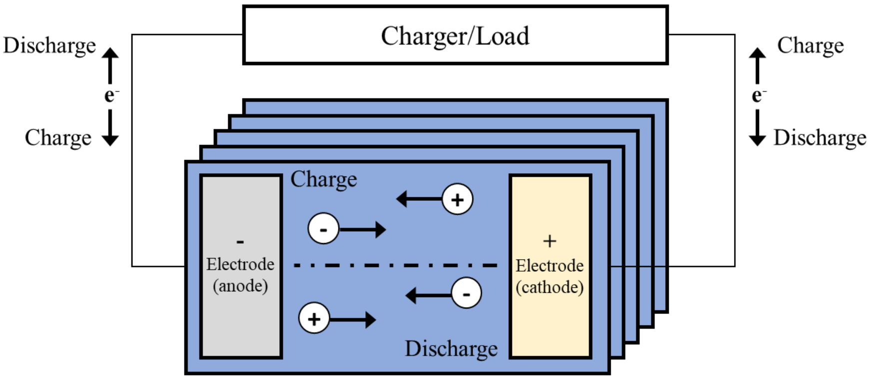

Figure 2-7. EB schematic

2.1.1.6 Flow Batteries

Flow batteries (FB), similarly to EBs, store energy as a difference in electrochemical potential between two electrodes. The main difference being that in FB, two aqueous electrolytic solutions are contained in separate tanks and connected by a circulating electrolyte; in contrast EBs contain internal solid electrodes and an electrolyte. A schematic demonstrating the operating principles of flow batteries is given in Figure 2-8. When compared to EBs, flow batteries excel in lifespan and scalability, with self-discharge presenting a negligible problem as flow batteries can also be fully discharged without impacting the life span of the cells. However, at present flow batteries are substantially more expensive than conventional batteries [41] and other grid scale storage technologies, partly owing to the requirement of mechanical circulating pumps and compounded by the previously lacking widespread applications. Flow batteries also rely upon expensive metals as the active species in the electrolytes (typical to vanadium redox batteries, zinc bromide batteries and polysulphide bromide batteries) [37]. Thus, similarly to EB, flow batteries demonstrate promise at a medium to large-scale if these limitations can be eradicated.

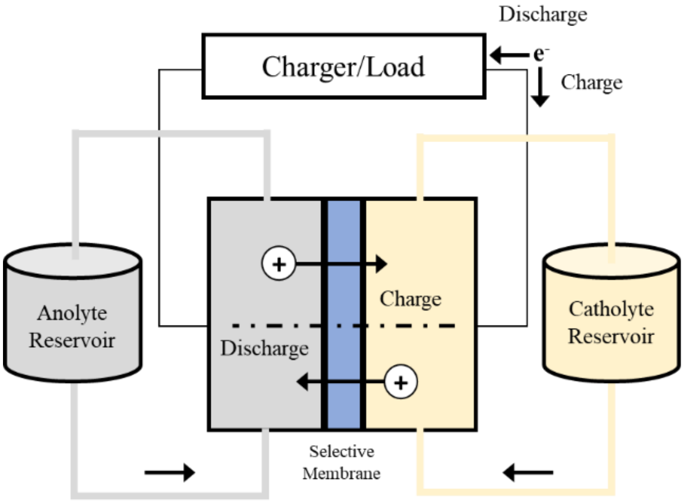

Figure 2-8. FB schematic

2.1.1.7 Hydrogen Energy Storage and Power to Gas

There has been significant attention on utilising Hydrogen Energy Storage (HES) or Power to Gas (PtG) to balance electrical grids. Proponents suggest that excess electrical power can be used to synthesise hydrogen or synthesise methane. These secondary fuels can then either be converted back into electrical power via fuel cells, used in turbomachinery to power conventional thermal plants or used as a fuel for separate processes such as transportation. Fuel cells are the primary technology used for the synthesis of hydrogen from water and can also operate by consuming hydrogen to generate electricity. Fuel cell technologies are relatively mature and possess good scalability from the kW to hundreds of MW power level. Furthermore, hydrogen can be stored for long durations, exceeding months, so presents a promising solution when considering inter-seasonal storage [42]. Lack of practical large-scale demonstration and the practicality of the storage of hydrogen remain a challenge [43].

Similarly, methane can be synthesised from hydrogen, thus can be deemed as a potential EES. Many nations already possess natural gas storage infrastructure, so practical storage challenges present less of an issue. The synthesis of methane therefore could be a viable solution for introducing a load for grid balancing. The produced methane is a highly energy dense fuel that can be employed in a range of applications. Several pilot studies have been conducted to assess the possibility of large-scale applications, but to date, PtG is not widely practiced [44]. If synthesised methane is still used in natural gas power plants, this will be a contribution to greenhouse gas emissions and overall climate change.

2.1.1.8 Discussion of Electrical Energy Storage Technologies

The predominant characteristics of an EES technology is its capability for power and capacity. A comparison of these parameters for the presented EES technologies is given in Figure 2-9.

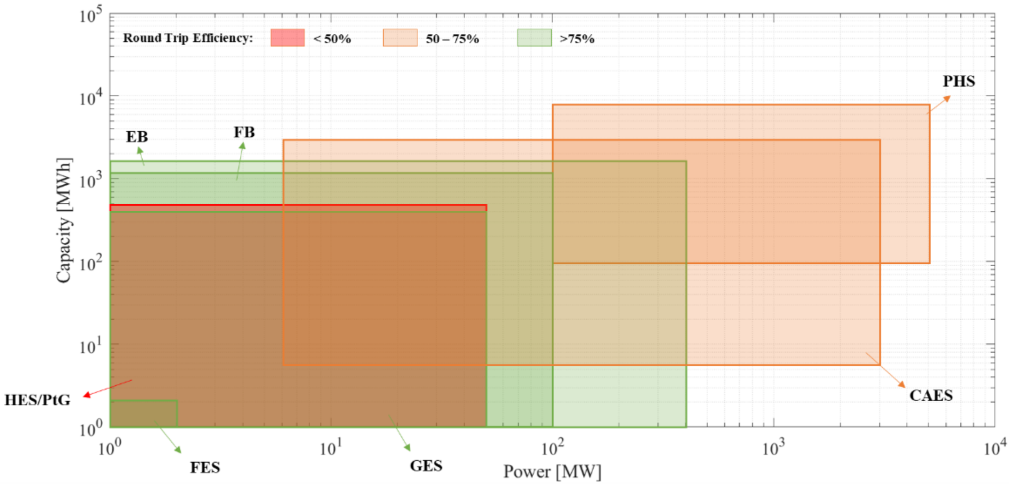

Figure 2-9. Comparison of EES technologies [45–47]

At present, the two technologies that are capable of the largest power ratings and storage capacities are PHS and CAES, both also possessing very good ranges in power and capacity from mid-to-large capacity for PHS and small-large for CAES systems. EB are beginning to compete in terms of storage capacity in the mid-range in terms of power and capacity. Aside from power and capacity, important factors in the operation of EES are the storage duration, the operational life of the system, the self-discharge rate, round trip efficiency and response time. Additionally, there is great importance of the power and capacity density of the EES technology. The key metrics of each discussed EES technology are given in Table 2-1.

With the long storage durations that CAES systems possess, up to the month timescale, CAES is one of the best suited technologies for inter-seasonal storage. Storage of large amounts of energy across long durations will be essential for countries with high penetration of renewables in their grids and high seasonal weather variability, so that summer surplus of power can be stored to meet the winter shortfall. EES technologies with short storage durations cannot meet the demand for seasonal storage and are better suited for frequency regulation. Additional system lifespans of CAES systems are good when compared to competing ESS, this affects the overall economic viability of the plants as well as simplicity in long term planning.

Efficiencies and energy densities remain a limiting factor of CAES systems, where efficiencies are attempting to be improved through the development of A-CAES and I-CAES. Low efficiency limits the economic viability of CAES systems and also the associated carbon emissions with lost power generation. Batteries are emerging at the large-scale, but required materials necessary for fabrication remain an issue as well as short lifespans also presenting a challenge.

.

Table 2-1. Comparison of EES technologies [9,13,16,18,23,45–47]

Technology	**Power [MW]**	**Capacity [MWh]**	**Storage Duration**	**System Lifespan [year]**	**Self-discharge [%]**	**Efficiency [%]**	**Response Time**	**Energy Density [Wh l^{-1}]**	**Power Density [W l^{-1}]**
PHS	100-5000	100-8000	hour-month	40-60	0	65-85	minutes	0.13-0.5	0.01-0.12
CAES									
D-CAES	5-3000	5-2860	day-month	40	0	42-54	minutes	2-5	0.5-2
A-CAES	1-1000	10-1000	day-month	40	>0[2]	80[3]	minutes	0.5-20	0.5-2
I-CAES	1-1000	10-1000	day-month	40	0	80[3]	minutes	1-25	0.5-2
FES	0.001-20	0-1	second-minute	15-20	1.3-100	75-95	milliseconds-seconds	20-80	1000-2000
EB	0-400	0-1600	minute-day	5-15	0.5-20	70-95	milliseconds	100-500	1500-10000
FB	0-100	0.2-1200	hour-month	5-20	0.2	60-85	milliseconds	16-30	<2
GES	0-50	0.25-480	hour-month	25-50	0	75-90	seconds	2-5	3
HES/PtG	0-1	0-600	day-month	20+	0-4	25-45	seconds	500-3000	>500

---

[2] The self-discharge of A-CAES facilities is dependent on the capability of the TES.

[3] The figures are estimated as these results have not been demonstrated/reported at present.

2.2 Assessment of Recent Major CAES Projects

Owing to the highlighted benefits of CAES systems, and as a long-established large-scale energy storage technology, there has been continued interest in the development of CAES since its first demonstration. Consequently, there have been numerous major CAES projects, commercial or demonstrations in recent years, which are given in Table 2-2.

- The Norton CAES facility was a proposed project of up to 2700 MW, planned to be developed in Norton, Ohio repurposing a disused limestone mine as the storage method. The project suffered setbacks for a number of years and was finally discontinued in 2013. Regarding innovations, the Norton project did not advance CAES technology significantly as all planned implementations of technologies were pre-established, key lessons were learnt however, regarding the management and economics of large-scale energy storage developments [48,49] .
- Another long planned commercial CAES project that has ultimately been abandoned, was a plant in County Antrim, Northern Ireland. The facility was again planned to utilise conventional D-CAES methods as well as employing a salt cavern as the air store. Designed to deliver 330MW for up to 6 hours, the project was awarded €90m from EU funding, though the company, Gaelectric, went into liquidation in 2017 and no buyer was found [10] with the planning application subsequently withdrawn and no substantial developments arising from the project.
- Between 2010 and 2012, the New York State Energy Research and Development Authority (NYSERDA) aimed to achieve a 130 MW to 210 MW CAES facility in upstate New York, dubbed the Seneca CAES Project. The site was deemed to be feasible because of the local salt mining operations and on-site high-pressure natural gas pipeline that could be directly used in the D-CAES plant [50]. The initial plan was comprised of 3 phases. Phase 1 involved siting, design, financials and filings. Phase 2 was to be construction and Phase 3 was to be commercial demonstration and performance reporting. However, a number of factors led to increased projected necessary investment which resulted in the project ultimately being discontinued at the end of the first phase, citing lack of economic incentive [51].
- The ADELE project, based in Staßfurt, Germany, aimed to be the first large commercial demonstration of A-CAES technology at the grid level. As with the previous CAES projects, salt caverns were planned to be used as the underground

air store, but with the addition of a large sensible heat store to capture and reinject the heat of compression. The project was designed to deliver 200MW up to 5 hours with a 70% round trip efficiency. The project was placed on hold in 2016 citing uncertain business conditions and no further updates have been published [52].

- The Bethel Energy Centre is a commissioned CAES facility in Anderson County, Texas [53] developed by APEX CAES. The project is planned to incorporate conventional D-CAES technology, utilising underground salt caverns with gas as the heat source at the expansion stage. The proposed system power is 324MW, deliverable for up to 48 hours. At the time of writing, the facility is fully permitted and construction ready and planned to be operational by 2022.
- Another proposed large-scale conventional CAES project was the Advanced Underground CAES facility from PG&E planned for San Joaquin County, California [54]. The facility aimed to deliver 300 MW and utilise a depleted gas reservoir. The project was outlined for three phases, although concluded at the end of the first because of uncompetitive economic conditions [55]. However, the project demonstrated the feasibility of using depleted natural gas reservoirs for CAES systems.

In contrast to the implementation of existing CAES technologies in new plants, novel CAES methods are being developed and tested:

- Hydrostor are a promising company that have demonstrated a unique type of CAES at the grid level. A commercial reference facility in Goderich, Canada became operational in 2019, rated at 1.75MW [56]. Air is stored in a specially excavated underground cavern that can be partially flooded by a surface water reservoir. This ensures constant air pressure throughout the process as the chamber volume can vary in size through the partial flooding. Additionally, the heat of compression is captured, stored and later reinjected making the system a demonstration of adiabatic CAES. Hydrostor are a fast-moving company, with a number of smaller and failed demonstration projects [57].
- The only megawatt-scale demonstration of isothermal CAES in recent years has been from SustainX. The company designed and tested a 1.5MW commercial scale prototype of a novel isothermal CAES system. The processes were based upon the compression and expansion of a foam-air mixture to facilitate fast heat

transfer and maintain constant temperature throughout [58]. The system realised round trip efficiencies of 54% a significant improvement upon D-CAES. A limitation of the scalability of the prototype is that specially constructed above-ground air vessels were used as the storage medium and it is unclear whether this technology could be adapted to be integrated with larger underground storage methods. This is compounded also because SustainX has subsequently been acquired by GeneralCompression who and have divested in research in above ground CAES solutions with the future of this technology being unclear [59].

- A pilot plant for an A-CAES system is has been demonstrated by ALACAES near Biasca, Switzerland [60]. The system uses an excavated mountain tunnel and the focus of the research is the best integration of TES with CAES to create efficient A-CAES. Thus far, efficiencies of 63-74% have been achieved [61] although the system can only operate at low pressures in the range of 1- 8 bar, the technology in this form is far from commercialisation [62].
- Construction has begun on a large-scale adiabatic CAES facility in Jintan, China. A collaboration between Tsinghua University and Zhongyan Jintan Company, the project hopes to achieve a 50 MW to 60MW A-CAES plant, requiring no external fuel input. The project aims to reduce solar curtailment in Jiangsu province. The facility will employ an existing salt cavern remaining for previous solution mining operations [63,64].
- A final example of an A-CAES demonstration is by the Chinese Academy of Sciences in Bijie City, Guizhou province. A 10MW system has been constructed by incorporating a network of above-ground storage tanks, chargeable to 70 bar, and a 22MWh sensible heat store such that the whole system can store up to 40MWh of electricity. At the time of writing, the system is still subject to further development [65].

Collating the recent major CAES developments, it is evident that there are challenges in getting the technology to market as a commercial operation. A number of well-planned and advanced projects have been stalled and ultimately failed such as the ADELE and Norton projects. Failures are predominantly attributable to economic factors. The more promising A-CAES technologies that are expected to become operational in the coming years are still far from the scale of conventional gas-fired CAES plants.

Table 2-2. Major recent CAES projects

Project Name	Location	CAES Technology	Project Purpose	Project Status	Years Active	Power [MW]	Capacity [MWh]	Efficiency [%]	Air Storage Pressure [bar]	Storage Method	Reference
Norton CAES plant	Norton, Ohio, USA	Conventional diabatic, gas fuelled	Commercial	Not realised	2001 - 2013	800-2700	-	-	55 – 110	Aquifer storage/repurposed limestone mine	[48,49,66]
GAELECTRIC Northern Ireland	Islandmagee, Co Antrim, UK	Conventional diabatic, gas fuelled	Commercial	Not realised	2008 – 2019	200 (charge) 330 (discharge)	1980	-	-	Solution mined salt cavern	[10,67]
Seneca CAES Project	Reading, New York, USA	Conventional diabatic, gas fuelled	Demonstration	Not realised	2010 - 2012	130 - 210	2000	-	-	Solution mined salt cavern	[50,51]
SustainX Smart Grid Programme	Seabrook, New Hampshire, USA	Isothermal, innovative water-foam mixture employed to ensure constant heat transfer during compression and expansion	Demonstration	Discontinued	2013 – 2015	2.2 (charge) 1.65 (discharge)	1	54	12 – 207	Above ground pressure vessels	[58]
ADELE project	Staßfurt, Germany	Adiabatic, sensible heat store	Commercial	Discontinued	2010 – 2016	200	1000	70	100	Solution mined salt caverns	[10,52,68]
PG&E Advanced Underground CAES	San Joaquin County, California, USA	Conventional diabatic, gas fuelled	Commercial	Commissioned	2010-2018	300	-	-	-	Depleted natural gas store	[10,54,55]
TICC-500	Tsinghua University, China	Adiabatic, sensible heat store	Demonstration	Active	2014 – present	0.5	0.5	33	30 – 110	Overground storage tank	[10,69]

Chinese Academy of Sciences, CAES demonstration plant	Bijie City, Guizhou, China	Adiabatic, sensible heat store	Demonstration	Active	2017 – present	2.8 (charge) 10 (discharge)	40	62.3	70	Overground storage tanks	[65]
Pilot scale demonstration of AA-CAES	Gotthard base tunnel, Biasca, Switzerland	Adiabatic, sensible heat/combined sensible-latent heat store	Demonstration	Active	2017 – present	0.7	-	63-74	8	Previously excavated unlined rock cavern	[60,61]
Zhongyan Jintan CAES	Jintan, Jiangsu, China	Adiabatic, sensible heat store	Commercial	Commissioned	2017 – present	50 - 60	200 - 300	-	-	Solution mined salt cavern	[63,64]
Goderich A-CAES facility	Goderich, Ontario, Canada	Adiabatic, cavern flooded and hydrostatic pressure used for isobaric storage	Commercial	Active	2019 – present	2.2 (charge) 1.75 (discharge)	7	>60	-	Specifically mined cavern	[56]
Apex CAES Bethel Energy Centre	Tennessee Colony, Texas, USA	Conventional diabatic, gas fuelled	Commercial	Commissioned	2019 – present	324 - 487	16000	-	-	Solution mined salt cavern	[10,53]
Feicheng A-CAES	Feicheng, Shandong, China	Adiabatic, sensible heat store	Commercial	Active	2019 – present	1250 (expected)	7500	67	-	Repurposed salt and coal mine caverns	[70,71]

2.3. Compressed Air Energy Storage Utilising Underground Formations

Underground formations have long been utilised for the storage of natural gas because very large volumes and therefore storage capacities can be reached. The underground structures employed for gas storage can be adapted for several energy-carrying fluids and are increasingly being considered to use for the storage of air in large-scale CAES systems. A number of underground structures and techniques can be employed for storage, with main considerations highlighted in this section.

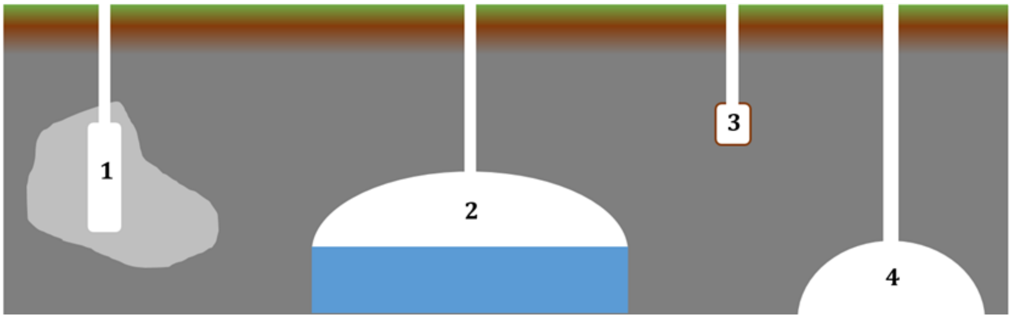

Figure 2-10. Types of formations for underground energy storage

Table 2-3. Underground storage methods: key for Figure 2-10

	Underground storage method	Note
1	Salt cavern	Typically, solution mined from a salt deposit
2	Aquifer Storage	Air is injected into permeable rock displacing water and capped by a cap rock
3	Lined rock cavern	A specifically excavated chamber, lined with an additional material to ensure hermeticity
4	Depleted gas reservoir	Reservoir previously used for gas tapping or storage, can be in permeable to semi-permeable rock type

Both commercial CAES facilities currently in operation utilise solution mined salt caverns for the air storage. Salt deposits can be multiple of kilometres thick so provide the opportunity for engineering deep, very large volume caverns. Salt cavern walls also possess moderately high strength and are usually more uniform in properties than other rock types [72], as well as maintaining a self-repairing property, where the material can flow plastically to seal fractures preventing further crack propagation [73], therefore salt caverns can remain stable for very long geological periods. Additionally, salt cavern storage requires significantly less base gas (the residual gas that must remain in the cavern upon discharging) than other mediums, particularly porous rock geologies [74]. Salt caverns are therefore best suited to the flexible operation and regular cycling that CAES plants operate under, providing higher flexibility with respect to turnover frequency with high injection and withdrawal rates [75]. Moreover, for salt caverns, exploratory work is typically lesser and therefore lower cost owing to existing knowledge of the salt structures because of prior prospecting for hydrocarbon resources [76]. A drawback of employing salt caverns is that the solution mining process is reliant on the local availability of a large amount of water for the extraction of the rock salt [77], though the obtained salt could provide an additional significant revenue stream in addition to the storage plant operation [73], provided that there exists the ability to refine the obtained brine into rock salt at a facility nearby.

In addition to salt deposits, aquifers and porous rock formations have become a standard for storing natural gas worldwide, accounting for 13% of underground natural gas storage globally [76], where the principles can be easily configured for the storage of high-pressure air. An artificial gas field is formed by injecting high pressure gas into the permeable rock displacing the water and creating a variable volume gas store. A number of additional geological criteria must be met, with a suitable cap rock and surrounding rock to form a closure. Specific aquifer characteristics are also less widely known than salt formations and all of the factors result in aquifer storage being currently the most expensive form of natural gas storage available to the industry [74] and would therefore be an expensive method of underground storage in large CAES systems. Additionally, the injection of air into porous formations may change the existing cap rock properties and may impact the operation and security of the whole system without thorough prior consideration [78]. Moreover, aquifer stores require significantly more base gas remaining after discharging further limiting the utility of this form of storage, typically between 50% to 80% cushion gas in contrast to salt caverns requiring 20% [79]. Li et al have proposed attempting to identify locations with aquifers and a significant geothermal resource. It is suggested that this could improve the efficiency of the full system by maintaining or increasing the air temperature within the cavern, as it receives heat from the surroundings [80]. A novel well bore is suggested as the method of extracting the geothermal energy and preliminary modelling has been conducted. Determining suitable locations with this additional constraint would add complexity to the planning process however. In addition, modelling of the operation cycle of an aquifer based CAES plant has been conducted, indicating the feasibility of operating such a facility on a daily, weekly or monthly cycle.

A relatively new development to the underground energy storage industry is the consideration of hard rock geology lined caverns (Lined Rock Caverns – LRC). In principle, caverns can be excavated to large volumes and lined with concrete and steel to ensure no permeability. A single natural gas storage plant has demonstrated the feasibility of this type of storage in Grängesberg, Sweden with pressures or 500 bar achieved [81]. The achievable pressures could significantly exceed those of salt cavern storage, with current CAES facilities operate in the 45 - 80 bar range [82]. Similar storage capacities could therefore be achieved even with the smaller chamber volumes. A small-scale test compressed air LRC facility has demonstrated 87 bar for the investigation of wall performance and deformation [83].The greatest potential for LRC for CAES is therefore for locations where other geographic features are not present. Capital costs of forming caverns in hard rock geologies are currently significantly greater than in salt geologies, potentially being 15 times greater [84], though specific costs will vary for each proposed location and depend heavily on the local lithological features. Zhou et al. have developed a modelling methodology for determining the degradation and damage to the cavern wall of a LRC over numerous air injection cycles [85].

Aside from utilising naturally occurring geological features, there is also great potential for the repurposing of existing underground infrastructure left as a remnant of resource extraction or natural gas stores for the storage of compressed air. At present, the most prominent method of gas storage is using depleted oil or gas reservoirs, accounting for 81% of total underground natural gas storage [76]. As these reservoirs previously contained oil or gas, the characteristics of the reservoirs, in terms of porosity and permeability, already meet the requirements for high pressure air storage [74] and it is likely that the structure and geologies of the depleted reservoirs are known owing to the surveying and prospecting prior to and during the extraction of the depleted resource. This is the method of air storage to be implemented in the previously planned PG&E CAES facility in San Joaquin, California [54]. The use of natural gas reservoirs can be seen as a viable candidate for the storage of compressed air particularly in Europe as the demand for natural gas is predicted to stagnate or decrease in the coming decades [86] with a number of existing reservoirs expected to be decommissioned.

In addition to the exploitation of depleted reservoirs, oil and gas wells, the reuse of disused mines has been considered for use within CAES systems and natural gas storage [87]. Many depleted coal mines possess large pre-excavated volumes therefore have the potential to significantly reduce the initial capital investment required. Additionally, closed coal mines are typically located locally to existing thermal power plants, therefore existing infrastructure could be utilised in adapting these systems into CAES facilities. The storage of natural gas and CO_2 has been demonstrated in abandoned mines, as with depleted oil and gas reservoirs, but never with a CAES system, the previously discussed company Hydrostor have aims to reuse a decommissioned mine for a CAES facility, though this project has not yet moved past the announcement phase [88]. There are plans to adapt a network of tunnels from a previously used coal mine in northern Spain into a small-scale A-CAES pilot plant. Preliminary work has modelled the impact on the tunnels walls of cyclic loading from the injection of high pressure air and indicates that the existing infrastructure is sufficient to withstand the imposed conditions [89] .The adaptation of existing shafts in previously used coal mines do however pose the risk of the combustion of remaining coal seams with high temperatures, thus shafts would have to be adequately sealed and assessed to ensure safe operation and feasibility [76] or exploration of underground mines from differing resources.

2.4. Potential Assessment and Analysis of Underground CAES in India and the UK

India is projected to become the most populous country by the mid-2020s [90]. Coupled with the nation's rapid economic development, drive for electrification of rural communities and increasing urbanisation, the electricity demand of India will grow substantially in the coming decades [91]. Additionally, the government of India has set the ambitious target of providing 40% of its electricity generation from renewable sources by 2030 [92]. To achieve this goal, the rate at which renewable electricity generation technologies are being installed in India is growing each year. The UK situation is similar, having achieved the target of 30% renewable electricity generation by the end of 2020. Additionally, in 2019, the UK government established the goal of achieving net zero emissions by 2050 [93]. In recent decades, greenhouse gas emissions from the power generation sector in the UK has been reduced over 80% compared with its emission level in 1990s, however, emissions from transportation and heating sectors have not. To reduce emissions, the electrification of transportation and heating is inevitable, which will in turn require more power generation, and consequently must be supplied from renewable energy sources. Without grid scale, long-duration energy storage, it will be difficult to achieve the net zero emission goal. This section examines and compares the potential capacity of CAES in India and the UK, through a proposed methodology.

2.4.1 Methodology

There have been a limited number of previous attempts to assess the potential and suitability of specific locations for underground CAES storage [94–96], but these do not regard all forms of possible underground CAES technologies and have not allowed for a quantitative analysis. A methodology for assessing the geological suitability of an area for the underground CAES is adapted from a study presented by Aghahosseini & Breyer [97], with three geological criteria under consideration to determine an area's suitability. Firstly, the identification of hard or porous rock geologies: with data obtained from the Global Lithological Map (GLiM) [98], four rock classifications were mapped: Mixed sedimentary, carbonate sedimentary, acid plutonic rocks and siliciclastic sedimentary, these rock types have been demonstrated to be preferred for underground gas and air storage when combined with aquifers, natural gas reservoirs or excavated to form caverns, as discussed in the previous section. Secondly, geological and mineral maps for Indian states [99] were gathered and used to identify salt deposits, in the form of halite or potash beds, and then were additionally mapped. It was found that the Indian salt reserves are concentrated in the north-west of the country, although the general availability of salt resources was very limited when compared to other world regions. Thirdly, large aquifer systems were identified and mapped. The identified aquifer systems were composed predominantly of two subsystems, the Indus Basin aquifer and the Ganges-Brahmaputra aquifer [100]. ArcGIS was used to map and process the results. Data relating to operating and disused oil and gas reservoirs and coal mines were not obtained for this analysis and focus was given to natural geological features. The mapped results of these three criteria are presented in Figures 2-11 to 2-13.

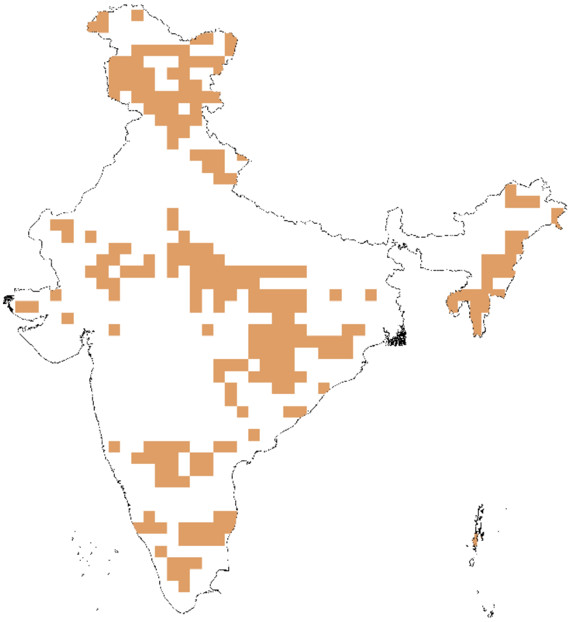

Figure 2-11. Indian locations with one of the four identified geology types[4]

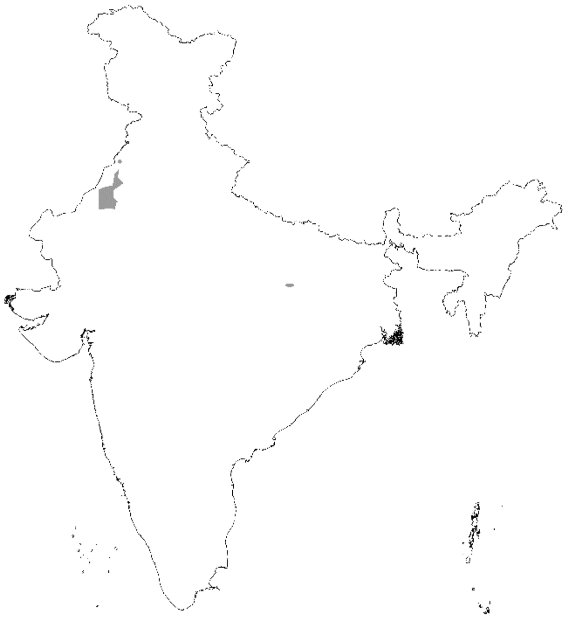

Figure 2-12. Salt deposits of India

---

[4] The suitable geology types are: Mixed sedimentary, carbonate sedimentary, acid plutonic and siliciclastic sedimentary

Figure 2-13. Large aquifer systems of India

Areas possessing at least two of these geological features were classified as being highly suitable for large-scale underground CAES. In practice, it is possible that an area possessing only one of these features would be sufficient for the formation of a large storage cavern i.e., salt deposits or some hard rock geologies, however, regions with two features present would identify the most suitable areas for CAES implementation. Therefore, the final classification generates the total suitable surface area for CAES underground storage within India. Moreover, further constraints were enforced by removing urban areas, roads, railways, national parks, other restricted land for construction, areas with elevation greater than 1500m and lakes. Furthermore, this study solely considers CAES for use in mainland India, although there are some suitable geological features present in India's island territories, their potential for the formation of CAES caverns and their integration with renewable electricity generation are not assessed here.

In addition to the determination of the overall CAES potential in India, the potential for renewable electricity generation is estimated, to assess the benefit that CAES can provide to renewable electricity generation technologies. Renewable generation can benefit from having the energy storage local to the site or entirely integrated, reducing transmission costs and losses, therefore resulting in higher round trip efficiencies. If a CAES system is directly coupled to the renewable generation, then there exists the potential for creating a dispatchable power plant or potential for consistent power output, decoupling the generation from the variable renewable resource.

Contiguous Indian land area was divided into a grid of 1° intervals of latitude and longitude and the annual capacity factor for a power plant (both wind and solar) placed at the centre of the grid cells was calculated, this is given in Equation (2.1). Data for the calculation of the Solar Annual Capacity Factor (ACF_s), was obtained from *Renewables Ninja* [101], which gives hourly solar data with the power output of the solar PV plant determined considering a monocrystalline solar PV module of 385 W possessing a temperature coefficient of power of -0.39% per degree Celsius [102]. The data used for the computation of the Wind Annual Capacity Factor (ACF_w) was obtained from *Soda Pro* [103] and modelled for a Suzlon S111 2.1MW wind turbine at a hub height of 90m [104]. This turbine was employed in the assessment as it is a large-scale Indian manufacturer and supplier of wind turbines.

$$ACF_{s,w} = \frac{E_{s,w}}{365 \times 24 \times P_{s,w}} \tag{2.1}$$

Where $E_{s,w}$ is the annual energy generated by the assumed solar or wind plant for the centre of the grid cells and $P_{s,w}$ is the rated power of the solar or wind generation. This capacity factor is then used as a method of ranking the potential for both forms of renewable generation within India.

The available area suitable for underground CAES was additionally compartmentalised into the same 1° by 1° grid cells. The cell areas suitable for CAES were then min-max normalised to rank the locations in terms for CAES suitability availability, as were the capacity factors for solar and wind generation. The three normalised factors are then multiplied together to provide a CAES-solar integration potential score ($CAES_{SIS}$), CAES-wind integration potential score ($CAES_{WIS}$) and overall CAES-renewable integration potential score ($CAES_{RIS}$) as in Equations (2.2), (2.3) and (2.4). These scores are between 0 and 1 and can be used for a direct comparison.

$$CAES_{SIS} = AF_{CAES} \times ACF_s \tag{2.2}$$

$$CAES_{WIS} = AF_{CAES} \times ACF_w \tag{2.3}$$

$$CAES_{RIS} = AF_{CAES} \times ACF_s \times ACF_w \tag{2.4}$$

2.4.2 Feasible CAES Storage Capacity in India

Applying the methodology presented in Section 2.4.1, the regions suitable for underground CAES in India are identified and presented in Figure 2-14. Total land area with the geological potential for underground CAES is determined to be 34,400 km^2, with the greatest density of CAES suitability across central-northern states of Madhya Pradesh and Uttar Pradesh. A small area of CAES suitable land is identified in the west of Gujarat and additional clusters of land in Jammu & Kashmir and Punjab. There is some suitability for CAES in the east of the country in West Bengal and Assam.

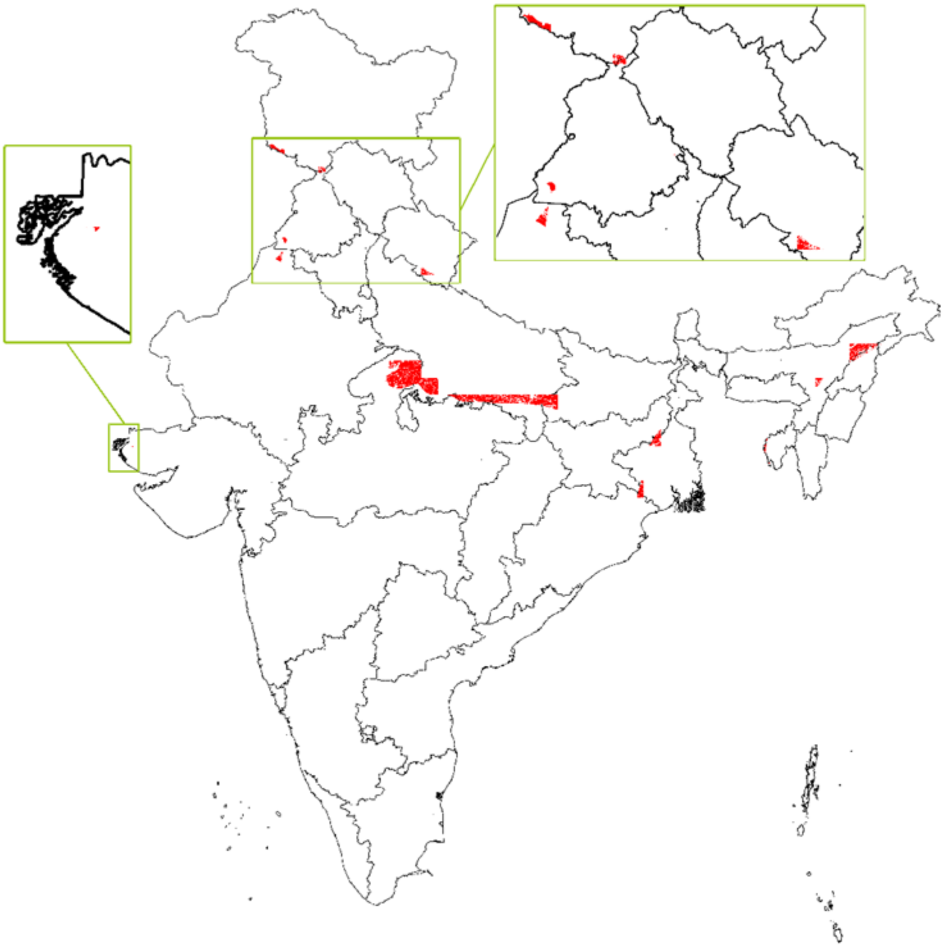

Figure 2-14. Identified areas suitable for CAES in India

The total land area of India is approximately 3.29 × 10^6 km^2, therefore this analysis concludes that 1.05% of land would be deemed suitable for the installation of a large-scale CAES facility. Taking assumptions that all of the determined CAES suitable land could accommodate CAES plants with similar energy density characteristics to the Huntorf and McIntosh plants and a constant energy storage density (regardless of the implementable storage type at a particular location), an estimate for the total capacity of CAES in India can be determined. The number of possible caverns is calculated from determining the amount of Huntorf caverns that would fit in the total above ground surface area deemed suitable for CAES. Note the Huntorf storage facility is comprised of two storage caverns, but parameters are only taken for one of these for this analysis. With the number of possible caverns determined an estimate of an upper limit of the cavern volumes can be given. The estimate for the potential CAES energy storage capacity is given in Table 2-4 with the full compartmentalised results contained in Appendix B, Table B-1.

Table 2-4. Total CAES capacity in India

Constant	Value		
Total suitable area for CAES	34,400	km^2	
Huntorf cavern surface area occupied	0.00125	km^2	[97]
Number of possible caverns	2.75×10^7		
Volume of Huntorf cavern	141,000	m^3	[105]
Total available volume for CAES caverns	3.88×10^{12}	m^3	
CAES energy storage density	0.003	$MWh \cdot m^{-3}$	[47]
Total potential for CAES in India	11.6×10^9	MWh	

Total electricity demand in India is estimated at 10^9 MWh annually [106], therefore the total underground CAES energy storage capacity potential stands at approximately 10 times greater than annual demand if all available land were utilised for this underground storage of air. Thus, although it can be concluded that there is sufficient geological resource to meet India's energy storage requirements, it is highly unlikely that CAES alone will be a sufficient technology in its current form. Utilisation of all potential land is likely to be very small (much less than 1% of available) thus a variety of differing energy storage systems should be examined for the Indian situation. India's suitable land area for CAES also ranks very low when compared to other nations [97] predominantly owing to the lack of availability of salt deposits. As such it is very unlikely that sufficient CAES plants can be constructed at an economically viable price to totally meet India's energy storage requirements, unless there are substantial advancements and demonstrated CAES facilities utilising storage mediums other than salt caverns.

Figure 2-15 displays the distributions of the potential for solar and wind generation across India. When considering electricity generation from solar, there is greatest potential in the north-west of the country across the states of Rajasthan and Punjab. For wind generation, the highest potentials are in the western states of Gujarat and Rajasthan and across the south-central states of Karnataka and Maharashtra. In general, there is not good coincidence between areas of both high solar and wind potential, though Gujrat and some areas of Rajasthan do show promise of high levels of generation from both renewable resources.

Of the 357 grid cells that India has been divided into, 31 contain suitable geographic criteria for underground CAES development. These are ranked in Table B-1 (Appendix B) along with the normalised factors for wind and solar generation. From the analysis, the states of Madhya Pradesh and Uttar Pradesh are identified as the locations where renewable generation could most benefit from integration with CAES owing to the good renewable potential and wide availability of CAES suitable land. Further detailed investigation should be conducted with a focus on these two states to determining the viability of underground CAES systems in these regions.

The state of Gujarat possesses very good solar and wind power generation potential but possesses minimal geological potential for the construction of underground CAES, therefore in this area particularly renewables should be developed and integrated with more appropriate energy storage technologies.

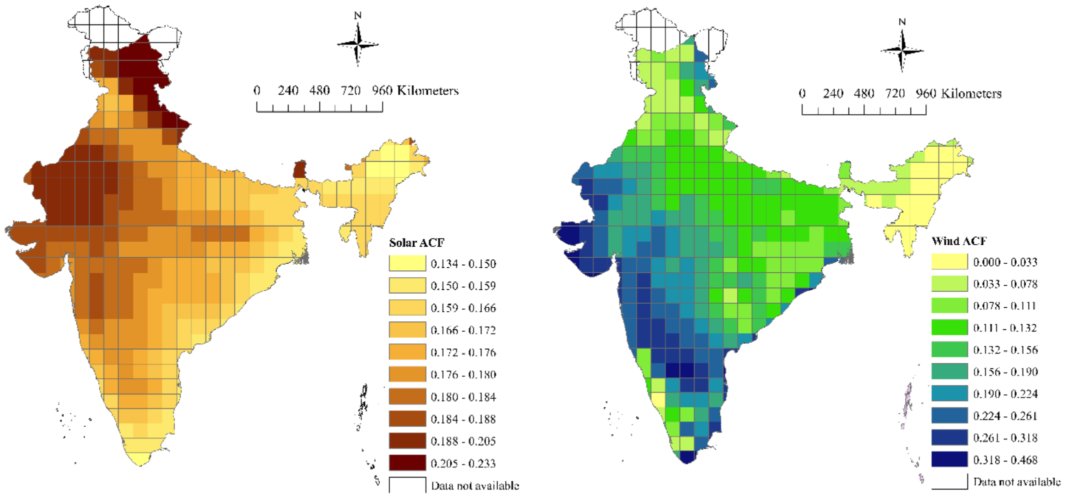

(a) **(b)**

Figure 2-15. (a) Solar capacity factor distribution for India (b) Wind capacity factor distribution for India [107]

2.4.3 Feasible CAES Storage Capacity in the UK

The availability of CAES suitable features in the UK is substantially different to that of India. The UK is a much smaller country by area and population and possesses a wide abundance of salt deposits; these can be observed in Figure 2-16. The Cheshire Basin in north-west England contains numerous large salt beds. Historically, caverns have been formed from these beds and used for the storage of natural gas, and because of the wide availability and previous usage, much attention has been directed at adapting this geological resource for CAES. If all of the existing salt caverns present in the Cheshire Basin were converted to the storage of air then 725 GWh of capacity would be achieved, 26 times greater than the UK's current pumped hydro capacity [108]. Taking all the salt beds present in the Cheshire Basin as a whole, it has been estimated that it is abundant enough to form up to 100 caverns, providing capacity for 2.53 TWh of storage with an output power of up to 40 TW [109], this would greatly exceed daily average demand of the UK grid. It will almost certainly be cheaper to repurpose the existing gas facilities to CAES storage as the UK decarbonises than it will to construct new salt caverns. In addition to the use of salt caverns for CAES, there exists great potential for the UK's saline aquifer resources to be employed. There is sufficient capacity for 96 TWh using the saline aquifers [110], although these will prove more difficult to harness and their use relies upon less established technologies than salt deposit storage. In the near future, it is recommended that the salt deposits should therefore be targeted for the development of CAES in the UK, prioritising existing infrastructure from previous gas stores.

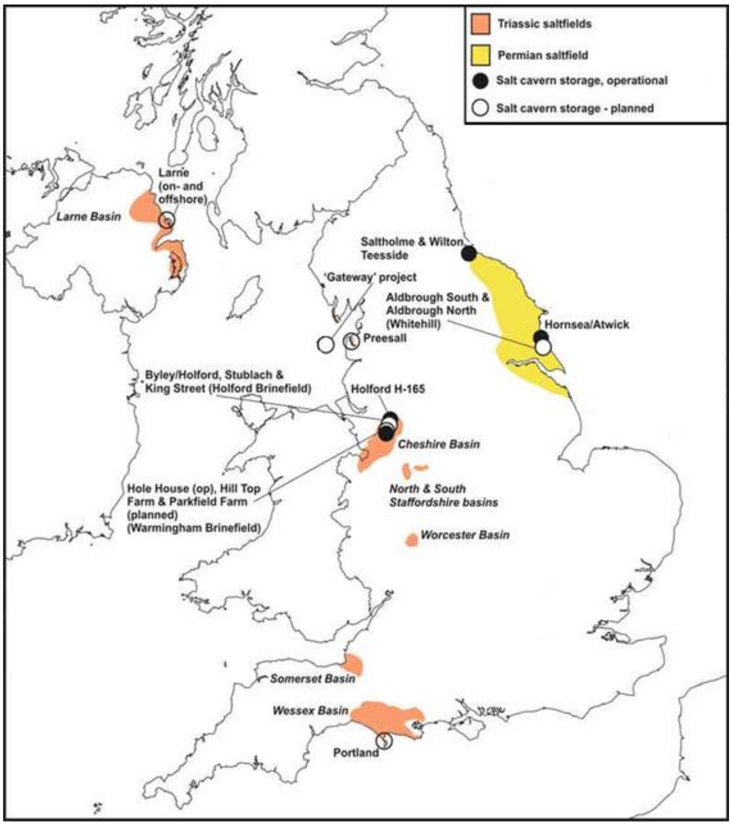

Figure 2-16. UK salt deposits. Operational and planned natural gas storage sites that have the potential to be converted to CAES storage [111][5]

2.5. Summary

One of the most promising solutions for mitigating the challenges of the variability and uncertainty in renewable generation is EES. There are several competing EES technologies, each possessing unique mechanisms and characteristics. CAES is one of the most mature EES technologies that excels, when compared to competing EES, in terms of range of system size, system lifetime and storage duration. The reliance of CAES on underground formations for storage is a major limitation to the rate of adoption of the technology. Several candidate methods for using underground formations for CAES have been discussed, however presently salt caverns show the most promise as these have been demonstrated for use in gas and CAES storage and are abundant in many locations. A CAES capacity determination methodology is proposed, and an assessment of the potential for underground compressed air energy storage has been conducted for India by collating geological characteristics local to each region and integrating the potential for renewable electricity generation. India has great potential for solar generation, particularly in the northwest of the country and a lesser potential for wind

---

[5] Adapted from reference figure.

generation. The total land area suitable for underground air storage has been evaluated to be 34,400 km^2 or approximately 1.05% of total land area. It is suggested that this resource is sufficient to meet India's electricity storage requirements solely with CAES though this scenario is highly unlikely as only a very minor fraction of this land could practicably be used. The UK situation for CAES potential is greatly different with large salt deposits with sufficient capacity to meet energy demand if fully utilised. The assessment methodology proposed in Section 2.4 can be adapted and applied to other nations for the determination of CAES and renewable integration feasibility and has the potential to inform the strategy of CAES technology expansion.

Chapter 3 – Compressed Air Energy Storage Integration to Benefit Photovoltaic Generation

Following from the introduction of CAES as an EES and examination of its potential to benefit wind and solar photovoltaic (PV) power generation through conventional integration, this chapter introduces the prospects of additional benefits from the integration of CAES with PV generation that can be achieved by integrating CAES with PV for panel cleaning and cooling, ameliorating soiling and heating losses and therefore increasing generation efficiency.

In this chapter, PV electrical power generation is examined, and key features of the technology are described. The negative impacts upon PV generation from panel soiling and high panel temperatures are identified and current mitigation strategies targeting these two sources of inefficiencies are discussed. A system for integrating CAES with PV generation to achieve panel cleaning and cooling is proposed.

3.1 Overview of Solar Photovoltaic Technologies

Solar photovoltaic (PV) panels generate electrical power via the photoelectric effect. Photons transfer energy to electrons in the modules' semiconductor, allowing the electrons to break free leaving a positively charged atom and a free negatively charged electron [112]. Conductive grids at the top and bottom of the cell collect these charges and when connected into a circuit current is allowed to flow.

The large-scale development and implementation of solar PV as an electrical power generation technology began to grow steadily from the 1970s onwards [113], driven primarily by the oil crises and subsequent desire to find alternative generation sources, independent of fossil fuel requirements. As the technology matured and achievable efficiencies increased in the subsequent decades, the adoption of solar PV began to grow rapidly during the late 2000s, this is demonstrated in Figure 3-1. To meet the goals of the United Nations Paris Agreement of limiting mean global temperature rise to less than 1.5°C [5] signed in 2015, fossil fuel generation is being phased out in most developed countries. Therefore, the rate of installation of PV continues to increase, as PV have been identified as one of the key low-carbon generation methods to replace greenhouse gas emitting generation. During the year of 2020, solar PV accounted for 3.1% of global electricity generation [114], with 135 GW of PV installed during the same period, accounting for 39% of all additions to generation capacity [6].

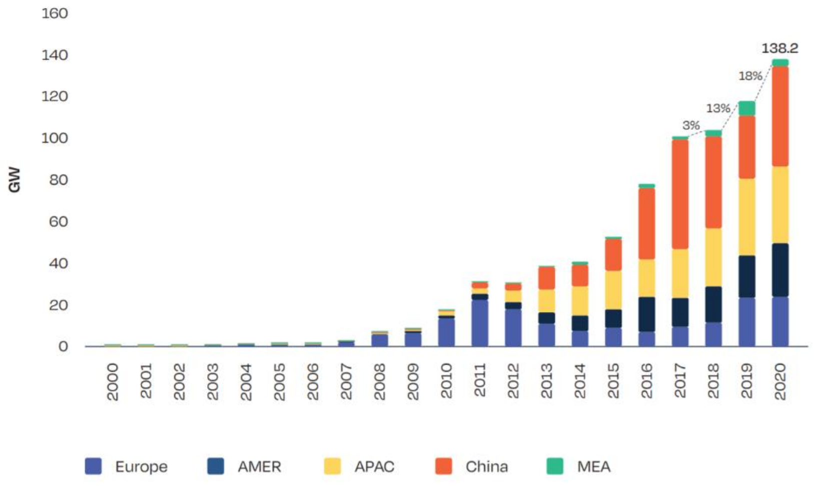

Figure 3-1. Installed capacity of solar PV by region, 2000 – 2020 [6]

The proportion of worldwide generation from PV is expected to substantially grow over the next decades [115], with worldwide solar PV generation expected to surpass total coal generation by 2050 [116].

The primary advantage of solar PV as an electrical power generation technology is the abundance of the solar resource. Solar radiation received by the Earth's surface is approximately 85,000 TW, at least two orders of magnitude greater than current global electricity demand [117]. In addition to the availability of solar energy, PV generation possesses many advantages compared to conventional fossil fuel generation. Panels are simple to install, once installed produce no emissions, are implementable across a wide range of scales and are beginning to outcompete thermal power generation in cost terms because of a reduction in production cost and the rising price of oil, gas and coal.

3.1.1 Features of PV Technologies

Although there are many methods for harnessing energy from the solar resource, the solar energy sector is dominated by electrical power generation and within the solar-electric sector, photovoltaics are the dominant technology. For example, in 2020, 821 TWh energy was generated from PV compared to 14.5 TWh from concentrating solar power (CSP) generation [114,118]. Within PV generation, there are multiple sub-technologies with commercial installations dominated by two types: monocrystalline and polycrystalline cells [119]. Monocrystalline cells are formed from a single crystal that possesses a continuous lattice structure with very few impurities. Polycrystalline cells are comprised of multiple smaller elements of monocrystalline silicon that are compiled into a single cell. Monocrystalline cells are more efficient at converting irradiance into electrical current, with typical efficiencies of 14-15% and efficiencies in excess of 20% achievable [120], but are more expensive because of the complexity in growing single large crystals during the manufacturing process. Conversely, polycrystalline cells are less efficient, typically ranging from 12-14% [119] but are cheaper to manufacture, as crystals can be grown to a range of sizes, cut and bundled into complete cells. Of the two technologies, polycrystalline cells have been more widely implemented because of their lower cost, but with the reducing cost of manufacture and innovations in Silicon casting, the market share of monocrystalline cells is expected to increase in the coming years [121].

3.1.2 PV Characteristics

Figure 3-2 indicates a typical current-voltage (I-V) characteristic curve for a PV panel at a constant temperature and constant level of irradiance. When the panel is short-circuited, i.e., resistive load is negligible but current is allowed to flow, the current reaches a maximum, I_{sc}. When the panel is not connected, i.e., open circuit, so no current can flow, the module voltage is at a maximum, V_{oc}. The power delivered by a module to a connected resistive load is the product of the voltage and current, so in both instances, no power is delivered by the module. This can be observed through the power-voltage (P-V) characteristic curve, in Figure 3-3.

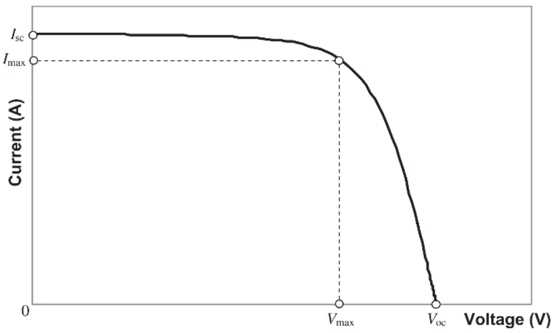

Figure 3-2. Typical current-voltage (I-V) characteristic curve for a PV module [120]

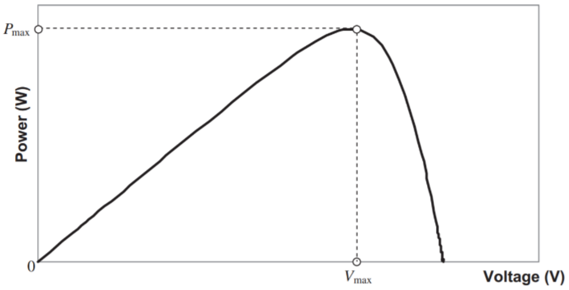

Figure 3-3. Typical power-voltage (P-V) characteristic curve for a PV module [120]

The maximum deliverable power is achieved when operating at the maximum power point (MPP), defined as the point on the I-V curve where the product of the current and voltage are at a maximum. These currents and voltages are denoted as I_{max} and V_{max} respetively. Owing to the desire to operate at the MPP, maximum power point tracking (MPPT) algorithms are implemented to control the operating voltage and current and ensure that the MPP is reached. At the point of generation, the DC power generated by PV modules usually undergoes power conversion or inversion for integration with the load or grid and MPPT algorithms are implemented at this stage.

The shape of the characteristic curves of PV modules are predetermined by factors such as cell material, size and connection of the individual cells in the panel but are additionally dependent on the instantaneous irradiance level and operating temperature of the module. Figure 3-4 demonstrates the effect of temperature and insolation on the characteristic curves of a typical PV panel.

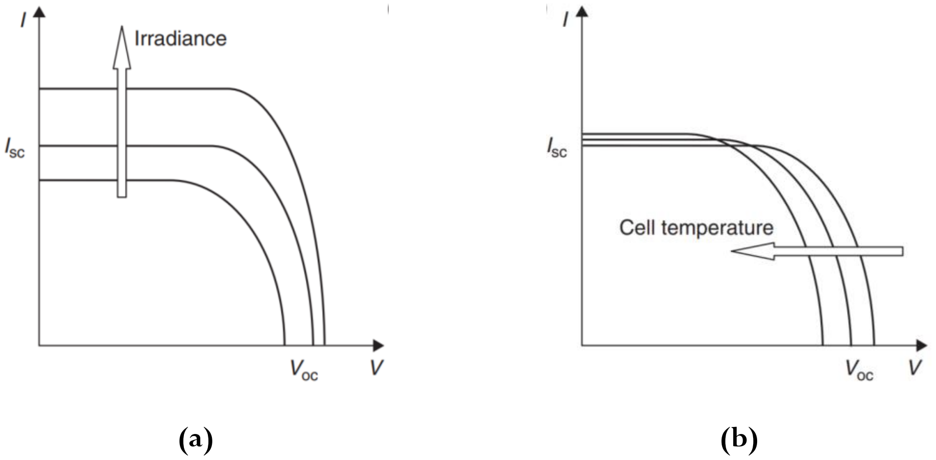

(a) **(b)**

Figure 3-4. (a) Effect of irradiance on typical I-V curve (b) Effect of cell temperature on typical I-V curve [120]

Figure 3-4(a) demonstrates the effect of irradiance on the I-V curve of a typical PV panel. The short circuit current increases linearly with an increase in irradiance and the open circuit voltage increases logarithmically. Therefore, for a panel at a fixed temperature, increasing the level of irradiance that the panel is subjected to, the power output increases. Observing Figure 3-4(b), an increasing temperature decreases the open circuit voltage linearly and increases the short circuit current linearly. With temperature increase, the relative decrease in open circuit voltage is far greater than the increase in short circuit current, therefore the overall effect is a decrease in output power with an increasing temperature at a fixed level of irradiance.

3.1.3 Properties of PV Power

As with all renewable electricity generation methods, there are challenges to the adoption of PV technologies. Owing to the variable nature of the primary solar energy source, generation from PV is inherently intermittent. Although the overall quantity of solar energy reaching Earth is in abundant, there are large fluctuations in the instantaneous availability over each day and across seasons. During night, PV cells can produce no power and in winter seasons the overall availability of irradiance is diminished, so PV generation is significantly reduced. An electrical grid with a high proportion of variable renewable generation, such as PV, faces greater challenges in balancing supply and demand to maintain grid frequency and grid stability. The intermittency and stochastic nature of PV generation is not shared by traditional thermal plants that are dispatchable with operators able to ramp up or down generation to meet current grid demand.

Additionally, PV technologies possess relatively low energy densities and efficiencies when compared to other generation technologies. This means a larger area is required to generate the same power as a conventional thermal power plant.

3.1.3.1 Curtailment of PV Generation

Owing to the variability of renewable generation and power demand, renewable electricity generation is subject to curtailment. This occurs when immediate potential for generation from renewable resources exceeds the current local power requirement, so power is not delivered from these resources and potential generation is lost. Although the curtailment rates of solar are typically low, as PV generation is prioritised over other forms of generation because it involves no-emissions and marginal costs at the point of generation, a significant quantity of energy from PV generation is lost because of curtailment. An estimate 6.5million MWh of PV generation was wasted because of curtailment in 2018 with estimated curtailment rates for different countries ranging from 0.3-8.4% power reduction [122,123]. PV curtailment therefore reduces the profit of plant operators but at present is necessary to maintain the stability of the grid [124]. It is expected that as the proportion of PV power within the grid mix grows, rates of curtailment will grow as variability and uncertainty effects are magnified [125].

3.2 Photovoltaic Panel Soiling

Photovoltaic panel soiling is the accumulation of material on the surface of panels that leads to a reduction in power output. Particles present on the surface of PV panels block light from reaching the current producing photodiodes within the individual solar cells that comprise the panel, with the light either absorbed or reflected by the particles [126]. Figure 3-5 provides an example of soiled and un-soiled PV panels. Though predominantly arising from dust and sand, the term soiling does not exclusively refer to these particles, but also encompasses bird droppings and other sources of surface contamination [127]. The primary constituent components of particles contributing to soiling losses have been shown to be mineral dust, pollen, engine exhaust particulates, bird droppings, agricultural emissions and biological-particles (algae or fungal spores etc.) [128] and exist within the range of 2-63µm diameter [126] with an average diameter of between 15-30 µm [129]. The adhesion of finer particles to panels' surfaces has been shown to contribute to a greater reduction in power output than the same density of larger dust particles [130], because they can fit into grooves present owing to the surface roughness of the panels and are more efficient at filling voids present between other particles. Additionally, dust colour has been shown to effect soiling impact also [131], with dust of a darker shade reducing power out of PV panels greater than dust of a lighter shade.

Figure 3-5. Example of soiled[6] panels (left) and unsoiled panels (right) in a large PV power plant [132]

PV panel soiling is estimated to account for a minimum of 3-4% reduction in global PV power production annually resulting in approximately £4 billion loss in revenue [128]. Without cleaning, and dependent on location, loss in potential power generation arising from dust accumulation can exceed 1% per day [126] and 1-9.3% reduction in power output per month [133]. Cumulative loss factors of 15-43% across longer term assessments have been reported [134–137]. Estimates for the effect of dust potency on power output generally lie within the range of 2-8% $g^{-1}m^{2}$ [138].

Specific soiling losses of an individual installation can be measured, but precisely quantifying and predicting the impact of soiling on global PV power generation is challenging [139]; numerous factors influence the rate of dust accumulation and the effect on power generation that this introduces. The factors influencing soiling rates and effects can be divided into geographic, pertaining to location influenced factors, and installation factors, regarding choice of technology and design. Geographic factors comprise local temperature, dust type, wind-speed, wind-direction, rainfall and humidity, with installation factors comprising panel tilt-angle, orientation, height, panel surface material [140]. Furthermore, soiling is not uniform throughout the year but varies from month to month, season to season with changes to local weather conditions [141]. Because of this, it is generally easier to forecast soiling losses over a longer period than over short durations, as instantaneous variability in the environmental conditions and their impacts can be difficult to predict [142].

Furthermore, depending on the connection of the individual solar cells that comprise the PV module, non-uniform soiling can lead to a significant observed power reduction, because of a

---

[6] The panels are non-uniformly soiled with a greater concentration of sand accumulated at the top of the panels.

large current mismatch and local heating effects arising from the partial shading [143]. Therefore, losses in PV power generation can be greater for a panel that is soiled non-uniformly than a panel that has equal dust distribution across the panel surface [144]. The effect of non-uniform soiling has also been shown to contribute to an overall degradation in the lifetime of the panel [145,146]. Non-uniform soiling can create local '*hotspots*' of elevated temperature in the PV panels, that through repeated thermal cycling from intense sun exposure has been shown to decrease performance and lead to breakages at an accelerated rate through thermal degradation and expansion.

3.2.1 Mitigating the Effects of PV Soiling

To reduce the negative effects arising from the deposition of particles on PV modules, researchers and plant operators widely practice and investigate methods of soiling mitigation. Primarily, techniques can be categorised into active and passive. Methods are defined as active if regular intervention is undertaken to remove accumulated dust on the panels. Passive methods aim to minimise the amount of action required after the installation of the PV system. In addition to these derived methodologies, soiling effects can be ameliorated by natural phenomena (precipitation etc.), which can reduce the rate of dust accumulation on the panel surface as well as remove adhered particles. Figure 3-6 categorises the methods for limiting effects of panel soiling.

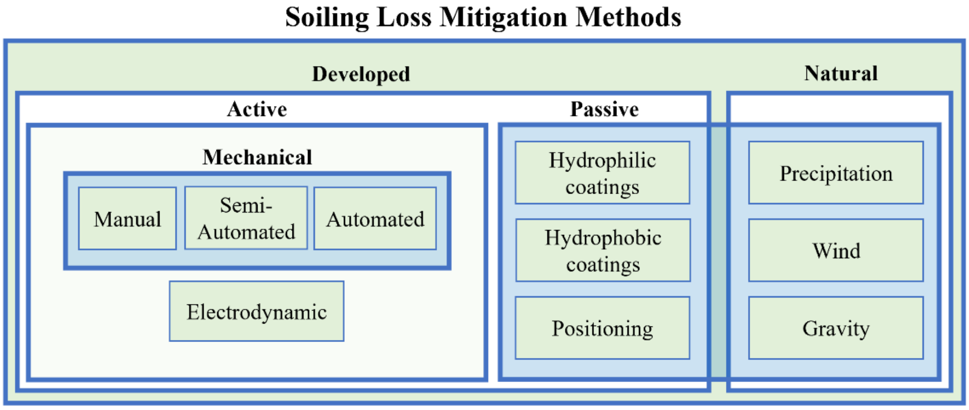

Figure 3-6. Categorisation of soiling mitigation methods

3.2.1.1 Manual Cleaning

Manual cleaning is the most widely practised method for removing dust from the surface of PV panels [140], where human labour is used to mechanically wipe dust from the panel surface. Typically, hard-bristle brushes or soft cloths are used as the cleaning device, with water employed to aid particle detachment. Sometimes additional chemical cleaning solutions are used [147]. Manual cleaning is heavily dependent on the local cost of labour but is generally the most economical technique for cleaning small to medium sized plants. As a method of removing adhered dust, manual cleaning is highly effective and if performed thoroughly, all present dust can be removed. However, repeated brushing of PV panels can damage the surface leading to a reduction in optical transmissivity and a decrease in performance as well as reduce the panel lifetime [148]. Additionally, the necessity of water to effectively clean the panels limits the technique's application to non-arid regions. When employing manual cleaning of PV panels, the foremost consideration is the frequency and scheduling of cleaning, to create the optimum balance between additional revenue from clean panels compared to the required cost of cleaning [149–151].

3.2.1.2 Automated Cleaning

Automated or semi-automated methods function similarly to manual cleaning with both being regarded as mechanical methods in which contact is made to the panel surface with some cleaning implement, however for automated methods, machinery replaces human labour. Brushes or cloths contact the panel surfaces and remove present dust. This may be done with a rotary brush system that tracks across a rail or may involve a fixed wiper that brushes dust away, as in the mechanisms proposed by Deb et al. [152] and Khan et al. [153], in Figure 3-7(a) and 3-7(b) respectively. Furthermore, vehicles can be used as the prime mover for the cleaning brushes, as depicted in Figure 3-7(c) [154] and small-scale robots capable of moving between panels cleaning each individually have reported some use as in Figure 3-7(d) [155].

The initial capital investment of cleaning machinery is greater than that of manual cleaning and there are still associated labour costs, particularly with semi-automated methods, where a trained operator needs to be present to begin or oversee the cleaning process. As with manual cleaning, abrasion to the panel surfaces and degradation of the panels can occur and in some cases, water is still a requirement. Semi-automatic methods are far more prevalent than fully automatic methods, with the latter only accounting for 0.13% of the global PV cleaning market [128]. Though not used commercially, investigations into the use of ultrasonics have been shown to be a viable method of dust removal from the surface of PV panels that has potential for easy automation [156].

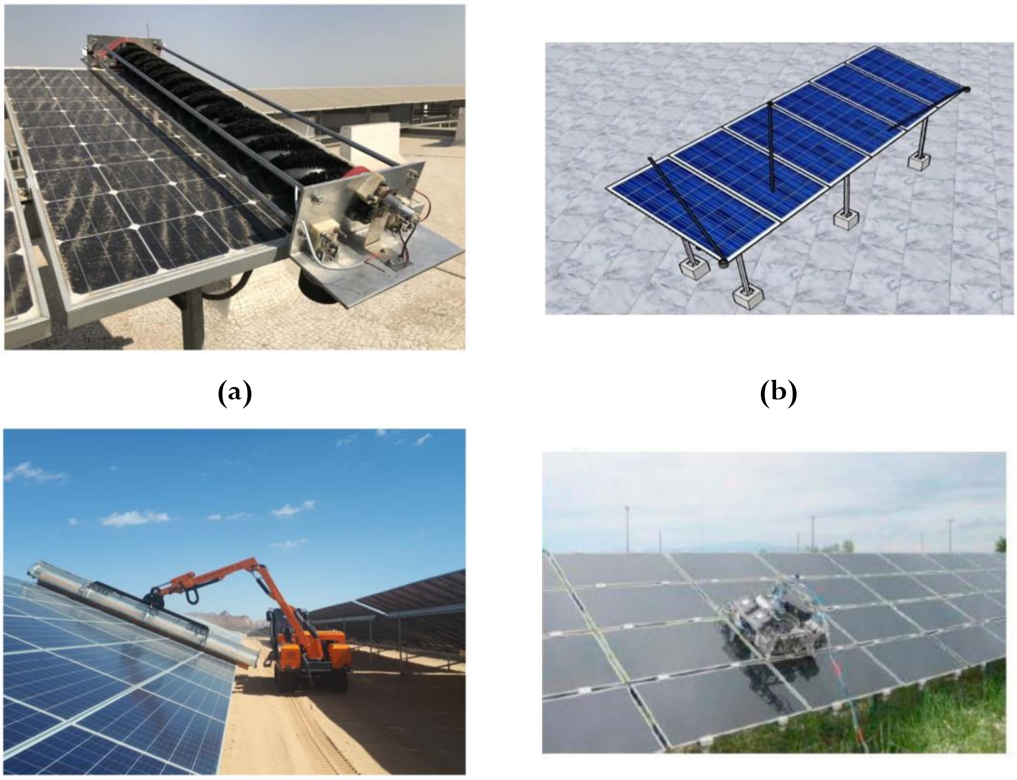

(a) (b) (c) (d)

Figure 3-7. Automated and semi-automated cleaning methods for PV modules

3.2.1.3 Electrodynamic Dust Shields

Electrodynamic dust shields (EDS) are a developing concept for the removal of dust by utilising dynamic electric fields [147]. A thin film with attached or printed electrodes is placed on top of the PV panel. The electrodes have alternating high voltages applied to them creating an electrodynamic wave; dust is repelled owing to the electrostatic charges of the particles [157]. Electrodes should be transparent or thin to limit shading losses [158] and the produced electrodynamic wave can be a standing wave or travelling wave. For systems designed for a standing wave implementation, particles are repelled and carried away by the wind and in the travelling wave orientation, the particles are migrated along the surface of the panel to the edges. A six-month study by Guo et al. reduced soiling losses by up to 33% using an electrodynamic dust shield when compared to a reference [159]. Most research has demonstrated their effectiveness on small solar modules, however increasing size of the EDS is expected to not impact the dust removal efficiency, indicating their potential use in large-scale solar plants. At lower levels of soiling however, the overall performance in the removal of dust by EDS are diminished [160].

3.2.1.4 Super-hydrophobic and Super-hydrophilic Films

Anti-soiling coatings, such as super-hydrophobic and super-hydrophilic films aim to create '*self-cleaning*' panels by maximising the benefit of rainfall at removing dust. Panels are coated with super-hydrophobic films that possess extremely low wettability, this means that droplets that come into contact with the surface have a large contact angle [147], this is demonstrated in Figure 3-8(a). This encourages the water droplets to roll rather than adhere or sit on the panel surface. As the droplets roll away, particles that the droplets encounter are carried to the edge of the panels. Super-hydrophilic films function an opposite manner, water in contact with the film forms a very low contact angle, demonstrated in Figure 3-8(b). With sufficient rain this creates a thin film of water across the entire surface of the panel. Settling dust therefore comes into contact with the thin film of water rather than with the panel surface and is carried away the by gravity to the edge of the panel, buoyant on this thin film. Gravity is the force driving the particles from the surface, so these coating methods' effectiveness are dependent the panel tilt angle. It is unclear if these anti-soiling coatings can be practically applicable in large commercial solar plants, with cost and durability being key issues identified [140,161]. Additionally, few studies demonstrate their effectiveness outside of a laboratory setting so further field testing needs to be pursued [162]. The applicability of these coatings in commercial solar plants are limited further by the locations of the large-scale facilities in arid environments. As they rely on rainfall as the cleaning mechanism, in installations where rain is scarce, they would be ineffective [161].

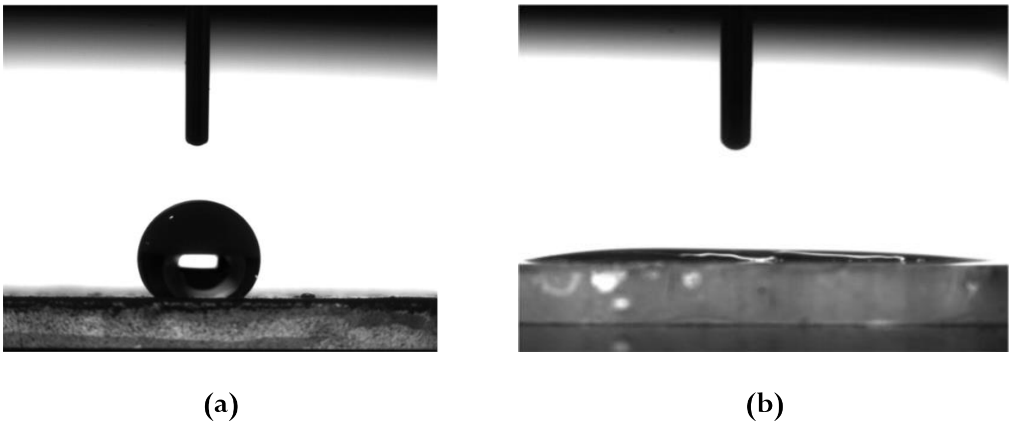

(a) **(b)**

Figure 3-8. (a) Water droplet in contact with a super-hydrophobic coating (b) Water droplet in contact with super-hydrophilic coating [163]

3.2.1.5 Passive Methods

In some cases, passive, natural methods are used to retard the rate of panel soiling, reducing potential power loss. Also, natural phenomena can be used to provide a cleaning effect to a soiled panel. These are particularly effective in regions where soiling is light so the cost of cleaning may exceed revenue gained from the excess generation of clean panels. The two dominant natural cleaning factors are precipitation and wind. Rainfall as a cleaning mechanism, possesses widely variable effectiveness and is unreliable and inconsistent. Furthermore, rainfall cannot be depended upon in arid regions where it is scarce. However, Conceição et al. have shown that in Southern Europe cleaning is not required throughout the winter months owing to the increased level in rainfall that prevents the accumulation of dust, regularly passively cleaning the installed panels throughout this duration [164]. Wind cleaning is similarly inconsistent, with a range of effectiveness. It has been shown to be effective for removing large particles, larger than 50 µm, however is ineffective at removing smaller particles, with these contributing more to soiling losses [165,166]. The orientation and angle of the panel can contribute to soiling rate, for example angling with consideration of prevailing wind direction to maximise wind cleaning. It is difficult however to do this while not compromising the best angle and orientation for solar gain. The tilt angle of the panel also plays a big role, Conceição et al. demonstrate that dust accumulates at a faster rate on a flat panel and reduces to a negligible amount on a vertical panel [167]; this relationship was also measured by Ullah et al. [168]. Therefore, if conscious of soiling effects, installers should be considerate of panel tilt angle, not only in terms of maximising solar input but also dust accumulation reduction.

3.2.1.6 Discussion of Soiling Mitigation Methods

There is no universally adopted method for mitigating soiling effects, with the main factors influencing the approach being location (determining the rate of soiling, climate, economic pressures, accessibility) and the size of the installation. It is clear there are a wide range of anti-soiling strategies in use and under investigation owing to the great economic losses that are incurred because of panel soiling. Table 3-1 summarises the soiling mitigation methods identified in this section.

Table 3-1. Summary of soiling mitigation methods for PV panels

Method	Advantages	Disadvantages
Manual cleaning	• High proportion of dust removal • Can be performed when needed • Low capital cost	• Expensive and cost dependent on local availability of labour • Water requirement • Possible surface damage
Automated cleaning	• High proportion of dust removal • Minimal labour cost • Automation allows flexible operation	• High capital cost • High operation and maintenance costs

Natural cleaning	• No cost	• Location and climate dependent • Low proportion of dust removal, particularly for smaller particles
Super-hydrophobic coatings	• Passive cleaning method, no additional action required	• Short lifespan • Expensive • Cannot be implemented in arid environments
Super-hydrophilic coatings	• Passive cleaning method, no additional action required	• Expensive • Cannot be implemented in arid environments
Electrodynamic dust shield	• Fast acting • High effectiveness in certain conditions • Can be automated • Water-free method	• High capital cost • Ineffective in high-humidity environments • Needs high voltage electricity supply • Low effectiveness at low soiling levels
Panel Positioning	• No capital investment • Reduces required frequency between cleaning	• Does not eliminate soiling losses • May not be applicable in some locations • Secondary cleaning may still be necessary

As described, manual cleaning is markedly the most employed technique; therefore, the motivation for the development of subsequent strategies has been to alleviate the need for manual cleaning which can be expensive and logistically difficult owing to the increasing scale of newer plants and the remote and potentially inaccessible regions in which an increasing number of solar plants are being installed. The lack of automation within the sector ensures the cost of cleaning is linked to the local availability of labour. Additionally, semi-automated methods do not eliminate these requirements as some human operators are necessary.

A common limitation of many of the existing methods is the reliance on water, whether this be as a resource or in terms of rainfall. This can drive costs up or limit the applicability of techniques in certain environments and render the proposed '*self-cleaning*' methods ineffective. Additionally, complexity of methods, particularly engineered mechanisms tend to lead to reduced durability and increased maintenance requirements that in turn increases costs. Furthermore, the latter presented methods of panel coatings and dust shields are still in development and currently not mature enough to be employed in the PV cleaning sector.

3.3 Photovoltaic Panel Heating

Solar modules, typically, convert less than 20% of incident solar radiation into electrical power under standard conditions [169]. The unconverted radiation is stored by the panel material as sensible heat, raising the cell temperature. When the material temperature increases, the bandgap energy of the semiconductor decreases. The electrons within the semiconductor are at a higher energy state and need less energy to escape to form an electron-hole pair. This means that at higher temperatures the intrinsic carrier concentration is greater and this results in a higher saturation current. The open circuit voltage is inversely correlated to the saturation current, so the open circuit voltage decreases with an increase in temperature. This results in a lower overall electrical conversion efficiency as the open circuit voltage is the dominant factor in overall cell power output [170].

For typical commercially operating PV systems, there is an observed 0.3% to 0.5% decrease in efficiency per degree of temperature increase [171]. This is relative to the rated efficiency of the module which is measured under standard conditions of 1000 Wm^{-2} and cell temperature of 25°C. However, in real-world operation, panels tend to operate at temperatures hotter than this and at lower levels of insolation. Cell temperatures of 50-60°C are common in tropical climates [172,173], with cell temperatures as high as 80-85°C measured in some locations [174,175]. This results a large wastage of potential generation capacity because of excessive temperatures. The efficiency losses from high cell temperatures are additionally exacerbated because locations that have a good solar resource, tend to also have high ambient temperatures, increasing average cell operating temperatures. It is therefore difficult to decouple cell temperature inefficiency from large-scale generation.

Furthermore, temperature is one of the key factors that influences the degradation of solar cells, particularly large swings in temperatures. This situation presents itself most readily in desertic environments where ambient temperature can range from as much as 40°C per day and panel temperature up to 80°C. The expansion and contraction of the panel under these temperature effects leads to a reduction in overall panel lifetime [176].

3.3.1 Mitigating the Effects of PV Heating

Although not extensively practiced in the PV industry, because of the negative effects to PV generation arising from high temperatures, there is a growing body of research investigating techniques for thermal management of PV modules. Previous, comprehensive reviews have presented heat mitigation methods for solar PV modules [177–183], with the key methods and research highlighted in this section. Figure 3-9 categorises the main approaches for managing PV panel temperatures. Primarily techniques can be broken down into active and passive methods. Active cooling approaches require additional energy input to cool the panels and passive methods operate without additional energy input.

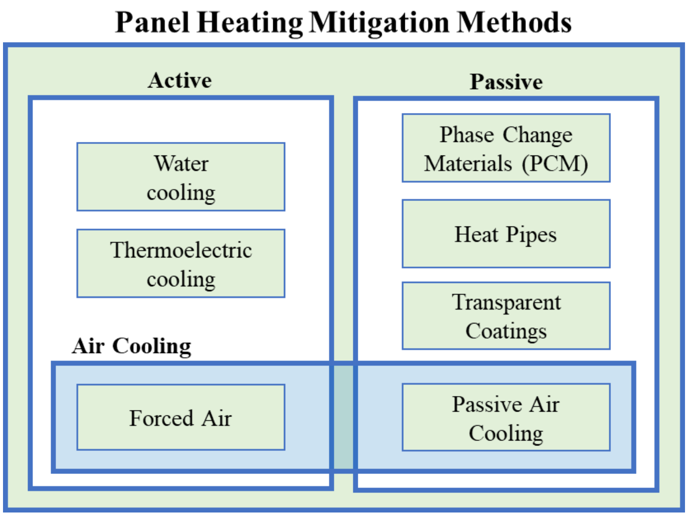

Figure 3-9. Categorisation of heating mitigation methods

3.3.1.1 Air Cooling

Air cooling is applied in many engineering systems as a thermal management technique. Air cooling can either be active or passive; active air systems consume energy, typically through the powering of a pump or fan, blowing air across the component that needs to be cooled. Heat is transferred from the system to the high velocity air stream which carries it away, lowering the temperature of the system through forced convection. Passive air cooling involves the addition of heat sinks and finned surfaces to maximise the surface area of a component and increase heat losses via natural convection, therefore no additional energy consumption is required for cooling. It is advantageous to maximise the surface area in active cooled systems also as this increases the rate of heat loss.

In many proposed active air-cooled PV systems, parallel plates are affixed to the underside of the panel with perpendicular channels between that control and direct the airflow, while increasing the surface area in contact with the air stream. This type of system can be seen in studied in [184–187] and in Figure 3-10. Air flowrates can be controlled to affect the rate of heat removal and air systems typically have lower operating costs than active liquid systems. Forced air cooling has been shown to be effective at reducing the temperature of PV panels and is particularly effective in low temperature environments, where average ambient air temperature is lower [177] and in cooler climates there is the potential of using the removed heat for space heating or other useful benefit in hybrid photovoltaic-thermal (PV-T) generation [188], where both electricity and heat can be generated.

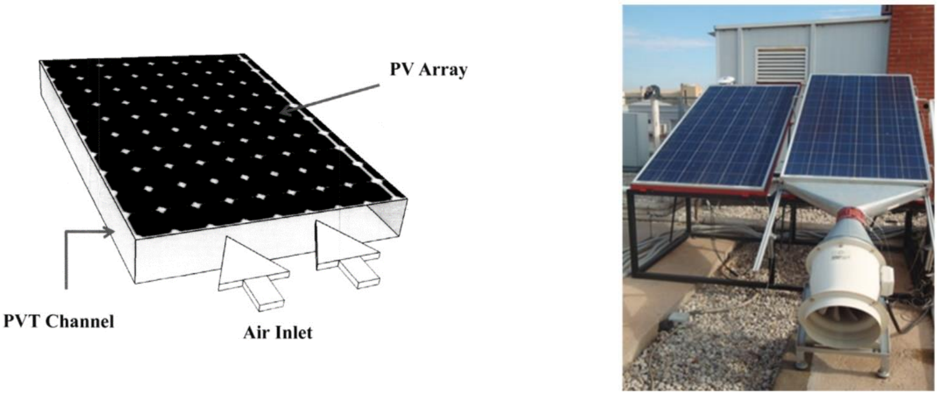

(a) **(b)**

Figure 3-10. Proposed active air-cooling mechanisms for PV panels [185,187]

For passive air-cooling systems, finned heat sinks can be affixed to the underside of the PV modules to maximise surface area contact with air and therefore maximise losses from natural convection. Hernandez-Perez et al. present a comparison of numerous passive, air-cooled heat-sink experimental studies and show effectiveness ranging from between 0.22-6°C drop in temperature depending on the size and design of fins that are implemented [189]. Additionally, Naghavi et al. demonstrated the benefit for elevation from the mounting surface to allow for maximal heat losses from natural convection. The study found that for roof-mounted PV panels, a mean difference of 18°C was observed between panels directly mounted to a roof and one elevated 0.2m from the roof surface [190]. Natural air cooling is the cheapest and simplest heat management technique for PV panels. Maximising heat loss from passive air cooling is low cost, requires no maintenance and components are highly durable. However, techniques are less impactful at cooling when compared to active air cooling other passive methods, and possesses irregular and variable functionality depending on current local weather conditions.

3.3.1.2 Water Cooling

Water cooling has been suggested for the thermal management of solar PV panels. The utilisation of water for PV temperature reduction feature two main approaches, top-side cooling, and underside water circulation.

For top side cooling, investigations focus of spraying or running water over the panel surface to remove heat via evaporation and convention. Krauter et al. have investigated the benefits of running water over the surface of the PV modules to combine the evaporative and convective heat loss of the panels. The authors suggest this method could be reduce irradiation reflection and report a net gain of 8% power considering the energy required to operate the pump [191]. Raju et al. performed similar research into a water spraying method and report efficiency increases from 9.4 to 14.57% from spraying, however the energy required to operate the pump for this exceeded the energy gained from the increase in panel efficiency [192]. Furthermore, Nižetić et al. performed a double spraying experiment and demonstrated average temperature reductions of the PV panel from 54 to 24°C, with a 5.9% increase in electrical conversion efficiency. The authors concluded that their proposed cooling method was not viable in terms of power consumption or water usage but could be a feasible system if the cleaning benefit of the water system is considered also [193]. Hadipour et al. also tested a water-spray based cooling system in a variety of operation modes. They reported an electrical power output increase of 25.9% and calculated the levelized cost of electricity (LCOE) of the power produced with the spraying mechanism was close to that with without any cooling. Therefore, the authors suggest that their spraying method has potential to be justifiable in instances where temperature effects permanently damage or stop the panels from working but cannot on temperature reduction and associated efficiency gains alone [194].

For underside cooling, investigations target the capturing of the thermal energy extracted from water-based heat exchange systems, similar to the air-based PV-T systems. Bahaidarah et al. studied a thermal collector fitted to the underside of a PV module that circulated water with a pump. The extracted waste heat was stored in a hot water tank. With their system, they achieved a 20% reduction in panel temperature and 9% increase in electrical power output [195]. With these combined PV-T systems there are challenges with how to usefully utilise the captured heat. There are also limitations on the scale at which these systems can be conducted as well as the necessity of local water availability.

3.3.1.3 Phase Change Materials

When a material undergoes a change in state, energy is absorbed or released. Therefore, certain materials are suited for use as a store of thermal energy because they have high heat of fusion relative to their sensible heat; these are commonly referred to as Phase Change Materials (PCM). The implementation of PCM for the cooling of solar panels has been extensively explored [196,197]. Proposed systems typically integrate a container packed with a PCM to the underside of a PV panel, with or without the presence of fins or meshes to maximise heat exchange area. Stalin et al. demonstrated an integrated system of PV with novel PCM to improve the efficiency of PV generation through the reduction in panel temperature. Integrating paraffin-CuO material reserve on the back of a panel resulted in an overall 1.2% increase in panel efficiency from 15.4% to 16.5% [198]. Similarly, a PV-PCM system constructed by Stropnik et al. achieved overall electrical generation increase of 9.2% over a one-month period, when compared to a reference panel without cooling [199]. Despite their effectiveness at reducing panel temperature and improving PV generation efficiency, PCM integration is not currently economically viable. PCMs integrated with PV appear to be best suited for regions that have consistent high levels of insolation and high ambient temperatures throughout the year. Chandel et al. suggest PV-PCM systems may find the greatest use case in roof integrated systems, where the underside of panels do not have air exposure and there is also the potential for heat reuse [197].

3.3.1.4 Heat Pipes

Heat pipes contain a volatile liquid that readily evaporates when in contact with a hot surface, extracting heat. The vapour can condense when it comes into contact with the cooler end of the pipe, releasing the latent heat. The liquid can then return to the hot surface via capillary action or gravity and the cycle can begin. They provide effective passive cooling methods in many applications or can be made into active cooling methods with the circulation of air or water across the condensing end to quickening the condensation of the vapour.

The implementation of heat pipes for the cooling of PV panels has been proposed. Tang et al. compared to passive cooling of a heat pipe system with water and air, in which the condensing end of the heat pipe system was surrounded by air and submerged in water. For the air and water cooling with the heat pipe system, overall energy generation in a day was increased by 2.6 and 3% respectively [200]. The primary benefits of employing heat pipes are the passive nature and simplicity of the mechanisms.

3.3.1.5 Thermoelectric Cooling

A thermoelectric module (TEM) can convert a heat directly into electric current from the application of a large temperature differential between two terminals. However, more commonly TEMs are used as heat pumps, where current is applied, creating a source of heating or cooling, removing heat from one terminal and rejecting heat at another terminal.

It is proposed that the voltage generated from the PV modules can be integrated with a TEM to either to actively cool the panels or to generate additional electrical power by the TEM using the waste-heat from the panel [201]. Salehi et al. demonstrated the use of an integrated TEM PV to cool the panel and produce additional power with the waste heat for a small-scale panel; the authors achieved a 10.04°C reduction and cell temperature and 10.5% increase in overall power production [202]. The scalability and cost of the application of TEM in such a way are unclear so it appears unlikely that this technique will find widespread adoption.

3.3.1.6 Transparent Coatings

The incorporation of transparent coatings (photonic crystal cooling) on the surface of PV panels to reduce surface operating temperatures can be a method to improve the electrical generation efficiency [177]. The coating can act as a visibly transparent thermal blackbody that can allow light through to the PV module while maximising radiative losses. Zhu et al. demonstrate the concept of this method for cell temperature reduction on a 0.1m-diameter cell achieving a reduction in temperature of 13°C [203]. Zhao et al present a methodology using transparent coatings and radiative cooling from photonic crystals to provide increased PV efficiency through panel cooling and provide a nocturnal cooling effect through radiation, in a hybrid system [204]. As the technology is immature and expensive, it is currently difficult to estimate the long-term viability of this method for PV cell improvement. If the cost and durability of the coatings are improved, they could present an effective passive method for improving the electrical conversion efficiency through panel cooling.

3.3.1.7 Discussion of Heating Mitigation Methods

Of the proposed methods for reducing the temperature of PV panels, none are currently employed widely. This suggests a lack of maturity in each system or a lack of economic viability. Until the cost of employing a method is cheaper than increased economic benefit from excess generation, it is unlikely that these methods will be adopted, with an acceptance that generation losses arising from high panel temperatures is inherent to PV generation. The primary benefits and limitations of each of the described cooling methods are presented in Table 3-2.

Table 3-2. Summary of heating mitigation methods for PV panels

Method	Advantages	Disadvantages
Natural air cooling	• Simple solution • Passive method	• Relatively low cooing effect • Waste of potential heat resource
Forced air cooling	• Good cooling effect • Potential for hybrid electrical/thermal generation	• Requires energy input
Water cooling	• Strong cooling effect • Potential for hybrid electrical/thermal generation	• Water requirement • Requires energy input
Phase change materials	• Passive method • Good temperature reductions possible	• Not economically viable

Heat pipes	- Passive method - Simple device	- Relatively weak cooling effect
Thermoelectric cooling	- Moderate cooling effect - Potential for additional electricity generation from heat source	- Complex system - Cost concerns
Transparent coatings	- Passive method - Good temperature reduction	- Expensive technology - Lack of durability - Unclear if technology will scale

As will many of the proposed anti-soiling methods, the water dependent methods for cooling are limited by cost and location particularly in arid regions. Active methods seem to be unviable for heating mitigation alone, as the energy input for cooling will always exceed the energy benefit. Therefore, a key feature of active methods must be a combined benefit, be that extraction of useful heat for an additional purpose as in PV-T systems, or extension to system lifetime whereby lifetime energy output of the system may be greater and economic benefits may be greater because of the additional years of operation.

3.4 Proposed PV-CAES System for Panel Cleaning and Cooling

Chapter 2 introduced the benefits that EES, and specifically CAES, can bring to renewable power generation and thus far this chapter has highlighted the challenges arising from PV panel soiling and heating, as well as mitigations strategies. Now, a system for ameliorating the soiling and heating issues with PV generation is presented.

It is proposed that integrating a CAES system directly with PV generation can combine the conventional benefits to renewable generation from EES (reduction in curtailment etc.) with the additional benefits of panel cooling and cleaning. CAES systems generate compressed air as the intermediate energy store; if this resource is utilised in a secondary way, a system can be created whereby the PV panels can be cleaned and cooled. The high-pressure air can be allowed to flow over the surface of the PV panels which will remove present dust and lower the operating temperature of the modules by forced convection. Therefore, it is suggested that this combined PV-CAES system can increase the overall energy efficiency of the PV generation. If the CAES system is charged via excess PV generation, the system has the potential to reduce the rate of curtailment. The system concept is displayed in Figure 3-11.

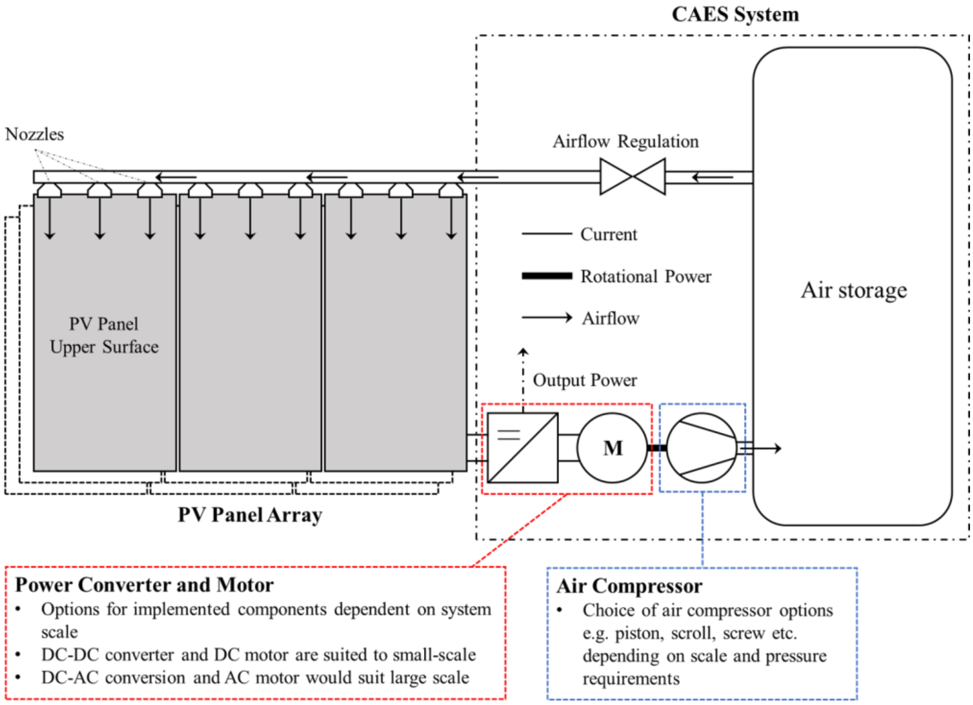

Figure 3-11. Proposed integrated PV-CAES system for panel cleaning and cooling

The system is comprised of a PV panel or array of panels and an adapted CAES system. The PV generation is capable of delivering power to an external source e.g., an electrical grid or load and the CAES system is connected in addition to this. The CAES system is comprised of a power converter and a motor to drive the compressor. The electrical motor can be a DC or AC motor depending on the suitability for the system scale or configuration. For small-scale systems DC motors are more widely available so DC-DC conversion would be required to integrate the motor. If the implemented system is of a large-scale, an AC motor will be more suited, therefore DC-AC inversion will be required for the motor supply. For a small-scale DC-based system, the implementation of a DC machine simplifies the system by not requiring power inversion and thus the DC-DC converter can be used to control the operation of the motor. The motor is coupled to an air compressor and drives air into an air store. There are several candidate compressor types available, with component choice dependent on a number of factors such as pressure requirements, efficiency and cost. Widely used air compressors include rotary-screw, reciprocating piston and scroll-type. Furthermore, the choice of air store will be dependent on the scale of the system. Regarding the system concept, the air tank could have the option to feed an expander and operate in a way to recover electrical power from the CAES or the generated air can be used solely for cleaning and cooling purposes. A series of pipes and nozzles will deliver the air to the panel surface and must be regulated through a pneumatic controller to open and close the system. The nozzles can be positioned in several ways but should be fixed. There are few moving parts in the cleaning system, thus the system should operate robustly with the potential for full automation. The proposed system is water free, which has been identified as one of the primary constraints in the implementation of cooling and cleaning technologies in PV generation. Of the reviewed air-based cooling methods, none propose upper-surface blowing for combined cleaning effects. Forced air cooling has however been investigated with regard to useful heat extraction in combined PV-T systems.

The specific structure of the PV-CAES system studied for the remainder of this thesis considers a small-scale implementation such that the functionality can be tested in a laboratory setting. Therefore, a DC motor-based system is studied and a scroll-type compressor is adopted for analysis. These are introduced here.

3.4.1 DC Motor

A DC motor is determined as the most suitable device for the integration in a small-scale implementation of the system for laboratory demonstration. If a DC machine is implemented, this limits the requirement of power inversion from the PV generation to drive the motor. Additionally, DC motors tend to be simpler to install and require less maintenance than AC alternatives. DC motor modelling is less complex than AC alternatives which will aid in the development of the full-system mathematical model.

3.4.2 Scroll-type Air Compressor

For a small-scale implementation of the system a scroll-type air compressor is adopted. A scroll-type compressor is a form of compressor that pumps air through the meshing of two coupled scroll blades. Compared to alternative compressors that could be implemented in the system, such as reciprocating piston or rotary screw compressors, a scroll-type compressor is chosen here because of their high efficiency, robust nature and minimal maintenance requirement. Furthermore they are compact and quiet and therefore suited to a small-scale lab implementation. Moreover, they can be acquired in a range of sizes and power ratings. Additionally, scroll-type compressors can function normally without need for lubrication. They also exhibit low vibration which further promotes robust operation and long operating lifetime [205]. Therefore, this compressor type is more suited to the application in remote and arid areas [206]. Detailed explanation of their function is outlined in Section 4.4.2. Figure 3-12 displays a cross section of an example scroll-type compressor.

Figure 3-12. Internal mechanism of typical scroll-type compressor [207]

3.4.3 Air Store

For the PV-CAES system that has been proposed, it is recommended that a small-scale above ground air tank is used as the storage medium as this is applicable to a laboratory environment. This will allow for the operation of the system in any location and will decouple the system from the requirement of large underground storage capabilities, though in theory this could also be suitable, the concept must be proven before examining large-scale implementation. Additionally, the small-scale air tank is most useful in terms of system assessment and initial study to assess the feasibility of improving PV generation from the compressed air cleaning and cooling.

3.5 Summary

PV generation faces many sources of inefficiencies. Firstly, panel soiling accounts for a large reduction in potential generation and impacts the overall lifetime of the solar modules. Secondly, high panel temperatures reduce electrical conversion efficiency of PV generation, exacerbated by the coincidence of good solar availability and high ambient temperatures. Thirdly, potential power generation is lost because of curtailment owing to the inherent variability and uncertainty in renewable generation.

Of the available techniques for mitigating soiling effects on PV panels, manual cleaning is the dominant strategy but this faces limitations in water availability and labour costs. Furthermore, lesser practiced and emerging methods have shown effectiveness in laboratory settings, but face their own limitations, primarily in terms of cost, scalability and durability.

Regarding temperature induced inefficiencies, there is not widespread application of heat mitigation strategies, although a wide number of mechanisms have been proposed. Active cooling methods are limited by the energy requirement leading to an overall net loss in energy and are only justifiable if a secondary benefit it achieved. Furthermore, passive methods have not achieved a level of technological maturity to make them economically viable.

A system integrating CAES with the PV generation is proposed. The conventional benefits to renewable generation from the integration of EES can be achieved and additionally, the capability of cooling and cleaning to improve the PV generation efficiency is provided from use of the compressed air. The proposed design is a water-free and automatable method that has the potential to be used across a wide range of scales of PV generation. The components for a small-scale laboratory demonstration of the proposed system structure are described, comprising of a DC-based system and scroll-type air compressor with above ground air vessel.

Chapter 4 – Dynamic Mathematical Modelling Study of the Proposed PV-CAES System

This chapter derives a full-system dynamic mathematical model for the PV-CAES system for panel cleaning and cooling with specific components proposed in Chapter 3. These key components and mechanisms are discussed with the construction of the full-system model highlighted at the end of the chapter. The functionality of the constructed dynamic full system mathematical model is demonstrated through the development of control for the charging process of the system.

Parts of the derived mathematical model have been described in the publications: "*Study on the cleaning and cooling of solar photovoltaic panels using compressed airflow*" in Solar Energy by D. Li, the author M. King, M. Dooner, S. Guo and J. Wang [208] and "*Mathematical Modelling of a System for Solar PV Efficiency Improvement Using Compressed Air for Panel Cleaning and Cooling*" published in Energies by the author M. King, D. Li, S. Ghosh, J. N. Roy, C. Chakraborty and J. Wang [209]. Furthermore, the control of the charging process presented at the end of this chapter is adapted from work presented by the author at the International Conference on Automation & Computing (ICAC), University of Portsmouth, UK, 2-4 September 2021 as "*Modelling and control of the charging process of a PV -compressed air system for efficiency improvement from panel cleaning and cooling*" [210].

4.1 PV Panel Generation

A PV module can be represented as a simplified circuit comprised of a photodiode as a current source within a single diode circuit [211,212]. This is shown in Figure 4-1.

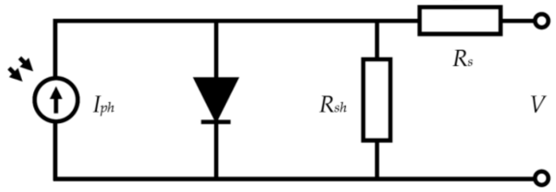

Figure 4-1. Single-diode representation of PV module

The photocurrent, I_{ph}, generated by the photodiode, is determined as a function of the short circuit current (the maximum output current capability, achieved when the operating voltage is zero), I_{sc}, the short-circuit temperature coefficient, k_i the cell temperature, T_p, the cell reference temperature, T_{ref}, and the solar irradiance, G, falling on the photodiode. This is given in Equation (4.1).

$$I_{ph} = \frac{G\left[I_{sc} + k_i\left(T_p - T_{ref}\right)\right]}{1000} \tag{4.1}$$

with:

I_{ph}	Photocurrent	[A]
I_{sc}	Short-circuit current	[A]
k_i	Short-circuit temperature coefficient	[%·°C^{-1}]
T_p	Panel temperature	[°C]
T_{ref}	Cell reference temperature	[°C]
G	Solar irradiance	[W·m^{-2}]

The cell reference temperature, T_{ref}, is typically taken as 25°C and the short-circuit temperature coefficient is a measure of the change in current generating potential of the cell with respect to temperature, typically in the range of 0.05% °C^{-1}.

The diode saturation current, I_0, is a function of the reverse-saturation current, I_{rs}, cell temperature and reference temperature, electron charge constant, q, semiconductor band gap energy, E_{g0}, the diode ideality factor, n, and the Boltzmann constant, K_b, shown in Equation (4.2).

$$I_0 = I_{rs}\left(\frac{T_p}{T_{ref}}\right)^3 \exp\left[\frac{qE_{g0}\left(\frac{1}{T_{ref}} - \frac{1}{T_p}\right)}{nK_b}\right] \tag{4.2}$$

where:

I_0	Diode saturation current	[A]
I_{rs}	Reverse saturation current	[A]
q	Electron charge constant	[C]
E_{g0}	Semiconductor bandgap	[eV]
n	Diode ideality factor	[-]

K_b	Boltzmann constant	[$\text{m}^2\cdot\text{kg}\cdot\text{s}^{-2}\cdot\text{K}^{-1}$]

The electron charge is a fixed constant of 1.602×10^{-19} C, as is the Boltzmann constant at 1.381×10^{-23} $\text{m}^2\cdot\text{kg}\cdot\text{s}^{-2}\cdot\text{K}^{-1}$. The diode ideality factor represents how similar the practical diode matches the ideal diode equation, and the semiconductor bandgap is the minimum energy require to excite and electron in the semiconductor to break free and carry charge, approximately 1.1 eV for silicon modules.

The reverse-saturation current is calculated given the short-circuit current, electron charge constant, open circuit voltage, V_{oc}, diode ideality factor, number of cells in series connection, N_s, Boltzmann constant and cell temperature. This relationship is described by Equation (4.3).

$$I_{rs} = \frac{I_{sc}}{\exp\left[\frac{qV_{oc}}{nN_sK_bT_p}\right] - 1} \tag{4.3}$$

and:

V_{oc}	Open-circuit voltage	[V]
N_s	Number of cells in series connection	[-]

where the open circuit voltage is the potential measured between the output terminal when the circuit is not connected.

The current through the shunt resistor, I_{sh}, is determined from the operating voltage, V, the current through the load, I, the series resistance, R_s, and the shunt resistance, R_{sh}. The relationship is given by Equation (4.4).

$$I_{sh} = \left(\frac{V + IR_s}{R_{sh}}\right) \tag{4.4}$$

where:

I_{sh}	Shunt resistor current	[A]
V	Operating voltage	[V]

R_s	Series resistance	[Ω]
R_{sh}	Shunt resistance	[Ω]

Series resistances present themselves from resistances in the contacts between the silicon and casings and reduce the performance of real PV modules from the ideal I-V curves. Shunt resistances usually arise from manufacturing defects and allow alternate paths for currents therefore reducing efficiency. A cell with a high shunt resistance fits the ideal I-V curve more closely therefore.

Finally, the output current can be determined from the photocurrent, saturation current, electron charge constant, operating voltage, output current, series resistance, diode factor, Boltzmann constant, number of modules in series, cell temperature and shunt current – given as Equation (4.5).

$$I = I_{ph} - I_0 \left[\exp\left(\frac{q(V + IR_s)}{nK_b N_s T_p} \right) - 1 \right] - I_{sh} \tag{4.5}$$

The power output of the panel is given as the product of the voltage and current.

$$P_p = VI \tag{4.6}$$

where:

P_p	Panel power output	[W]

The total energy generation from the PV panel, E_p, can be used as a measure of performance comparison. The energy captured by the PV panel is given as the integral of the panel power output with respect to time, given in Equation (4.7).

$$E_p = \frac{1}{3.6 \times 10^6} \int P_p \, dt \tag{4.7}$$

where:

E_p	Panel energy generation	[kWh]

4.2 Dynamic PV Panel Temperature

The temperature of the PV panel needs to be dynamically modelled, subject to both passive and active heating and cooling effects. Although several methods have been suggested for the thermal modelling of PV panels [213,214], these do not allow for the integration of cooling mechanism into the computation. Therefore, a heat-balance approach to the thermal modelling is taken, where the change in temperature of the panel is a result in the imbalance between heat input and heat output from the system. For this, a PV panel can be assumed to be a thin horizontal plate with uniform temperature and properties. The heat balance for the PV panel can be represented by Equation (4.8). When the heat into the system and out of the system are at an equal rate, no temperature change is observed. The calculated panel temperature is used to determine the PV panel operation, in Equation (4.1) – Equation (4.5).

$$\dot{T}_p = \frac{\dot{Q}_{in} - \dot{Q}_{out}}{m_p c_{pp}} \tag{4.8}$$

where:

T_p	Panel temperature	[°C]
Q_{in}	Heat input	[W]
Q_{out}	Heat out	[W]
m_p	Panel mass	[kg]
c_{pp}	Specific heat capacity of panel	[J·kg^{-1}·K^{-1}]

For PV modules, the source of heat input to the panel, Q_{in}, arises from incident solar radiation on the panel surface. A portion of incident radiation is converted to electrical current by the photodiodes, but the majority of energy is stored as sensible heat in the form of an increase in a panel temperature. This is given in Equation (4.9).

$$\dot{Q}_{in} = GA(1 - \epsilon) \tag{4.9}$$

where:

G	Irradiance	[W·m^{-2}]
A	Panel area	[m^2]

ϵ	Electrical conversion efficiency	[-]

For the determination of heat from the panel, pure convection is assumed as radiative effects are low relative to convective effects within the typical operational temperature range. Therefore, the total heat out of the panel, Q_{out}, can be represented by Equation (4.10):

$$\dot{Q}_{out} = hA\left(T_p - T_a\right) \tag{4.10}$$

with:

h	Heat transfer coefficient	[W·m^{-2}·K^{-1}]
T_a	Ambient temperature	[°C]

The overall heat transfer coefficient is calculated from Equation (4.11):

$$h = \frac{NuK}{L_c} \tag{4.11}$$

where:

Nu	Nusselt number	[-]
K	Thermal conductivity	[W·m^{-1}·K^{-1}]
L_c	Characteristic length	[m]

Owing to the assumption that the panel is a thin horizontal plate of constant temperature, the characteristic length, L_c, is determined with Equation (4.12).

$$L_c = \frac{A}{P} \tag{4.12}$$

where:

P	Panel perimeter	[m]

The mean film temperature must be calculated for the determination of the air properties, as these vary with temperature. It is the average temperature of the panel and the ambient air, given by Equation (4.13):

$$T_f = \frac{T_p + T_a}{2} \tag{4.13}$$

where:

T_f	Mean film temperature	[°C]

As the aim is to develop a dynamic model that can represent the panel temperature under natural conditions as well as subject to the proposed cooling mechanism, there are two cases to consider for convective heat transfer from the panel: natural and forced, dependent on if the proposed system is currently blowing air over the panel surface.

4.2.1 Natural Convection

Natural convective currents occur from differences in heat transfer fluid density because of temperature differences in the fluid (in this case air). For the periods when air is not blowing over the surface of the panel, natural convection is the heat-loss mechanism. The natural convective heat-balance diagram is displayed in Figure 4-2.

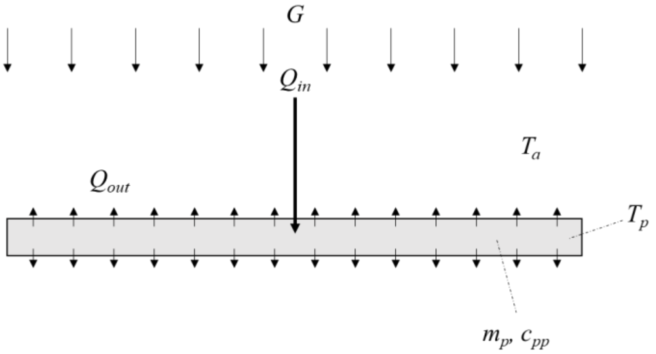

Figure 4-2. Panel natural convection heat balance

For natural convection, the Rayleigh number, Ra, must be calculated using Equation (4.14).

$$Ra = \frac{g\beta \Delta T {L_c}^3}{\nu \alpha_a} \tag{4.14}$$

where:

Ra	Rayleigh number	[-]
g	Gravitational acceleration	[m·s^{-2}]
β	Time constant	[°C^{-1}]

ΔT	Panel-ambient temperature difference	[°C]
ν	Kinematic viscosity	[$m^2 \cdot s^{-1}$]
α_a	Thermal diffusivity	[$m^2 \cdot s^{-1}$]

The kinematic viscosity and thermal diffusivity are both evaluated at the film temperature from look-up tables. The time constant, β, is the inverse of the film temperature, given in Equation (4.15).

$$\beta = \frac{1}{T_f} \tag{4.15}$$

From the determination of the Rayleigh number, empirical correlations for the average Nusselt number can be determined through Equation (4.16) [215].

$$Nu = \begin{cases} 0.54Ra^{1/4} & 10^4 \leq Ra < 10^7 \\ 0.15Ra^{1/3} & 10^7 \leq Ra \leq 10^{11} \end{cases} \tag{4.16}$$

The Nusselt number is then used in Equation (4.11) to determine the overall heat transfer coefficient and total heat loss.

4.2.2 Forced Convection

Forced convection occurs when the heat transfer fluid is driven by an external source; it results it greater heat loss than natural convection. For the periods when the system is delivering air to the panels, correlations for forced convection must be used. It is assumed that the air blowing over the surface of the panel is uniform across the length of the panel and can reach every point on the panel surface. The forced convective heat balance is demonstrated in Figure 4-3.

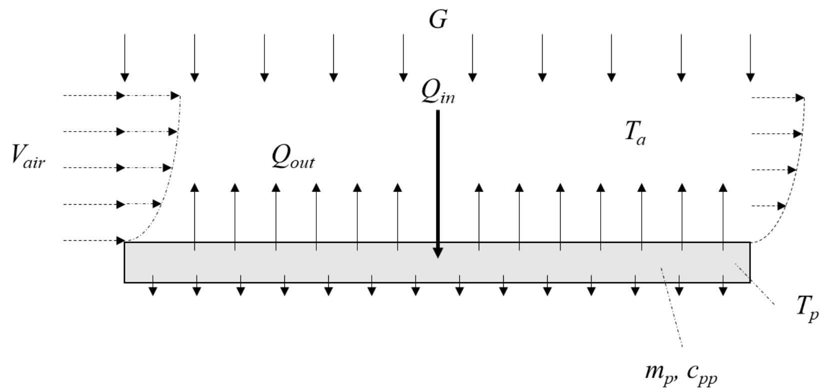

Figure 4-3. Panel forced convection heat balance

For forced convective effects, the Reynold's number for the flow must be calculated:

$$Re = \frac{V_{air} l}{\nu} \tag{4.17}$$

where:

Re	Reynolds number	[-]
V_{air}	Air Velocity	[m·s^{-1}]
l	Panel length	[m]

The kinematic viscosity, ν, is evaluated at the film temperature. Additionally, the Prandtl number, Pr, must be evaluated at the film temperature. Once these are obtained, correlations for the average Nusselt number can be used. This is given in Equation (4.18) [215].

$$Nu = \begin{cases} 0.664 Re^{1/2} Pr^{1/3} & Re < 5 \times 10^5 \\ \left(0.037 Re^{4/5} - 871\right) Pr^{1/3} & 5 \times 10^5 \leq Re \leq 10^7 \end{cases} \tag{4.18}$$

with:

Pr	Prandtl number	[-]

As with the natural convection case, Nu, can be used to determine the overall heat transfer coefficient and Equation (4.11) used to determine the panel temperature.

Note for the modelling, natural convection continuously occurs from the underside of the panel. When the system is actively cooling the top side of the panel the heat loss mechanism switches from natural to forced convection, as in Figure 4-3. Additionally, convective effects occur regardless of the current heat input with both heat in and heat out computed simultaneously.

4.3 Panel Soiling and Cleaning

4.3.1 Particle Adhesion

To model the potential for air cleaning of PV panels, the particle soiling and detachment criteria must be established. For this, particles are assumed to be uniformly distributed on a smooth panel surface of uniform particle diameter. When dust is present on the surface of the panel, solar radiation is blocked from reaching the photodiodes so a reduction in electrical power output is observed. The modelling approach assumes that the air blows uniformly across the entire surface of the panel with all areas cleaned evenly and subject to the same air velocity.

Particles adhere to the surface of the panels by three primary forces, Van der Waal forces, F_{VdW}, electrostatic force, F_e, and capillary force, F_c. The dominant forces on acting between the panel and the particles are shown in Figure 4-4.

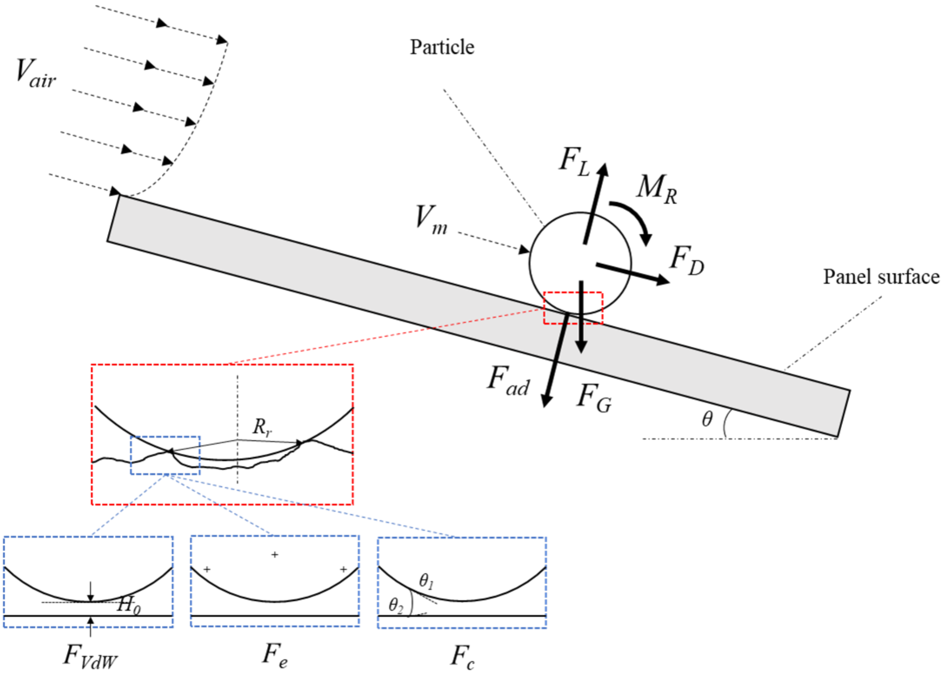

Figure 4-4. Adhesion mechanisms and detachment mechanisms of a particle on the panel surface, subject to airflow

The Van der Waals forces arise from interacting dipoles and at low humidity levels are the dominant form of interaction between the particle and the panel surface [216]. An expression for the van der Waal forces between the particle and the panel surface is given in Equation (4.19) [217].

$$F_{VdW} = \frac{A_h R_p}{6{H_0}^2} \tag{4.19}$$

where:

A_h	Hamaker constant	[J]
R_p	Particle radius	[m·s^{-1}]
H_0	Closest distance between surfaces	[m]

The Hamaker constant reflects the strength of the Van der Waals forces between two interacting bodies and the closest distance reflects surface roughness of the material. For glass interaction to dust the Hamaker constant and closest-distance have been reported as 7×10^{-20} J and 0.3 nm respectively [216].

The electrostatic force between the interacting particle arises from the respective charges of the interacting bodies [218]; they can either be attractive or repulsive in nature. An equation for the electrostatic force between a particle and the panel surface is given in Equation (4.20) [219].

$$F_e = \frac{q_p^2}{16\pi\epsilon_0 {R_p}^2}\left[\frac{1}{(\zeta + \zeta^2)\left(1 + 0.5\log\left(1 + \frac{1}{\zeta}\right)\right)}\right] \tag{4.20}$$

where:

q_p	Particle charge	[C]
ϵ_0	Vacuum permittivity	[F·m^{-1}]
ζ	Ratio of closest distance to particle radius	[-]

The particle charge of a particle >0.1μm can be approximated with Equation (4.21) [220].

$$q_p = 2.37 \times e \times \sqrt{2R_p\ [\mu m]} \tag{4.21}$$

The vacuum permittivity is reported as 8.854 × 10^{-12} F·m^{-1} [126] and used in the calculations as stated.

Capillary forces exist when a liquid is present between the particle surface and the particle. This can be a result of humidity in the air; with low humidity values, capillary forces will not dominate the adhesion mechanism. An expression for the capillary forces between the particles and the panel surface is given in Equation (4.22).

$$F_c = 2\pi R_p \psi(\cos\theta_1 + \cos\theta_2) \tag{4.22}$$

with:

ψ	Liquid surface tension	[N·m^{-1}]
θ_1	Contact angle	[°]
θ_2	Contact angle	[°]

The contact angles refer to the angle made by the liquid contacting between the surface and the adhered particle. As such the total force with which the particle adheres to the panel surface is the sum of the present forces, given by Equation (4.23).

$$F_{ad} = F_{vdW} + F_e + \mathrm{F_c} \tag{4.23}$$

where:

F_{ad}	Total adhesion force between particle and panel	[N]

Figure 4-5 demonstrates examples of the relative strength of the adhesive forces of particles on the surface of PV modules. Parameters are as previously stated with contact angles of θ_1 and θ_2 taken as 60° and 45° respectively for the demonstration of the capillary forces. If capillary forces are present owing to the presence of moisture, they will be the dominant adhesion mechanism. With the absence of moisture, Van der Waals forces will be the dominant adhesion mechanism. Electrostatic forces are 3 orders of magnitude smaller than the other adhesive forces, so are unlikely to influence the detachment of the particles in a significant manner.

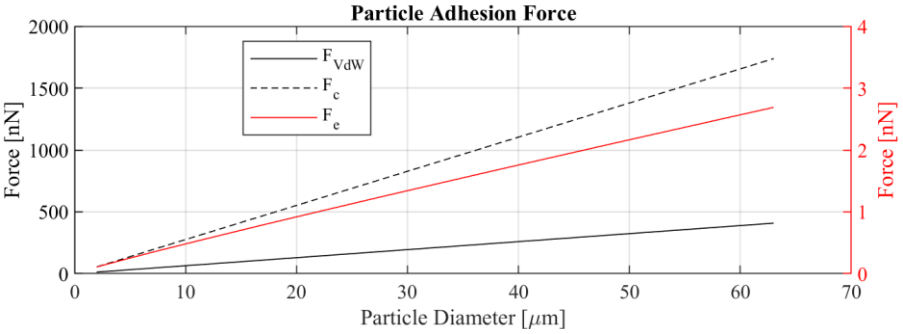

Figure 4-5. Relative strength of adhesion forces

4.3.2 Particle Detachment Modes

Particles adhered to the panel surface will be removed by air blowing at a high velocity over the panel surface. The air is designed to be blowing parallel to the panel surface so will act in a direction perpendicular to the particle adhesion force. The air acting upon the particle generates a drag force, F_D, a lift force, F_L, and a rolling moment, M_r on the particle, this is observed in Figure 4-4. The shear velocity, V_{sh}, at the surface of the panel is calculated from the free stream velocity, V_{air}, and the surface correction factor C_f, and occurs from the no-slip condition on the panel surface, given in Equation (4.24) [165]. The shear velocity relates to the shear stress and characterises the stress at the boundary layer of the flow.

$$V_{sh} = \sqrt{\frac{C_f {V_{air}}^2}{2}} \tag{4.24}$$

with:

$$C_f = 0.0592 \left(\frac{V_{air} l_p}{2}\right)^{-0.2} \tag{4.25}$$

where:

V_{sh}	Shear velocity	[m·s^{-1}]
C_f	Skin friction coefficient	[-]
l_p	Panel length	[m]

The shear velocity is used to determine the mean air velocity, V_m, at the centre of the adhered particle:

$$V_m = \frac{\Gamma R_p {V_{sh}}^2}{\nu} \tag{4.26}$$

where:

V_m	Mean velocity at particle centre	[m·s^{-1}]
Γ	Wall coefficient	[-]

The wall coefficient is constant at 1.84 [165] and the kinematic viscosity is evaluated from a look-up table dependent on air temperature. The resultant drag force from an air stream is then given by Equation (4.27).

$$F_D = \frac{C_D f \rho_{air} \pi {R_p}^2 V_m^2}{2C_{cu}} \tag{4.27}$$

where:

F_D	Drag force	[N]
C_D	Drag coefficient	[-]
f	Near-wall correction factor	[-]
ρ_{air}	Air density	[kg·m^{-3}]
C_{cu}	Cunningham correction factor	[-]

The near-wall correction factor, f, is taken as 1.7009 and accounts for the greater force exerted by a fluid to the particle on the wall than if suspended in the fluid [218] and the Cunningham correction factor relating to the corresponding wall effect [221]. The coefficient of drag is given as a function of the Reynolds number of the particle, Re_p [222] and shown in Equation (4.28).

$$C_D = \begin{cases} \frac{24}{Re_p}\left(1 + \frac{1}{6}{Re_p}^{2/3}\right) & Re_p \leq 1000 \\ 0.44 & 1000 < Re_p \leq 2 \times 10^5 \end{cases} \tag{4.28}$$

where:

$$Re_p = 2\Gamma\left(\frac{R_p V_{sh}}{\nu}\right)^2 \tag{4.29}$$

and:

$$C_{cu} = 1 + \frac{\lambda}{R_p}\left(1.257 + 0.4\exp\left(-1.1\frac{R_p}{\lambda}\right)\right) \tag{4.30}$$

and:

Re_p	Particle Reynolds number	[-]
λ	Molecular mean free path	[m]

The molecular mean free path is the shortest average distance a particle will move in the flow without changing direction, for air it is 0.07 µm at ambient conditions [218]. Additionally, the resultant rolling moment acting on the particle as a result of the blowing air is given by Equation (4.31):

$$M_R = \frac{8\Gamma f_m \rho_{air} \pi {R_p}^3 V_{sh}^2}{C_{cu}} \tag{4.31}$$

where:

f_m	Wall correction factor	[-]

with f_m given as 0.944 [222]. The resulting lift force F_L arising from the air stream is determined from Equation (4.32).

$$F_L = \frac{11.904\rho_{air} {R_p}^4 V_{sh}^4}{\nu^2} \tag{4.32}$$

Furthermore, gravity is acting upon the particle and contributes to the adhering of the particle upon the surface of the panel, dependent on the angle of inclination of the panel. The weight of the adhered particle is given in Equation (4.33).

$$F_G = \frac{4\pi {R_p}^3 \rho_d g}{3} \tag{4.33}$$

where:

ρ_d Particle material density [kg·m^{-3}]

g Gravitational acceleration [m·s^{-2}]

4.3.3 Particle Detachment Criteria

There are three detachment conditions for the particles when blown by an air jet, they can either roll, lift away or slide [126].

Particle lift-off will occur if the lift force is greater than the adhesion force plus the component of the particles weight acting perpendicular to the panel. The lift condition is given in Equation (4.34).

$$F_L \geq F_{ad} + F_G \cos\theta \tag{4.34}$$

Particle sliding will occur if the resultant drag force on the particle is greater than the perpendicular force of the particle to the panel (the sum of the adhesion force, perpendicular weight and lift force) multiplied by the coefficient of friction, minus the component of the particles weight acting parallel to the panel surface. The particle sliding criterion is given by Equation (4.35).

$$F_D \geq \mu(F_{ad} + F_G \cos\theta - F_L) - F_G \sin\theta \tag{4.35}$$

where:

μ Coefficient of friction [-]

The value of μ is dependent on the panel material, for glass materials as are typical in PV surfaces it is provided as 0.4 [223].

Finally, the rolling condition is determined by performing a moment balance around the rolling point of the particle [224]. The criterion for predicting particle rolling is given in Equation (4.36).

$$(F_D + F_G \sin\theta)\left({R_p}^2 - {R_r}^2\right)^{1/2} + M_R \geq (F_{ad} + F_G \cos\theta - F_L)R_r \tag{4.36}$$

with:

R_r Particle contact radius [m]

The particle contact radius can be of a range of values but has been shown to be approximately $0.01R_p$ for adhered particles [216,225].

Under the detachment criteria, if the air velocity is sufficiently great, adhered particles will be removed by one of the detachment criteria, whichever possesses the lowest threshold velocity. Figure 4-6 demonstrates the required shear velocities and air velocities to remove particles from a flat panel, 1m in length via the respective detachment criteria.

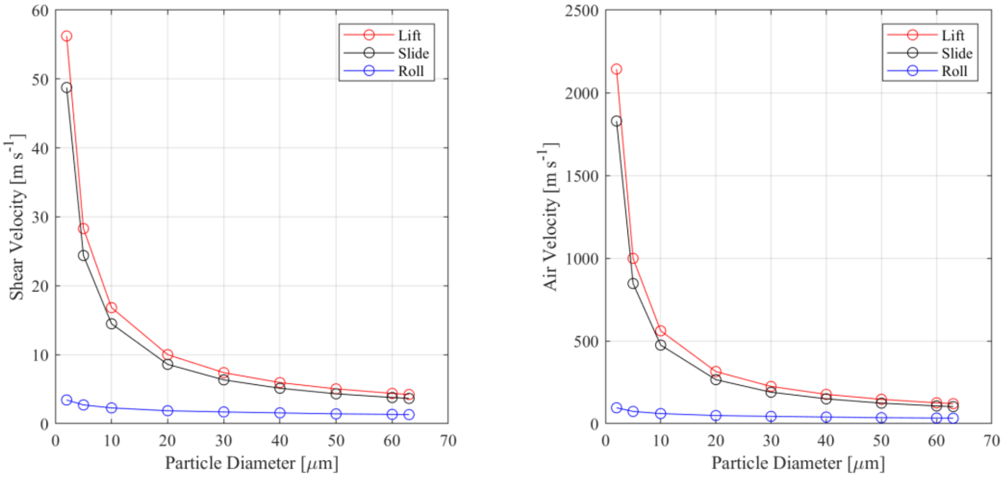

(a) **(b)**

Figure 4-6. Shear and air velocities for particle detachment

Figure 4-6 demonstrates the detachment mode for particles in the range contribute most to PV generation soiling losses as discussed in Chapter 3 (from 2-63μm diameter [126]). Across the range of particle diameters, the rolling detachment criterion will be achieved at lowest air velocities first, i.e., particles will never be removed via the lift or sliding mechanisms. Additionally, it can be concluded that larger particles are removed more easily from the panel surface, being detached at lower air velocities. Larger particles, greater 63μm are more likely to be able to be removed by natural wind blowing across the panel surface and therefore should contribute less to panel losses.

4.3.4 Soiling Power Loss

The estimation of power loss from soiling is determined from the impact of the deposited particles to the radiative transmittance into the modules [129]. Equation (4.37) provides an estimation of the soiling loss in terms of a factor that is multiplied to the incident solar radiation, reducing input radiation to the modules.

$$F = 1 - \frac{m\left(E_{abs} + \beta_f E_{scat}\right)}{A} \tag{4.37}$$

where:

F	Soiling power loss factor	[-]
m	Total dust mass	[kg]
E_{abs}	Absorption efficiency	[$\mathrm{m^2 \cdot g^{-1}}$]
β_f	Particle up-scatter fraction	[-]
E_{scat}	Scattering efficiency	[$\mathrm{m^2 \cdot g^{-1}}$]
A	Panel surface area	[$\mathrm{m^2}$]

The absorption efficiency, E_{abs}, particle up-scatter fraction, β_f, and scattering efficiency relate to the interaction of radiation with particles. Their values have been reported as 0.02, 0.02 and 1.0 respectively [129].

4.4 Air Compression System

As introduced in Section 3.4. The primary components of the CAES system to be implemented is comprised of a DC motor driving a scroll-type air compressor. The compressor feeds a small-scale air tank, which then discharges through a series of pipes and nozzles to deliver air to the surface of the PV panel. Mathematical models of the subcomponents of the CAES system are outlined in this section.

4.4.1 DC Motor

A DC permanent magnet synchronous motor (PMSM) is implemented as the driver of the compressor, owing to the reasons laid out in Section 3.4. The rotational acceleration of the rotor, $\ddot{\theta}$, is a function of the rotor inertia, J_m, the rotor torque, τ, the viscous damping factor, b, the rotor speed, $\dot{\theta}$ and the load torque, τ_L [226]. The rotor is assumed to be rigid and the magnetic field constant. This is given in Equation (4.38).

$$\ddot{\theta} = \frac{1}{J_m}\left(\tau - b\dot{\theta} - \tau_L\right) \tag{4.38}$$

where:

$\dot{\theta}$	Rotor velocity	[rad·s^{-1}]
J_m	Rotor inertia	[kg·m^2]
τ	Rotor torque	[N·m]
b	Viscous damping factor	[N·s·m^{-1}]
τ_L	Load torque	[N·m]

As the magnetic field is assumed to be constant, the motor torque is directly proportional to the armature current, i_m, such that:

$$\tau = K_t i_m \tag{4.39}$$

where:

K_t	Motor torque constant	[N·m·A^{-1}]

The armature current is a function of the circuit inductance, L_m, the circuit resistance, R_m, the applied voltage, V_{DC}, and the back emf, e. This is provided in Equation (4.40).

$$\dot{i}_m = \frac{1}{L_m}(-R_m i_m + V_{DC} - e) \tag{4.40}$$

where:

i_m	Armature current	[A]
L_m	Circuit inductance	[H]
R_m	Motor resistance	[Ω]
V_{DC}	Applied voltage	[V]
e	Back emf	[V]

Similarly, the back emf is proportional to the rotor speed, as in Equation (4.41).

$$e = K_e \dot{\theta} \tag{4.41}$$

where:

K_e Electromotive force constant [V·s·rad^{-1}]

4.4.2 Air Compressor

A scroll-type compressor is comprised of two meshing scroll blades of identical spiral geometry. One scroll blade is fixed and the other sits on a shaft capable of orbiting around a fixed path. The meshing blade geometry is presented in Figure 4-7. As the moving scroll orbits, air is forced through the device as the chamber volumes decrease. The compressor is driven by an electric motor.

A mathematical model for a scroll-type compressor is derived from a mathematical model of a scroll-type expander [227,228]. In contrast to scroll compressors, which are powered by rotational motion to produce pressurised air, scroll expanders work in reverse, powered by compressed air to produce rotational motion. Thus, the derivations of chamber geometry can be applied for compressors.

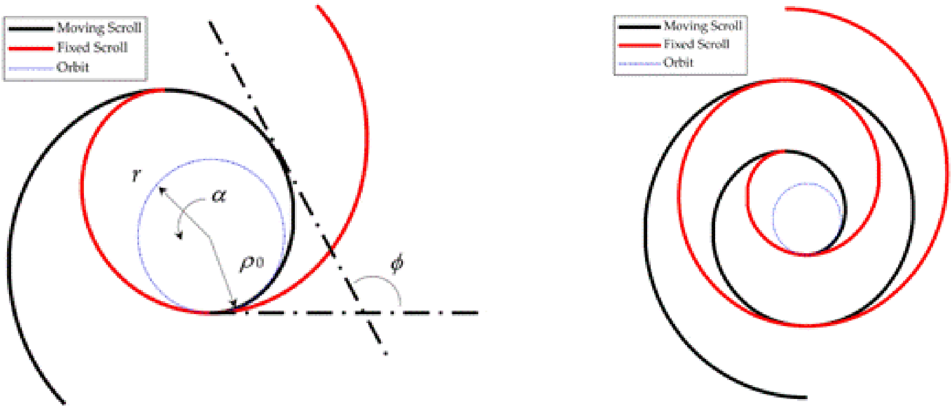

(a) **(b)**

Figure 4-7. (a) Geometry definition for the scroll compressor blades (b) Scroll-type compressor blade geometry

As in Figure 4-7, the moving scroll orbits on a fixed path and is enveloped by the fixed scroll. Air is compressed as in moves inwards from the inlet to the central outlet valve, which results in air being pumped through the device. The geometry of the moving scroll blade is determined by Equations (4.42) and (4.43).

$$x_m = (\rho_0 + k\phi)\sin\phi + k\cos\phi - k + r\sin\alpha \tag{4.42}$$

$$y_m = -(\rho_0 + k\phi)\cos\phi + k\sin\phi + \rho_0 - r\cos\alpha \tag{4.43}$$

where:

x_m	x-coordinate for moving-scroll geometry definition	[m]
y_m	y-coordinate for moving-scroll geometry definition	[m]
ρ_0	Initial radius of curvature	[m]
ϕ	Angle of rotation	[°]
k	Opening curvature value	[m]
r	Orbit radius	[m]
α	Orbit angle	[°]

The coordinates for the enveloping scroll blades can be similarly derived by Equations (4.44) and (4.45).

$$x_f = \left(\rho_0 + k(\phi + \pi)\right)\sin(\phi + \pi) + k\cos(\phi + \pi) - k + r\sin\phi \tag{4.44}$$

$$y_f = -\left(\rho_0 + k(\phi + \pi)\right)\cos(\phi + \pi) + k\sin(\phi + \pi) + \rho_0 - r\cos\phi \tag{4.45}$$

where:

x_f	x-coordinate for fixed-scroll geometry definition	[m]
y_f	y-coordinate for fixed-scroll geometry definition	[m]

Figure 4-8 demonstrates one full orbit of the moving scroll blade and the effect on the inlet, side and central chambers.

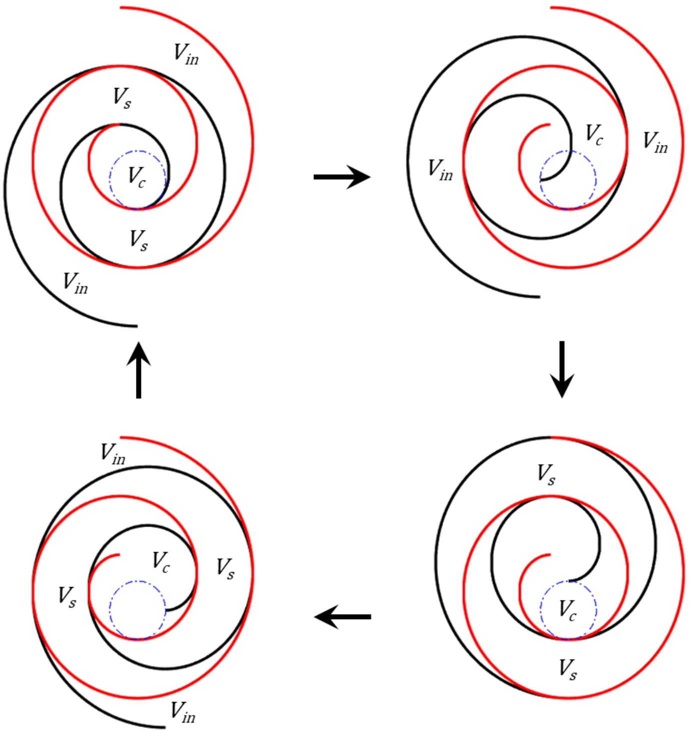

Figure 4-8. Compression cycle for scroll compressor orbit

The volume of the compressor's inlet chamber is calculated with Equation (4.46).

$$V_{in} = V_{total} - V_c - V_s \tag{4.46}$$

with:

V_{in}	Inlet chamber volume	[m^3]
V_{total}	Total scroll volume	[m^3]
V_c	Central chamber volume	[m^3]
V_s	Side chamber volume	[m^3]

The side chamber volume can be calculated using Equation (4.47).

$$V_s = z[\pi r^2 + 2\pi r(\rho_0 + k\alpha)] \tag{4.47}$$

where:

z	Scroll blade height	[m]

The volume of the central chamber can be calculated with:

$$V_c = z\Big[(kr - \pi k^2)\cos\alpha + (kr\rho_0\pi - r\rho_0)\sin\alpha + (kr\pi + 2k\rho_0\pi)\alpha + k^2\pi\alpha - kr$$
$$+\frac{1}{3}k^2\pi^3 - \frac{1}{2}kr\pi^2 + \rho_0 r\pi + \frac{1}{2}r^2\pi + {\rho_0}^2\pi\Big] \tag{4.48}$$

Calculating the volume of the respective chambers dynamically, allows for the determination of the pressure and temperature of the air in the respective chamber. For the model, perfect meshing is assumed so that no air leaks between alternate chambers. The pressure of the inlet chamber increases for the first phase of the orbit, such that the pressure decreases below ambient; this draws air into the inlet chamber. The pressure in the inlet chamber is related to the volume of the inlet chamber through Equation (4.49).

$$\dot{p}_{in} = \frac{1}{V_{in}}\left(\dot{m}_{in}RT_{in,t} - \dot{V}_{in}p_{in}\right) \tag{4.49}$$

where:

p_{in}	Inlet chamber pressure	[Pa]
$\dot{m}_{in}$	Inlet mass flowrate	[kg·s^{-1}]
$T_{in,t}$	Air inlet temperature	[K]
R	Universal gas constant	[J·kg^{-1}·K^{-1}]

The pressure in the side chamber can be calculated through Equation (4.50).

$$\dot{p}_s = \frac{1}{V_s}\left(m_sR\dot{T}_s - \dot{V}_sp_s\right) \tag{4.50}$$

where:

p_s	Side chamber pressure	[Pa]
m_s	Side chamber air mass	[kg]

and the pressure in the central outlet chamber can be calculated with Equation (4.51).

$$\dot{p}_c = \frac{1}{V_c}\left(m_cRT_c - \dot{V}_cp_c - \dot{m}_{out}RT_c\right) \tag{4.51}$$

where:

p_c	Central chamber air pressure	[Pa]
$\dot{m}_c$	Mass in central chamber	[kg·s^{-1}]
T_s	Side chamber air temperature	[K]
T_c	Central chamber air temperature	[K]
$\dot{m}_{out}$	Outlet mass flow of compressor	[kg·s^{-1}]

The masses of air in the respective chambers are determined through the ideal gas law. The temperatures of the air in the side and central chambers are given by Equations (4.53) and (4.54) respectively.

$$T_s = T_{in,t}\left(\frac{V_s|_{V_s=max}}{V_s}\right)^{\gamma-1} \tag{4.53}$$

$$T_c = T_s\left(\frac{V_c|_{V_c=max}}{V_c}\right)^{\gamma-1} \tag{4.54}$$

with:

T_s	Side chamber air temperature	[K]
γ	Ratio of specific heats	[-]
T_c	Central chamber air temperature	[K]

In Equations (4.53) and (4.54), the subscript '*max*' denotes the greatest value of the volume of the chamber that is achieved as the moving blade orbits around the fixed blade. The derivative of the temperature can be taken to satisfy the pressure calculation equations. The mass flowrate is determined through orifice theory [229] and given by Equation (4.55).

$$\dot{m}_{out} = \frac{C_d C_0 A_{out} p_c f(p_r)}{\sqrt{T_c}} \tag{4.55}$$

where:

C_d	Discharge coefficient	[-]
C_0	Discharge coefficient	[-]

A_{out}	Outlet area	[m^2]
p_c	Central chamber pressure	[Pa]
T_c	Central chamber temperature	[K]
$f(p_r)$	Flow function	[-]

The flow function, $f(p_r)$, is determined by Equation (4.56).

$$f(p_r) = \begin{cases} 1 & p_r \leq C_r \\ C_k[{p_r}^{2/\gamma} - {p_r}^{(\gamma+1)/\gamma}]^{1/2}, & p_r \leq 1 \end{cases} \tag{4.56}$$

and:

p_t	Tank pressure	[Pa]
p_r	Upstream-downstream pressure ratio[7]	[-]
C_r	Discharge coefficient	[-]
C_k	Discharge coefficient	[-]

The discharge coefficients, along with other modelling parameters are listed in Appendix D. The resistive torque generated by the compressor is given in Equation (4.57) [230].

$$\tau_L = \sum zr[2\rho_0 + 2k\alpha + (4j+1)k\pi]\Delta p \tag{4.57}$$

where:

j	Counter for number of compressing chambers	[-]
Δp	Pressure difference between compression chambers	[Pa]

The torque calculated by Equation (4.57) is used as the load torque in Equation (4.38) for the DC motor operation. The counter, j, is either 0 or 1 depending on which stage of the scroll orbit is currently proceeding.

---

[7] In this case, the upstream-downstream pressure ratio is the ratio between the storage tank pressure and the pressure of the air in the central outlet chamber.

4.4.3 Compressed Air Storage

A compressed air tank model can be derived from the energy conservation equations. Isentropic storage can be assumed with the pressure changes arising from mass flow in or out of the vessel or a change in temperature of the air [231]. The density of the air present in the air tank can be calculated through Equation (4.58).

$$\dot{\rho}_t = \frac{\dot{m}_i + \dot{m}_o}{V_t} \tag{4.58}$$

with:

ρ_t	Tank air density	[kg·m^{-3}]
$\dot{m}_i$	Input mass flow	[kg·s^{-1}]
$\dot{m}_o$	Output mass flow	[kg·s^{-1}]
V_t	Tank volume	[m^3]

The variable $\dot{m}_i$ in the compressed air tank model corresponds to the variable $\dot{m}_{out}$ in the scroll compressor model. The output flow of the tank corresponds to discharging air to blow across the panel surface. The temperature of the air in the tank can be calculated with Equation (4.59):

$$\dot{T}_t = \frac{1}{V_t \rho_t c_v}\left(\dot{m}_i\left(c_{p,air}(T_{in} - T_t) + RT_t\right) + \dot{m}_o RT_t\right) \tag{4.59}$$

where:

T_t	Tank air temperature	[K]
c_v	Isochoric specific heat	[J·kg^{-1}·K^{-1}]
$c_{p,air}$	Specific heat of air in tank	[J·kg^{-1}·K^{-1}]
T_{in}	Inlet air temperature	[K]

The pressure of the air in the air storage can be determined with Equation (4.60).

$$p_t = \rho_t R T_t \tag{4.60}$$

where:

p_t	Tank air pressure	[Pa]

4.4.3.1 *Air Discharge and Velocity*

The discharging air velocity can be determined through the continuity of compressible gas at steady flow conditions [232], represented by Figure 4-9 and Equation (4.61).

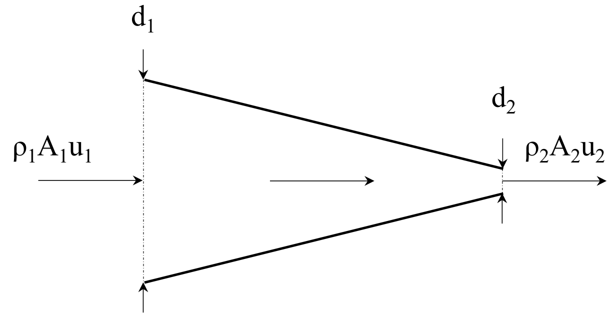

Figure 4-9. Continuity for compressible flow at steady flow conditions

$$\rho_1 u_1 A_1 = \rho_2 u_2 A_2 \tag{4.61}$$

where:

$$Q = uA \tag{4.62}$$

and:

$u_{1,2}$	Air velocity	[ms^{-1}]
$\rho_{1,2}$	Air density	[$kg{\cdot}m^{-3}$]
$A_{1,2}$	Chanel cross sectional area	[m^2]
Q	Volumetric flowrate	[$m^3{\cdot}s^{-1}$]

and subscripts '*1*' and '*2*' denoting the pipe and the nozzle outlet respectively. The pressure and flowrate in the pipe allows the determination of the velocity of the air at the nozzle, assuming atmospheric pressure at the outlet.

$$u_2 = \frac{\rho_1}{\rho_2} \frac{Q_1}{A_2} \tag{4.63}$$

The average air velocity across the panel can then be approximated through the ratio of the panel width nozzle outlet width through expansion, this is given in Equation (4.64).

$$V_{air} = 0.5 \times \frac{d_2}{d_p} u_2 \tag{4.64}$$

where:

V_{air}	Air velocity	[m·s^{-1}]
d_2	Nozzle width	[m]
d_p	Panel width	[m]
u_2	Nozzle velocity	[m·s^{-1}]

4.5 Full System Model

Figure 4-10 demonstrates the interaction of the described subsystem components into a full mathematical model for representing the PV-CAES system for panel cleaning and cooling. The model is implemented in MATLAB/Simulink.

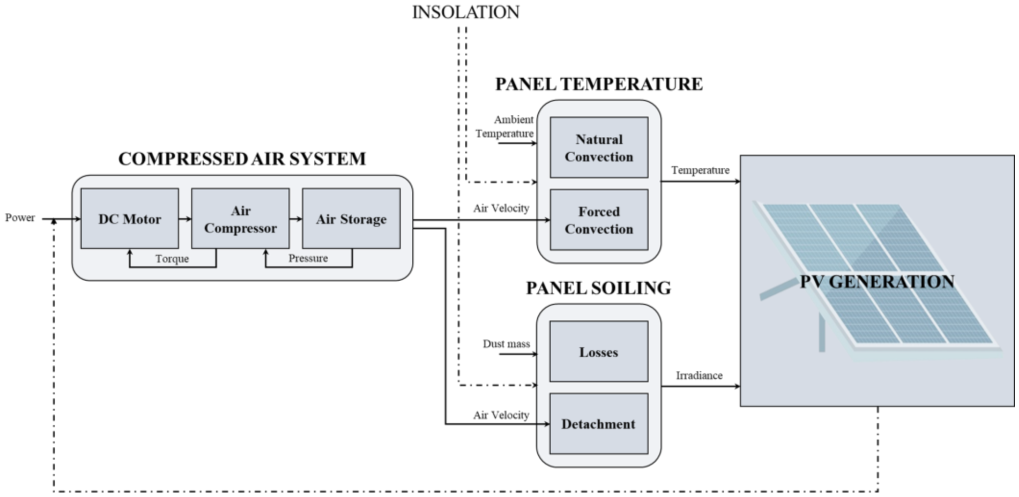

Figure 4-10. Interaction of mathematical model components in the full system model

The PV generation is determined from input of the panel temperature and the irradiance. The panel temperature is determined from the input insolation and can be dynamically switched between no air release and air release to determine natural or forced convective mechanisms. The panel input irradiance value is also dependent on the level of panel soiling, affected by the mass of dust present on the panel surface and whether compressed air is being released across the panels surface and the particle detachment criteria have been met. The compressed air system dictates the air velocity of the released air over the panel surface and can be operated dynamically. The compressed air system is additionally used for the overall energy analysis regarding the required energy to produce the compressed air and assessment of potential energy benefit from implementing the system.

4.6 Control of System Charging Process

This section concerns the control of the charging process of the proposed PV-CAES system for panel cleaning and cooling and demonstrates the mathematical model functionality. The control is developed for the particular structure of the proposed system described in Figure 4-11 and the mathematical model elements derived in this chapter. These are, DC-DC power conversion from PV generation, a DC motor and small-scale compressed air tank, with a scroll-type air compressor. System discharging, concerning the temperature, soiling and detachment mechanisms are not considered here as only the charging process is concern; these are validated and studied in Chapter 6.

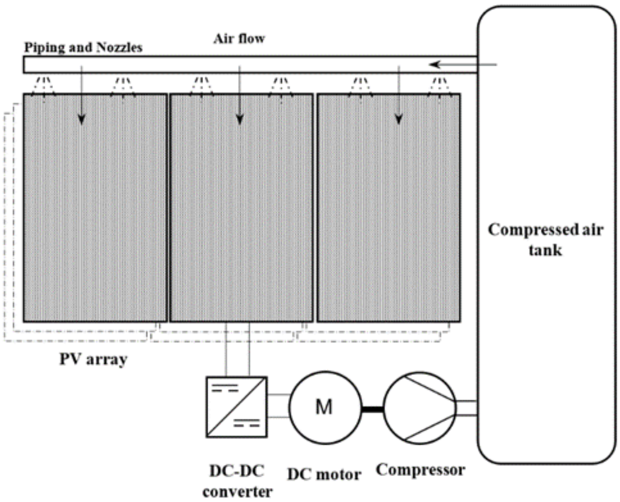

Figure 4-11. System modelled for the charging process control development

For the compressed air charging process and its control, the mathematical model of the proposed system introduced earlier in this chapter forms the basis of the model. This is a highly nonlinear system because of air compressibility and tank pressure changes as the charging process progresses. A control strategy for charging a compressed air tank from variable PV voltage source is developed and analysed to ensure the whole charging process operating smoothly.

Coupling the DC power generation from the PV panel to a boost converter is necessary to step up the low voltage PV output to suitable higher voltage. Additionally, the switching of the boost converter can be controlled to ensure a constant voltage supply to the motor for the variable voltage output from the PV generation, as this is dependent on the instantaneous availability of the solar resource. A functional requirement of this proposed system implementation is that there must be a minimum installed capacity of PV available to power the compressor.

4.6.1 Control Study Model Derivation

A further derivation of the charging process mathematical model must be established for the consideration of the charging process control. The introduction of the boost converter model modifies the operating principles of the previously described mechanisms. The modified charging process diagram is presented in Figure 4-12, which shows the equivalent circuits of the solar PV, converter and motor and their link to the compressor and air tank. From the equivalent circuit a mathematical model can be reformulated. PV generation equations remain the same as indicated in Section 4.1, but the DC motor mathematical model is modified based on the introduction of the boost-converter.

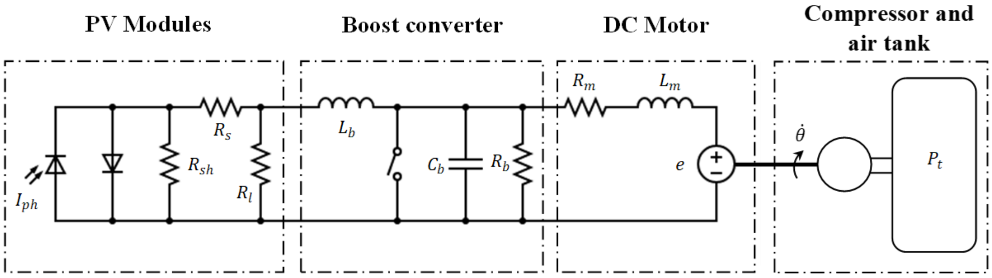

Figure 4-12. Circuit diagram representation of the proposed system used for the derivation of the mathematical model

The PV equivalent circuit, or any number of PV circuits connected in parallel to produce a large amount of current, can be coupled with a DC-DC boost converter to step up and control the output PV voltage. The converter can be modelled as a switching circuit with a predetermined inductance, L_b, capacitance, C_b, and resistance, R_b. The duty cycle, ρ, determines the switching and controls the output voltage. The boost converter output is connected to supply the DC motor. This can be represented by a resistance and inductance in series with a back emf generated by the motor, from the independent DC motor model examined in Section 4.4.1 and described by Equation (4.38) to Equation (4.41).

Voltage input to the boost converter will be variable owing to panel output voltage being dependent on the instantaneous solar radiation. For this control study, it is assumed that the array is sufficiently large that any current quantity can be drawn and the boost converter can regulate against the input voltage profile only. Following the circuit representation in Figure 4-12, the established DC motor model and applying Kirchoff's laws, the following dynamic model of the boost converter and DC motor can therefore be derived; this are Equations (4.65) to (4.68) [233].

$$\frac{di}{dt} = \frac{1}{L_b}\left(V_{DC} - [1-\rho]V_\mathrm{o}\right) \tag{4.65}$$

$$\frac{dV_\mathrm{o}}{dt} = \frac{1}{C_b}\left([1-\rho]i - \frac{1}{R_m}V_\mathrm{o} - i_m\right) \tag{4.66}$$

$$\frac{di_m}{dt} = \frac{1}{L_m}\left(V_o - R_m i_m - K_e\dot{\theta}\right) \tag{4.67}$$

$$\frac{d\dot{\theta}}{dt} = \frac{1}{J_m}\left(K_t i_m - b\dot{\theta} - \tau_L\right) \tag{4.68}$$

The parameters listed here are the same as described earlier in this chapter, but are listed here again for convenience along with the additional parameters introduced by the boost-converter:

i	Panel output current	[A]
L_b	Boost-converter inductance	[H]
V_{DC}	Panel output voltage	[V]
ρ	Duty cycle	[-]
V_O	Boost-converter output voltage	[V]
C_b	Boost-converter capacitance	[F]
R_m	Motor resistance	[Ω]
i_m	Motor armature current	[A]
L_m	Motor inductance	[H]
K_e	Electromotive force constant	[V·s·rad^{-1}]

$\dot{\theta}$	Motor velocity	[rad·s^{-1}]
J_m	Motor inertia	[kg·m^{2}]
K_t	Motor torque constant	[N·m·A^{-1}]
b	Viscous damping factor	[N·s·m^{-1}]
τ_L	Load torque	[N·m]

The converter duty cycle, ρ, ranges between 0 – 1 and corresponds to the proportion of time that the switch in the circuit is connected. For the control of the charging process the scroll-type air compressor and air store model are as described in Sections 4.4.2.

4.6.2 Control Implementation

Solar radiation data at given locations can vary greatly throughout one day but is not typically subject to rapid step changes over short periods. It has been shown that maximum changes in measured radiation does not exceed ±50 Wm^{-2}s^{-1} over maximum changes of ±500 Wm^{-2} [234]. Hence typical changes in input radiation occur over a period between 5 and 10 seconds. These correspond to a *‘positive front’* where clouds can clear causing a rise in radiation and a *‘negative front’* whereby clouds obscure the sun cause a quick drop in input radiation. These scenarios will correspond to a change in voltage produced from the PV modules. Additionally for average clear or overcast conditions, there is some natural variation in measured radiation and this typical variation occurs from random shading and is between ±25 Wm^{-2} and ±75 Wm^{-2} for clear and overcast days respectively [234].

To be able to respond to the changes in PV voltage arising from the aforementioned scenarios, control of the converter must be established. The controller needs to respond well in both standard operation, where there is only a slight variation in input solar values and also in the extreme cases, where there is the maximum possible increase, the ‘*positive front*’, and decrease, the ‘*negative front*’ in input radiation. In one case, it is desirable to maintain a constant voltage supply to the motor to have relatively constant power output. Another case, it is required the motor to deliver the required load torque at the speed which is optimal to the compressor. Here, the constant voltage maintenance control is reported. A PID control is implemented to regulate the duty cycle of the converter. PID control was chosen as the primary control strategy because of its simple mechanism, effective nature and robust functionality across a wide range of operating conditions [235]. The voltage across the motor is measured and used as feedback in the control to determine the duty cycle in accordance with Equation (4.65) and Equation (4.66). Parameters for monocrystalline panels rated at 100W were measured and implemented as simulation parameters with multiple parallel connection of panels. Additionally, parameters for a 3-kW motor and compressor were adopted for use in the simulation. The choice of electronic component parameter values were sized appropriately to the system, with a small-scale 200 L air used as the air store. The parameters used for simulation are contained in Appendix D. The derived mathematical model is implemented in MATLAB and Simulink. The block diagram in Figure 4-13 indicates the interactions between the relative components with the corresponding control signal.

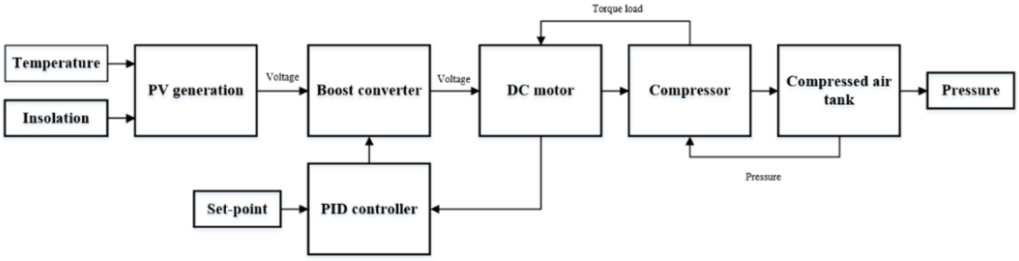

Figure 4-13. Block diagram demonstrating connections of mathematical model elements for the charging process control

For the case of the system response to standard solar variation on a clear day the following scenario was adopted. A radiation value of 750 Wm^{-2} was used as input with random variation of up to ±75 Wm^{-2}; this corresponds to the random fluctuation in solar input values for an overcast day across a short period of 120 seconds. The voltage was measured at the input and output of the boost converter to assess the control performance. The set-point voltage to be supplied to the motor was 110 V, the simulation results can be seen in Figure 4-14.

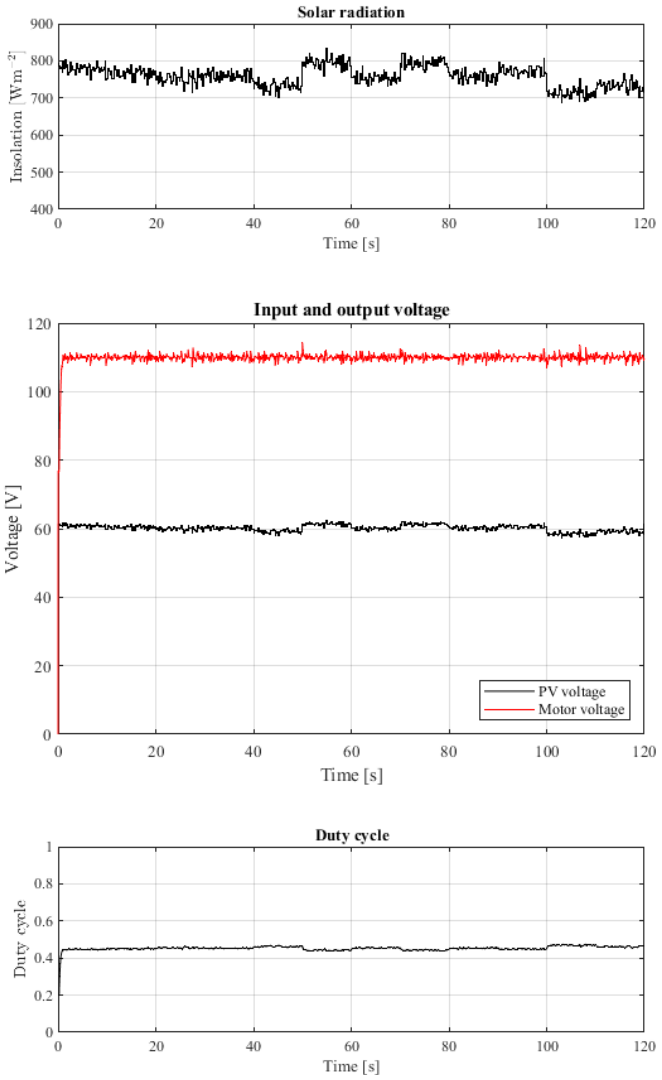

Figure 4-14. Solar radiation variation and corresponding change in input and output voltage

Observing Figure 4-14, the PID control is effective at maintaining a constant voltage across the motor when subjected to the small variations arising during standard PV operation. The input voltage to the converter can be seen to vary but the set-point of 110V is achieved and maintained at a steady value with small signal spikes of maximum 3 V for less than 0.1s. The adjustment in duty cycle can also be observed as a response to the changing input voltage. The performance of the motor during this time period can be observed in Figure 4-15.

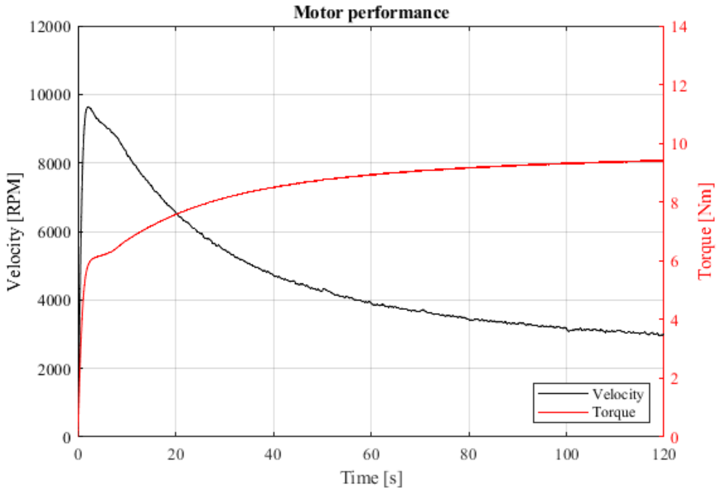

Figure 4-15. Motor velocity and torque

Fig. 4-15 demonstrates functionality of the motor and compressor modelling during the overcast scenario. The speed of the motor decreases during the period and the required torque increases. This is because the upstream pressure in the air tank increases, which induces a load torque increase. As the motor is powered by a constant voltage source, the load torque increase drives the motor speed decrease. The accumulation of air in the tank during this period can be observed in Figure 4-16.

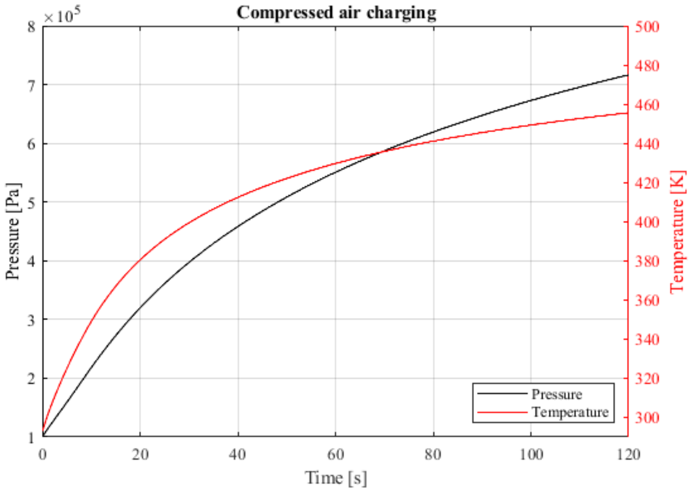

Figure 4-16. Compressed air tank pressure and temperature throughout charging period

Both the pressure and the temperature of the tank increase during the 120 second simulation period. If simulated for a longer duration the temperature and pressure will reach an equilibrium after the point at which the motor delivers the required torque with the reduced speed to compensate the pressure gradient from the compressor to the air tank.

The system is also subjected to a ‘*positive front*’ scenario which represents the extreme case for increase to input radiation to the system. This is given in Figure 4-17.

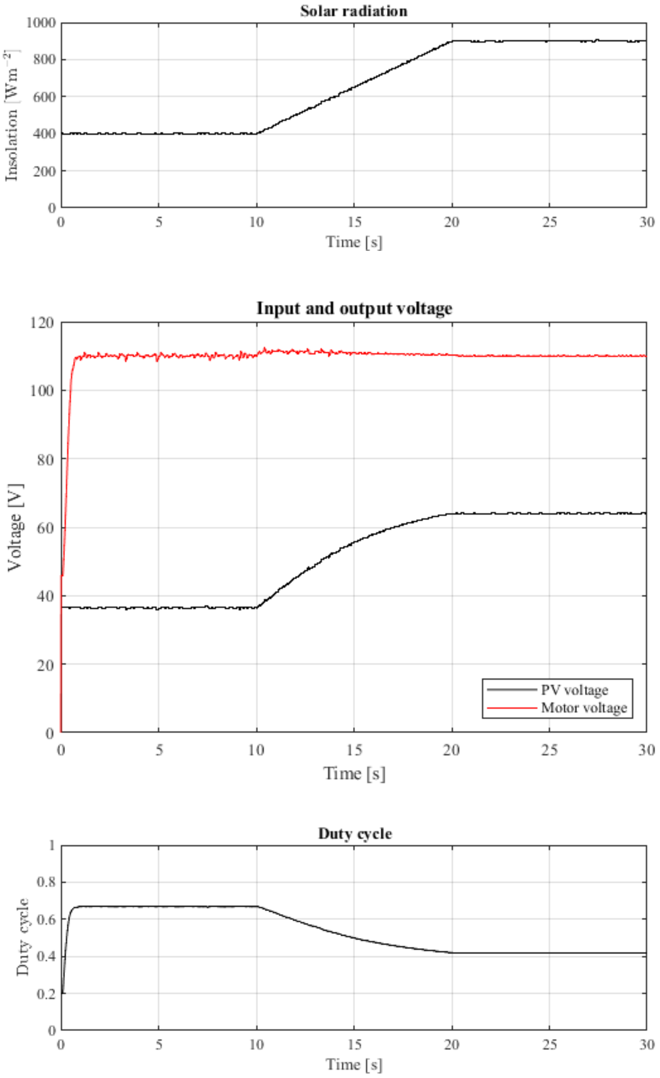

Figure 4-17. PV voltage and motor voltage in response to '*positive front*' scenario

Observing Fig. 4-17, the radiation value increases from 450 Wm^{-2} to 950 Wm^{-2} over a period of 10s. Additional random variation also added to the increase to emulate true measured solar data. This increase in input radiation corresponds to an increase from 37 V to 64 V at the output of the PV. A slight increase in motor voltage can be observed which increases from the set-point of 110 V to 112 V but the controller adjusts the duty cycle and returns the output to 110 V within a 5 second settling time. The duty cycle response can be observed as a result of the input voltage change. This level of disturbance and settling time is adequate for the situation of charging the air tank. Additionally, the system response to a ‘*negative front*’ can be seen in Figure 4-18.

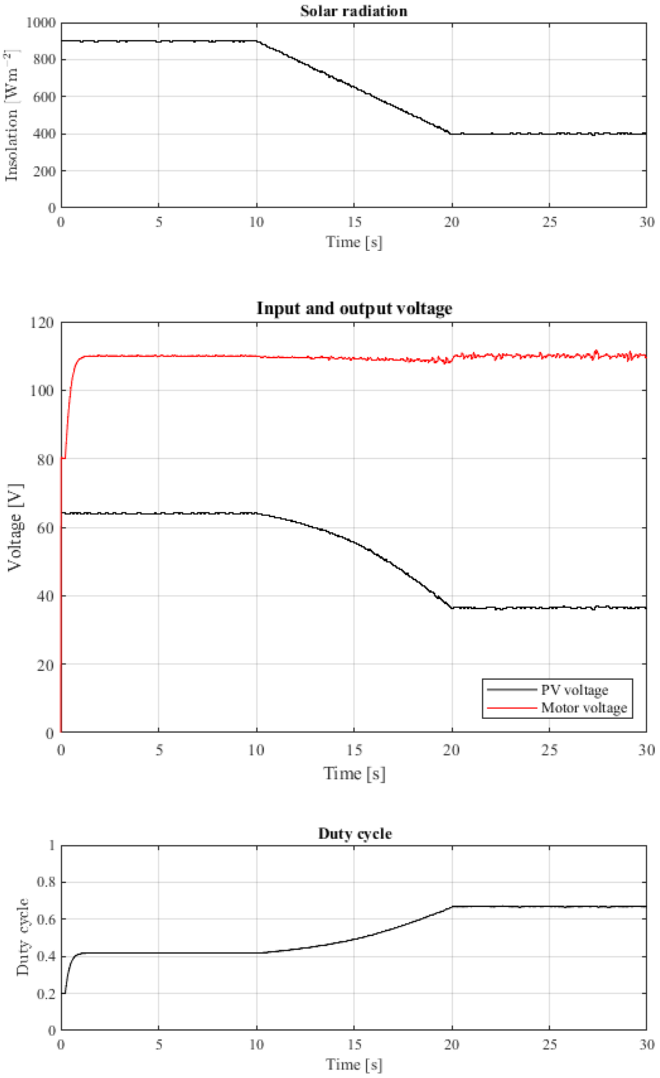

Figure 4-18. PV voltage and motor voltage in response to a '*negative front*' scenario

As with the '*positive front*' case random variation has been added to the declining insolation value. The input insolation drops from 950 Wm^{-2} to 450 Wm^{-2} over 10 seconds. The change in input condition corresponds to a drop in voltage from 64 V to 37 V from the PV output. A 2 V drop in motor voltage is observed and the controller restores the voltage to the set-point within 3 seconds. As with the overcast scenario and '*positive front*' case the controller performance is satisfactory. The PID control has shown it is effective in the typical use for random fluctuations in solar data and has been shown to be effective at maintaining a constant output voltage at the extreme conditions. The mathematical model of the charging process of the proposed PV-CAES has also been demonstrated to function suitably.

4.7 Summary

A dynamic mathematical model has been derived for the proposed integrated PV-CAES system for panel cleaning and cooling. The key components and mechanisms for the small-scale system orientation have been described and a mathematical model for each has been given with the necessary assumptions and simplifications discussed. These are: PV panel generation, PV panel temperature subject to normal heating effects and cooling from the CAES system, particle surface adhesion and detachment subject to compressed air flow, soiling losses to PV, a DC motor, scroll-type air compressor and compressed air storage. Together, these systems are combined to create a model that can be used to assess the potential benefit to PV power generation from cleaning and cooling from high pressure air discharging.

Further the mathematical model of the charging system of the proposed system has been derived, comprising of PV generation, a DC-DC boost converter, DC motor, compressor and air vessel. PID control has been implemented such that a constant voltage can be applied to the motor given a variable voltage input from the PV generation. The control has shown to be effective for charging the compressed air tank from a PV source for a standard use case of variable radiation from an overcast day as well as both the extreme increase and decrease cases of solar radiation. The closed-loop PID control is shown to be effective at maintaining a constant motor supply voltage in all these situations. The functionality of the charging process modelling has additionally shown to be effective.

The derived system model will be used to guide selection of test rig components and the whole system evaluation. This chapter only presents the simulation study for compressed air charging process. The discharging process modelling, testing and validation will be presented in the subsequent chapters.

Chapter 5 – PV-CAES System Test Rig Design and Implementation

An experimental test rig is necessary to assess the feasibility of using pressurised air to clean and cool solar PV panels and to validate the dynamic mathematical model derived in Chapter 4. The required functions that the test rig must perform are first given and then the individual elements of the test rig are discussed, with technical parameters and design rationale highlighted. The hardware, sensors, instrumentation and control system, including MPPT, are presented and the final test rig capabilities are discussed.

5.1 Test Rig Requirements

The fundamental requirements of the test rig are listed in Table 5-1. The design requirements were determined from consideration of the necessary features essential for assessing the capability of using compressed air to clean and cool solar PV panels. The test rig should emulate the components of the proposed system introduced in Chapter 3 and be capable of measuring and recording experimental data to validate the derived mathematical model presented in Chapter 4.

The test rig is designed around a PV panel. The constructed rig must provide a source of light to a PV panel, that the panel can convert into electrical power that can be measured. The rig must be capable of heating the panel, to emulate the temperature effects experienced by operational PV panels and therefore the power generation reduction that the panel experiences can be measured. Thus, the test rig must have capability of measuring the operating temperature of the panel.

Furthermore, the test rig must be able to emulate soiling effects on solar PV generation. For this, test-dust must be sourced that possesses similar characteristics to dust responsible for soiling losses in operational PV plants. The dust can be deposited on the panel surface and an output power reduction can be measured.

A compressed air system is to be established such that air can be stored and subsequently directed to the panel surface through a network of pipes and nozzles, blowing over the surface of the panel. The flowrates and pressures of the airflow must be measurable and controllable. Nozzle implementation should be modular such that nozzle number and orientation can be varied and can be used to assess the effectiveness of different nozzles designs.

An electronic load is required to vary the operating point of the PV panel and MPPT is to be implemented such that the panel can always be operating at the optimum generation point, given the variable temperature and soiling rate that the panel will experience. This will give an accurate indication of the benefit to the generation from the cleaning and cooling system than if the panel was subject to a fixed resistive load.

The test rig should accommodate PV panels of a commercial size, that are used in PV installations, and not simply accommodate small-scale solar modules; observing the effect of air cleaning and cooling on the commercial scale panels in the test rig will provide a better representation of a comparable system that could installed in a regular commercial setting. The test rig should also be able to accommodate a range of panels so that differently dimensioned PV panels can be assessed and the rig should not be limited to accommodating a single PV panel.

Additionally, the test rig should be inclinable as most commercially implemented panels possess a positive angle of inclination. The angle of inclination is expected to affect the particle detachment and cleaning criteria as gravity contributes to detachment and increases with panel angle.

The whole system should be enclosed such that when high velocity air is blowing over the surface of the panel and dust is being removed, the removed dust is self-contained and does not escape the system. Furthermore, a barrier will exist between the high velocity air within the test rig and the external environment. The enclosure will also create an increased internal temperature within the test rig system that can emulate ambient temperature of hot environments where PV installations may be present.

Finally, the measured data from the implemented sensors and control of the electronic load and pneumatic components should be coordinated from a single interface that can also be used to record and export obtained data.

Table 5-1. Design requirements of PV-CAES test rig

Element	Requirements
Light source	• Provide lighting to power a PV panel that can generate electrical power from this light source
Heating	• Heat the panel to emulate temperature effects on PV power output
Soiling	• Test-dust, to deposit on the panel surface to emulate soiling effects on PV power output

	• The acquired test-dust should be representative of dust that induces soiling losses in commercial systems
Structure	• Accommodate commercial scale PV panels • Adaptable to a range of PV panel sizes • Panel should be inclinable
Compressed air system	• Direct high-pressure air to the surface of the PV panel • Possess a modular system of nozzles that can be altered and reconfigured easily
Enclosure	• Isolate the system from the external environment, preventing dust from escaping and containing high velocity air • Increase the internal ambient temperature of the test rig
Measurement and control platform	• Record the power output of the PV panel • Record the temperature of the PV panel and ambient • Record the pressure and flowrates of compressed air system • Regulate the airflow being delivered to the panels • Enact MPPT for maximal power extraction

5.2 Final Test Rig

5.2.1 Test Rig Structure

The finalised structure of the constructed test rig is demonstrated in Figure 5-1. A panel bed of 1.95m by 1.37m lies parallel to a lighting panel of the same dimensions, elevated 0.4 m above. The panel bed possesses a test area of 2.67 m^2, which is sufficient to accommodate most commercial PV panels. The entire test platform is inclinable up to 45° as per the design requirements, indicated in Figure 5-2. When inclined, the lighting panel remains parallel to the panel bed and the perceived level of solar irradiance on the panel bed remains constant. The structural frame of the test rig is comprised of extruded aluminium.

Figure 5-1. Uninclined PV-CAES test rig viewed from the side

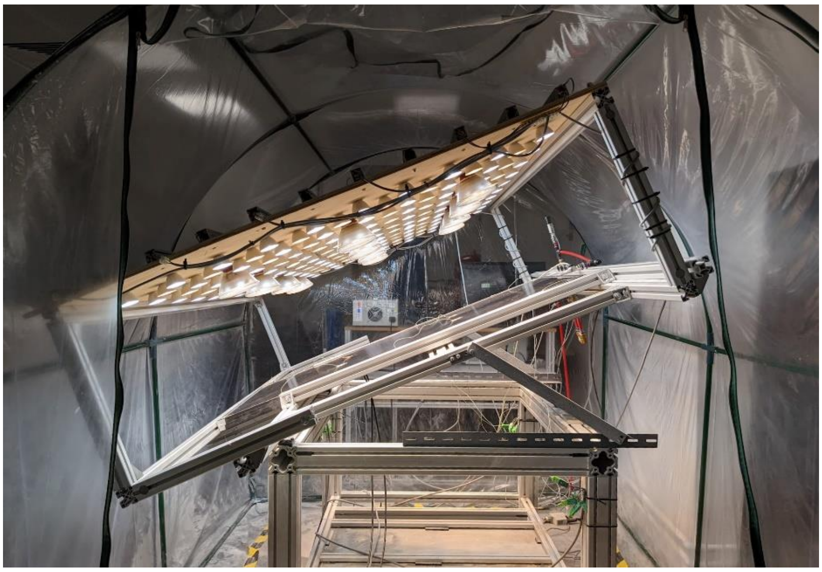

Figure 5-2. Inclined PV-CAES test rig viewed from the side

Lengths of aluminium profile hold the PV panel in the panel bed, with a bar running across the span of the rig at the top and bottom with perpendicular bars that can be moved into position to secure the PV panel from the side, this is indicated in Figure 5-3. Because the securing struts run around the perimeter of the PV panel holding it in place, they can be used for the mounting of the nozzle mechanism.

Figure 5-3. Highlight of panel bed and securing struts in the test rig

5.2.2 Light Source

In the test rig, a lighting panel hosts an array of lamps that act as the source of energy for the PV panel. LED bulbs were chosen as the light source to be implemented within the array because of their relatively high energy conversion efficiency, compact and robust nature, which is desirable for repetitive testing. Two '*colour*' LED lamps, 2700 K and 4000 K, were mounted in the light panel, to provide a broader spectrum of wavelengths to the PV panel under testing. The array of lights is comprised of two grids of LED bulbs offset by half of the length between two bulbs in the grid. The length between bulbs of the same colour is 0.125m vertically and 0.173m horizontally. The interspersed bulbs were implemented to create homogeneity in the light intensity experienced by the PV bed by creating overlap in the light projection between individual bulbs. In total 100 6.5 W, 2700K and 81 7 W, 4000 K bulbs were installed[8]. The viewing angle of the 2700K LEDS was 110° and the viewing angle of the 4000K LEDs was 36°. A transverse view of the LED lamp orientation is given in Figure 5-4.

---

[8] The specific LED bulbs used along with the list of all components used in the test rig is contained within Appendix C.

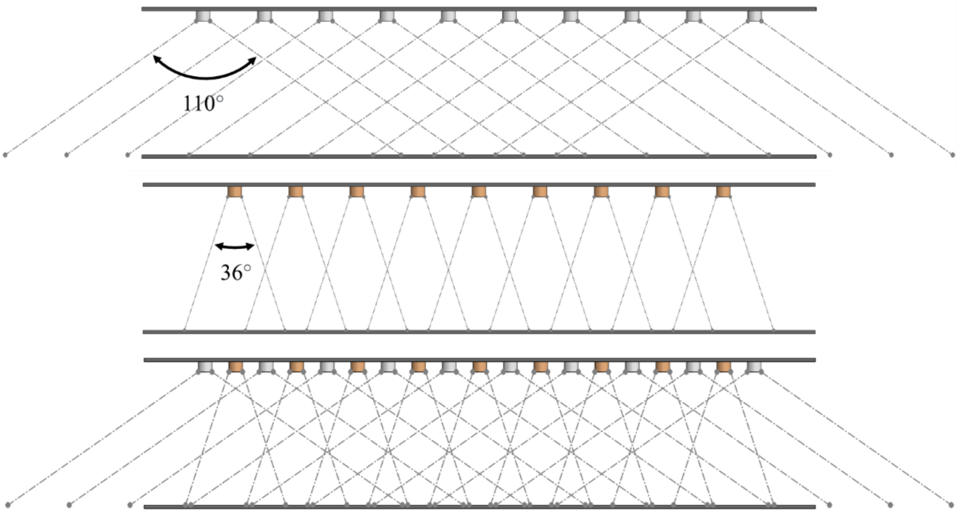

Figure 5-4. Viewing angles of bulbs implemented in light panel

The constructed light source resulted in an average measured irradiance value on the panel bed of 129.3 Wm^{-2}. The achieved irradiance value using LED bulbs as the light source is relatively low when compared to standard conditions for characterising solar PV modules (1000 Wm^{-2}). Furthermore, under this level of irradiance, tested panels were not reaching temperatures representative of the conditions that panels are subject to hot arid environments and therefore were not able to assess the benefit of cooling the PV panels with compressed air. Because of this, it was determined that the method for heating the panels would be through high-power incandescent heat lamps. This would fulfil two functions within the test rig: Firstly, they would provide additional radiation to the panel surface, increasing the average irradiance value perceived by the panel bed. Secondly, they would heat panels to higher temperatures, providing a better representation of high insolation regions, and therefore the cooling effect of compressed air could be more robustly tested.

To fit the incandescent heat lamps to the constructed light panel, 12 of the 4000 K LED bulbs were removed and replaced with 12 175 W incandescent heat lamps. These spaced evenly across the surface of the light panel. After this modification the final arrangement of the light sources on the light panel is given in Figure 5-5.

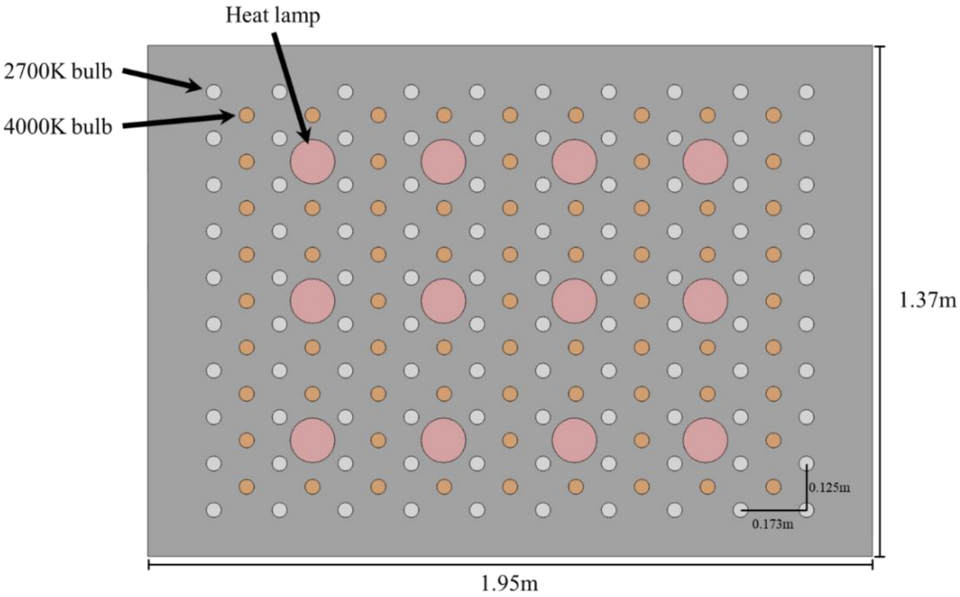

Figure 5-5. Layout of lamps implemented in light panel

The installed light panel with the combination of LED and incandescent heat lamps can be seen in Figure 5-6.

Figure 5-6. Light panel in the test rig

The installation of the heat lamps increased the total average irradiance value measured from the panel bed to 547 Wm^{-2}. The individual lamp types are wired independently so can be switched on in combination. Therefore, a range of insolation values can be emulated between 0 to 547 Wm^{-2}, the maximum achieved when all lamps are switched on. Table 5-2 demonstrates the range of irradiance values that can be achieved by the test rig through the switching of light sources.

Table 5-2. Parameters of light sources in test rig

Light source	**Average irradiance value measured on panel bed [Wm^{-2}]**
4000 K lamps	53.9
2700 K lamps	62.9
4000 K lamps + 2700 K lamps	119.1[9]
IR heat lamps	411.3
4000 K + IR heat lamps	448.4
2700 K + IR heat lamps	481.6
4000 K lamps + 2700 K lamps + IR heat lamps	547.4

5.2.3 Compressed Air System

High velocity air blowing over the panel surface is the investigated mechanism for cleaning and cooling PV panels in the system concept and test rig. The research laboratory in which the test rig is situated is fitted with a mains air-line that delivers air at 7 bar gauge. The compressed air network feeds a low-pressure 200 L air tank. A booster compressor is connected to the low-pressure air tank and increases the pressure up to 20 bar, connected to a larger high-pressure 340 L tank. The air is filtered and lubricated before supplying the booster compressor. Both tanks can act as the air reservoir for the test rig. The compressed air system is presented in Figure 5-7.

The tanks can be charged then disconnected from the mains supply such that when the valve to the test rig is opened, the pressure difference between the tank and the ambient pressure causes air to be expelled through the system. A manual pneumatic regulator is installed between air tanks nozzle system for safety and an electronic, variable pressure regulator is installed and controlled from the measurement and control platform. Air is delivered through pneumatic tubing and connected through push-fit connectors.

---

[9] The combined irradiance value of the LED bulbs has reduced from the initial 129.3 Wm^{-2} because of the removal of 12 of the 2700 K LED lamps to be replaced with the IR heat-lamps.

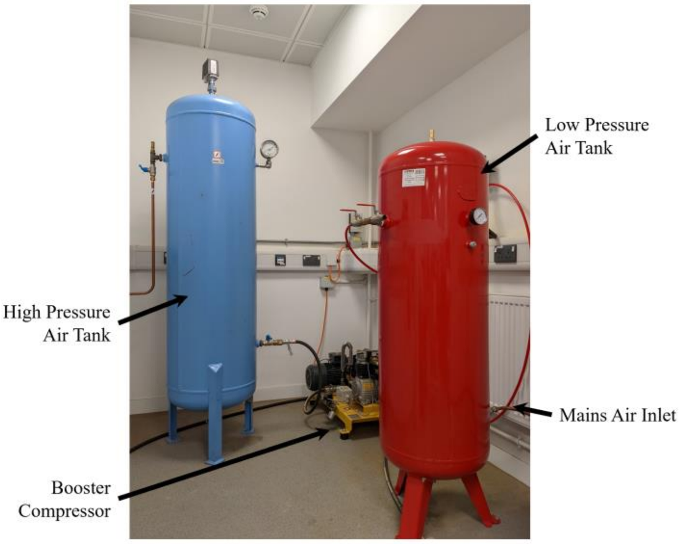

Figure 5-7. Compressed air system used in test rig

5.2.3.1 Nozzle Arrangement

Owing to the established test rig structure as described in Section 5.2.1, nozzles can be fitted around the perimeter of the test rig on the securing struts. The design allows for the investigation of the effectiveness of several nozzle arrangements and designs. Examples of the mounting of nozzles in the test rig, a single installed nozzle and a dual arrangement of nozzle, are given in Figure 5-8 and Figure 5-9 respectively. Nozzles are lain flat, parallel to the surface of the panel as this will provide the greatest perpendicular force to dust adhered to the panel surface. As the test rig is inclined, the relative angle between the nozzles and the panel surface remains constant. Wide fan nozzles were the implemented nozzle type as they generate a thin air profile vertically and wide angle horizontally. This creates a broad cleaning and cooling area across the panel surface. The nozzles were sourced from Silvent UK Ltd., a UK manufacturer of air and liquid nozzles.

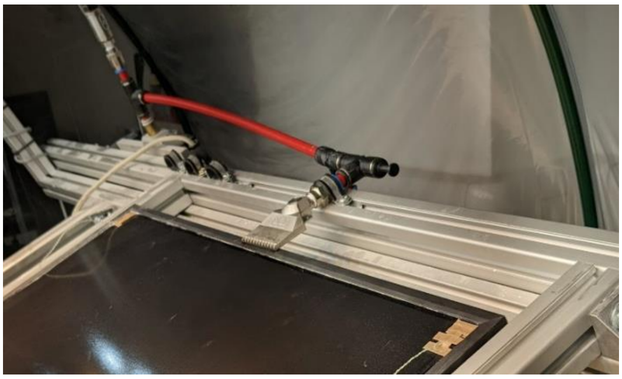

Figure 5-8. Single nozzle mounted in test rig

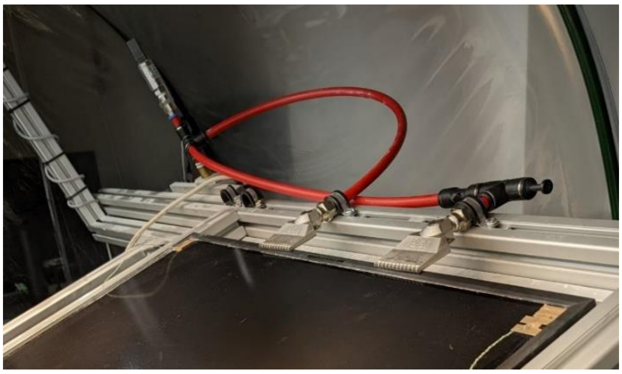

Figure 5-9. Two nozzles mounted in test rig

5.2.4 Sensors, Electronics, Data-acquisition Platform and Control

Several variables need to be measured and controlled in real-time during testing of the cleaning and cooling mechanisms. The required measurements can be broken down into electrical, pneumatic and thermal measurements. The necessary measurements that the test rig must record and the sensors used for monitoring these are given in Table 5-3.

Table 5-3. Required measurement and implemented sensor type

Category	Measurement	Sensor
Electrical	PV panel voltage	Integrated Digital Multimeter
	PV panel current	Integrated Digital Multimeter
Pneumatic	Tank air pressure	Pressure Transducer
	Pipeline air pressure	Pressure Transducer
	Nozzle pressure	Pressure Transducer
	Flowrate	Volumetric flowrate meter

Thermal	Panel temperature	Thermocouple Array
	Ambient temperature	Thermocouple

The test rig is monitored and controlled through a National Instruments PXI embedded controller and ancillary modules. The power from the PV panel is connected to an electronic DC load with the voltage and current measured through the NI integrated Digital Multimeter Module (DMM) connected to the PXI system. LABIEW was used for the processing of the acquired signals and a user-interface (UI) front panel was designed to interact with the components.

To measure the temperature of the PV modules, thermocouples are affixed to the PV panel. A total of 16 thermocouples are used to measure panel temperature, with 8 attached to the top surface and 8 attached to the underside of the panel. A temperature gradient will exist across the depth of the panel, therefore the upper surface of the panel is measured in addition to the lower surface, this gives a more representative temperature measurement. Thermocouples were affixed in the manner as displayed in Figure 5-10. Four of the thermocouples were mounted in the corners of the panel and the remaining four were fitted at distances of one-third of the horizontal and vertical length of the PV panel. The array of thermocouples will reduce the effect of temperature anomalies that may occur from uneven heating of the panel. In addition to the panel mounted thermocouples, a thermocouple is elevated away from the panel to measure the ambient air temperature in the surrounding test rig. The employed thermocouples were 0.2mm thickness; this was to interfere as little as possible with air stream across the panel surface.

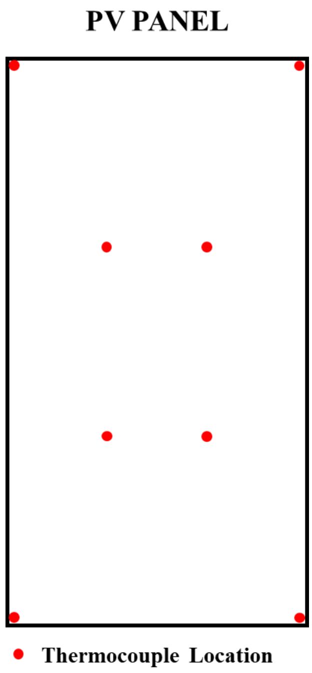

Figure 5-10. Position of thermocouples on the upper and lower surface of the PV panel

Pressure transducers were fitted to measure the tank pressure, pipe pressure and nozzle pressure. A flowrate sensor also measures the volumetric flowrate of air from the tank. These are displayed in Figure 5-11. Both types of devices output analogue voltage signals which are measured and calibrated to give a pressure and flow reading.

(a) (b)

Figure 5-11. (a) Example of pressure transducer used in test rig (b) Volumetric flow sensor used in test rig

The uncertainties of the employed sensors are provided in Table 5-4.

Table 5-4. Measurement uncertainty of employed sensors

Measurement	Sensor	Accuracy
Voltage measurement	Integrated Digital Multimeter	±0.10 [%]
Current measurement	Integrated Digital Multimeter	±0.10 [%]
Pressure	Pressure Transducer	± 0.25 [%]
Flowrate	Volumetric flowrate sensor	± 0.30 [%]
Temperature	Thermocouple	± 0.75 [%]

Figure 5-12 displays the measurement and control platform, relative to the test rig. The rig is entirely operated through the LABVIEW interface.

Figure 5-12. Control platform for system monitoring

The schematic presented in Figure 5-13 demonstrates the interaction between the hardware, instrumentation and control elements in the test rig. There are three primary elements in the rig: the compressed air channel, the electrical power channel, and measurement and control signals. The thermocouple array is comprised of the 16 thermocouples mounted to the top and underside of the panel as previously outlined, as well as the single individual thermocouple used for measuring ambient temperature. A LABVIEW interface was designed to monitor and control the test rig. The designed UI front panel of the LABVIEW programme is given in Figure 5-14.

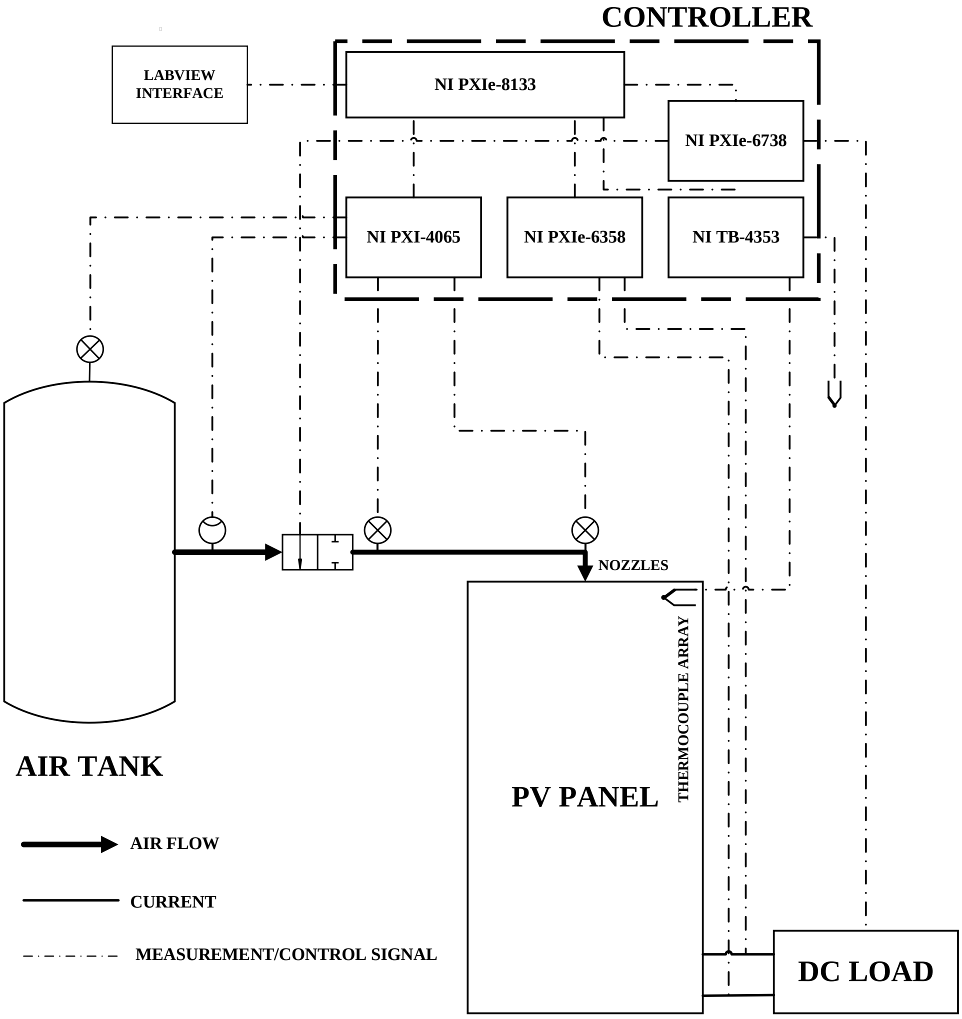

Figure 5-13. Schematic of components and control of PV-CAES test rig

The LABVIEW UI displays real-time data acquired from the instrumentation. The measured data for pressure and volumetric flowrate are displayed numerically and as a time plot. The current, voltage and power of the PV panel is additionally displayed numerically and as a time-plot. The individual thermocouple measurements are displayed and the average temperature of the panel is calculated. The resistive load can be set manually, or MPPT (discussed in 5.2.4.1) can be engaged through the switch. The pressure regulator valve is also controlled from the UI, where the desired pressure is numerically entered. The data is saved for later analysis through engaging the '*Data Save*' button.

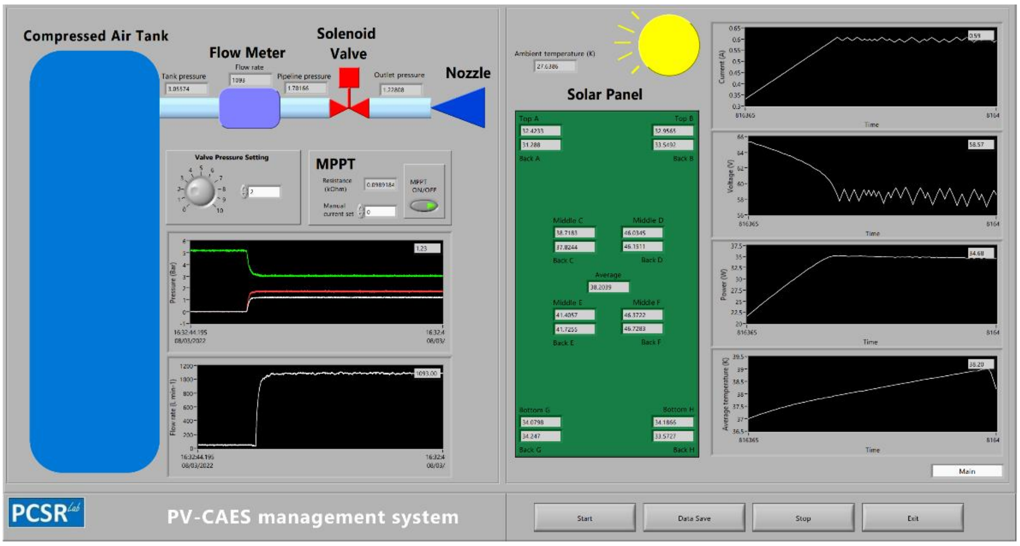

Figure 5-14. LABVIEW interface for managing PV-CAES test rig

5.2.4.1 Implementation of MPPT

MPPT is required in the test rig to assess the full benefit of CAES-based cooling and cleaning of PV panels. In PV installations at most scales, MPPT algorithms are implemented through the inverters, however in the test rig this effect is emulated through the dynamic alteration of the resistive load of the electrical DC load. Owing to the characteristic curves of PV modules as introduced in Section 3.1.2, as panels are soiled and heated, dramatic changes to their operation are observed. When cooling and cleaning is introduced, this can introduce rapid changes to the power generation and therefore large changes to the characteristic curves and potential power generation. Therefore, to better represent operational PV generation, MPPT is implemented in the test rig.

Figure 5-15 demonstrates a typical example of the effect of panel heating on the perceived power loss from PV generation. Without a dynamically changing load, the perceived power loss is greater when heating than when compared to the MPP of the elevated temperature panel.

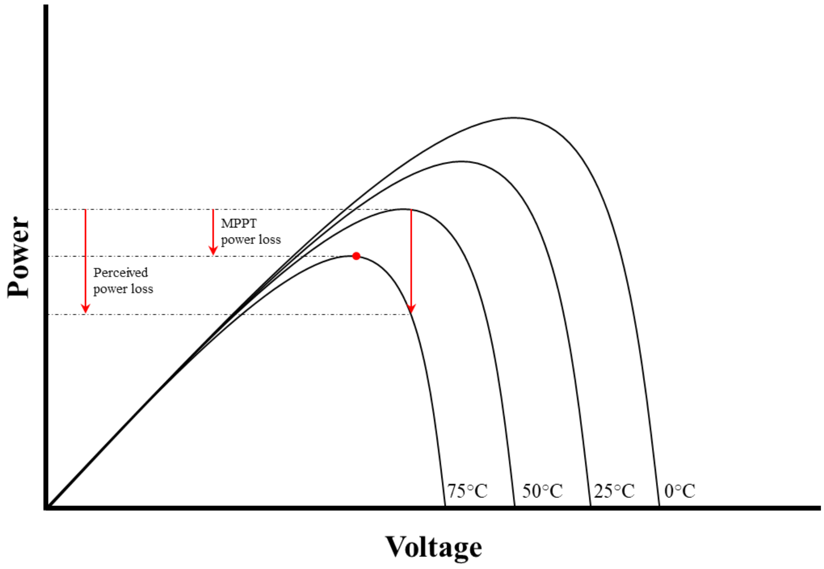

Figure 5-15. Panel heating and power loss with and without MPPT implementation

Conversely, Figure 5-16 demonstrates the necessity for MPPT implementation for a decreasing panel temperature. Convective cooling, which the PV panel will be subjected to will induce a reduction in panel temperature. Without MPPT implementation there is unrealised potential power generation as the panel would still be operating at the same voltage operation point although the instantaneous characteristic curve has changed.

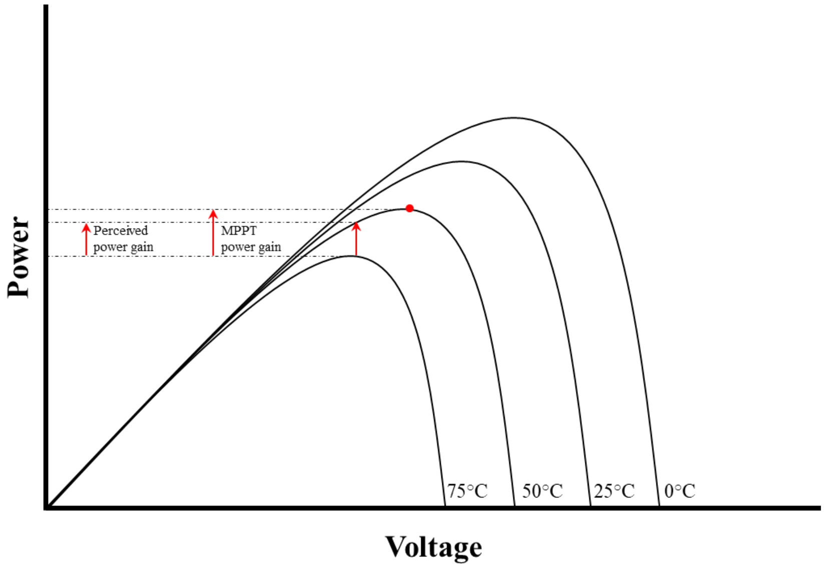

Figure 5-16. Panel cooling power gain with and without MPPT implementation

Similarly, the severity of soiling on the panel changes the power characteristic of the PV module. The amount of accumulated dust on the panel surface is proportional to the perceived level of solar irradiance experienced by the panel. Although the available solar radiation level may be high, a heavily soiled panel will experience a low level of irradiance because of the accumulated dust blocking and reflecting the light from reaching the photodiodes. Cleaning the panels with high velocity air is likely to induce rapid changes in perceived solar irradiance and therefore rapid changes to the operation of the PV modules. MPPT implementation is therefore recommended in the test rig to account for this and ensure the maximum power extraction benefit is demonstrated, representative of a commercial system. Figure 5-17 provides an example of the power generation difference for a typical PV panel with or without active MPPT. A decrease in solar radiance from 1000 Wm^{-2} to 500 Wm^{-2} could be analogous to a clean panel and heavily soiled panel, operational under 1000 Wm^{-2} input radiation.

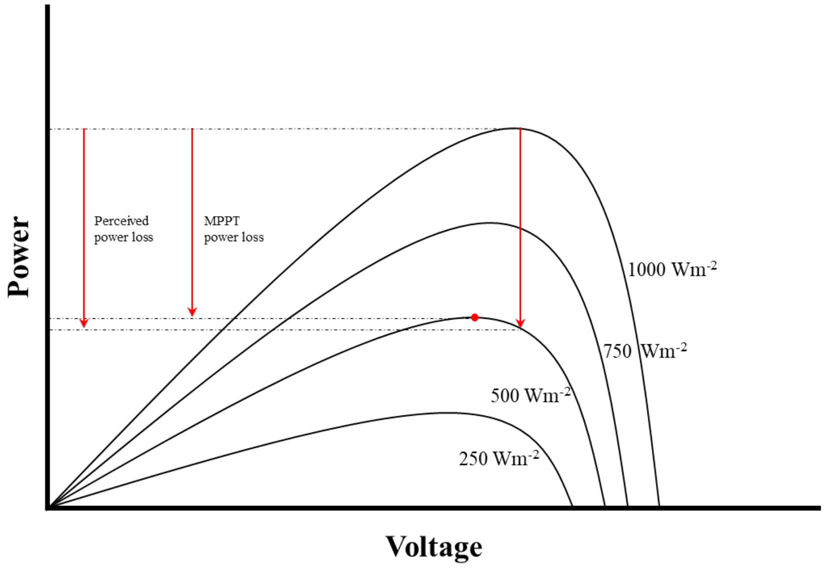

Figure 5-17. Panel soiling power loss with and without MPPT implementation

The impact of MPPT relating to cleaning effects will be less of that than of cooling effects owing to the greater influence of temperature on the open-circuit voltage of PV panels. Irradiance primarily effects the short-circuit current. Although MPPT impacts will be less, greater power extraction will be achieved for between clean and soiled panels because of the implementation of MPPT algorithms.

Figure 5-18 conversely demonstrates the difference in power generation with a fixed operation point or MPP tracking with a panel subject to rapid cleaning. Rapid cleaning of a PV panel will correspond to a large perceived increase in available solar irradiance. The operating voltage should increase to account for this and extract the maximum available power.

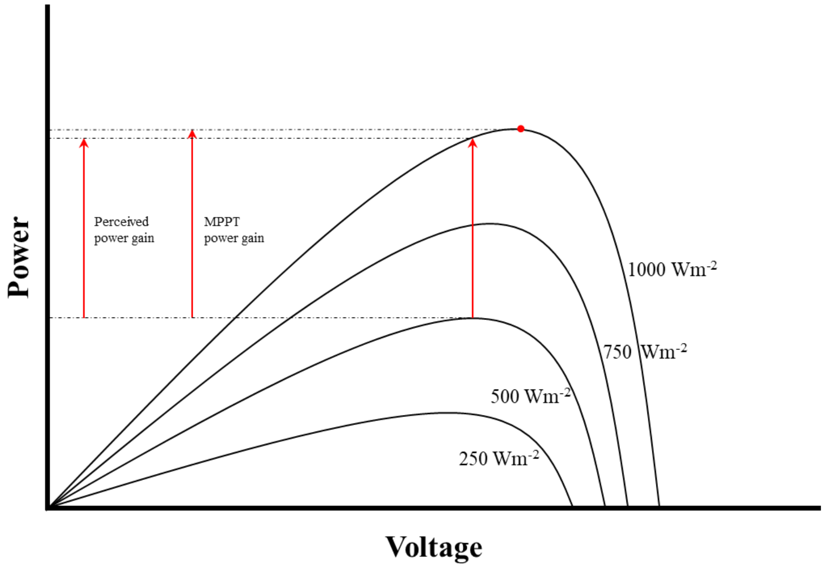

Figure 5-18. Panel soiling power gain with and without MPPT implementation

The MPPT algorithm chosen to be implemented in the test rig was Perturb and Observe (P&O). This is because of its wide adoption in commercial PV operation and the simplicity and robustness of the method [236]. For the P&O algorithm a small perturbation is introduced in the operating voltage, with the power output determined before and after the action. If the power output increases after the perturbation, then the perturbation is repeated. If the power decreases because of the perturbation, then the action is reversed and the effect on the resultant power is measured. An expression of the P&O algorithm, implemented in the test rig is given in Figure 5-19.

The MPPT control is implemented through LABVIEW logic. The voltage and current are measured and the output power is calculated. In the following loop iteration, the power is again calculated and the logical sequence as described in Figure 5-19 is carried out. The platform then sends a signal to the electronic load to vary the resistance, changing the operating point of the PV panel.

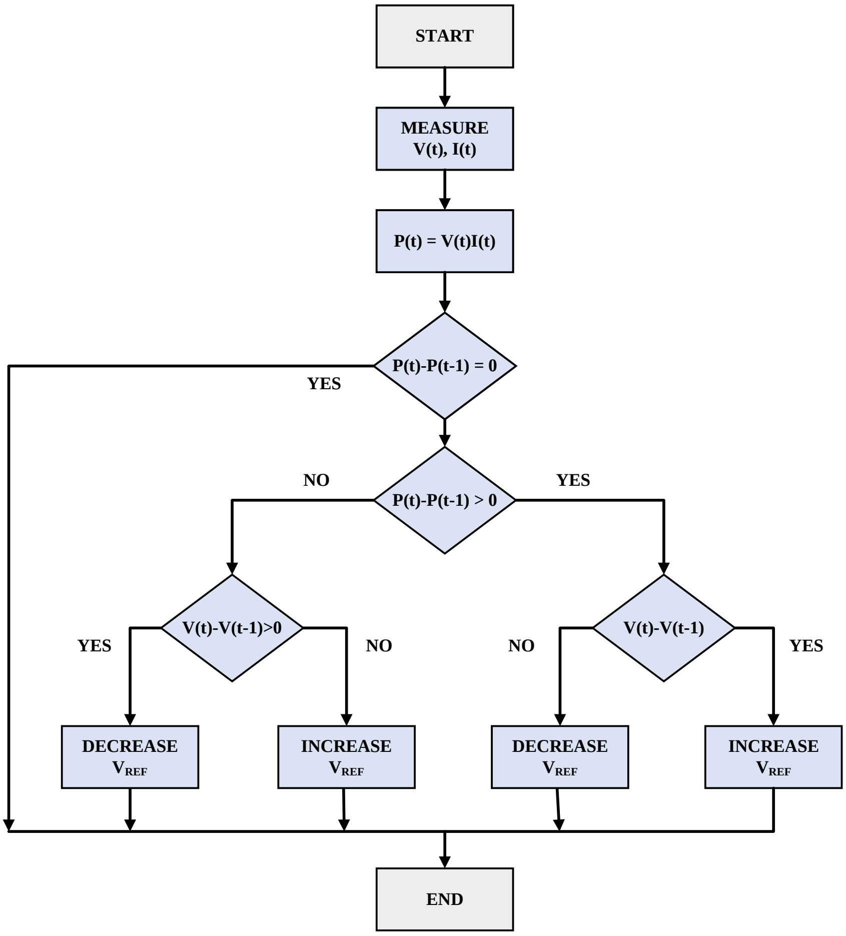

Figure 5-19. Perturb and Observe MPPT algorithm implemented in test rig

5.2.5 Test-dust

As discussed in Section 3.2., particles in the range of 2-63μm contribute the most to panel soiling. The mean size of particles contributing to soiling power losses has been reported as 15-30μm [129], 9-25μm [237] and 10-32μm [238]. Test-dust to be deposited on the surface of the PV panel is sourced to emulate these soiling conditions as far as is practically feasible. Talc was deemed as the suitable candidate for test-dust as it is naturally occurring, readily available in the required particle diameter range and does not impose significant safety restrictions. Additionally, talc has been previously used in laboratory solar PV soiling studies [239–241] for the purpose of emulating natural soling effects.

A scanning electron microscope (SEM) image of the talc as test-dust for the experimentation was obtained and is shown in Figure 5-20. The material composition and properties of the talc are provided in Table 5-5. From the SEM analysis it was estimated that the average diameter of the talc used as test-dust for experimentation was approximately 20μm, therefore was deemed to be suitable for use as test-dust.

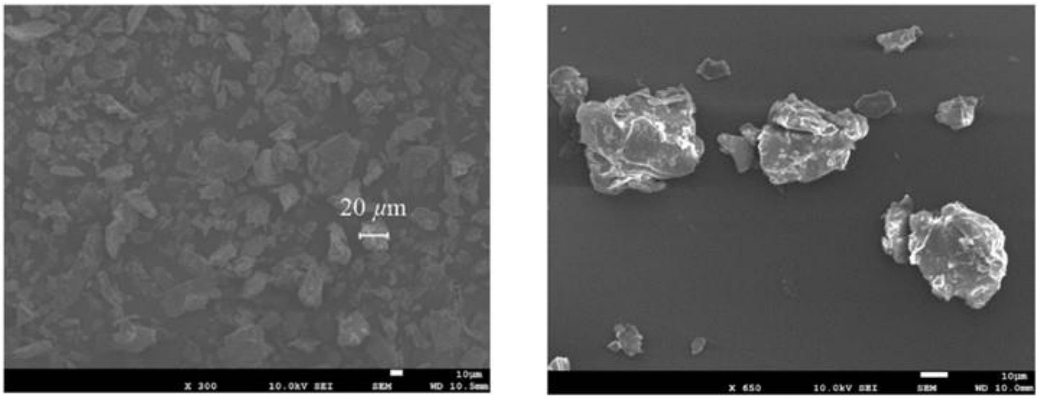

(a) **(b)**

Figure 5-20. (a) Test-dust under 350 times magnification (b) Test-dust under 600 times magnification

Table 5-5. Material properties of test-dust employed in testing [242]

Feature		**Value**
Composition	[%]	SiO_2 (63.37), MgO (31.88), H_2O (4.75)
Density	[kg m^{-3}]	2700

5.2.6 Full Assembly of the Test Rig

The final assembly of the test rig is shown in Figure 5-21. A clear greenhouse was employed as containment for the test rig to act as a barrier between the rig and external laboratory environment. This containment retains dust blown from the panel surface and acts as a barrier from to the high velocity air. Additionally, the greenhouse insulates the test rig and raises the internal ambient temperature and is useful for emulating the ambient temperatures of hot, arid environments of some PV installations.

A complete list of components and their manufacturers is contained in Appendix C.

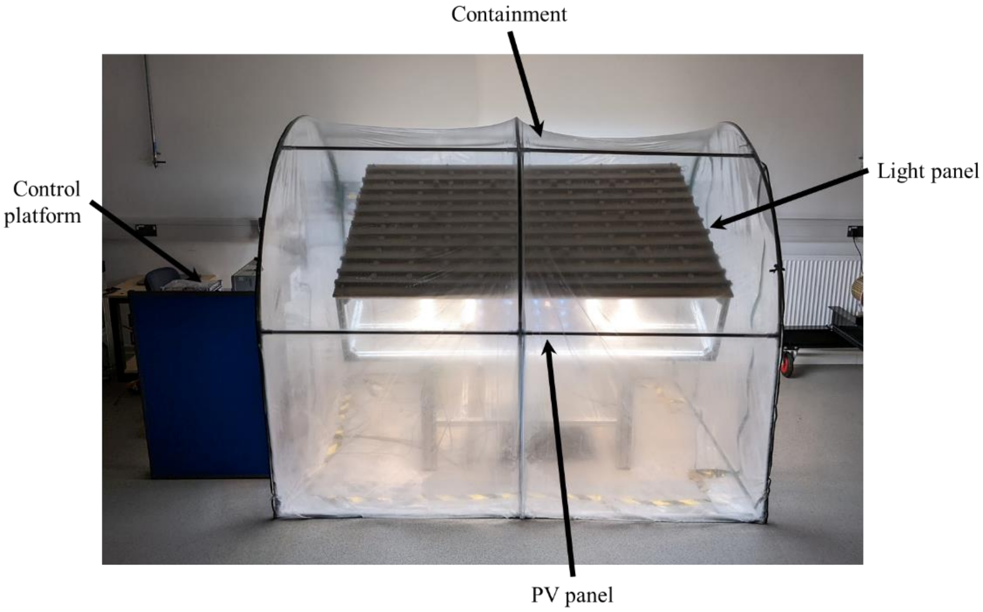

Figure 5-21. Final test rig within containment

5.3 Summary

A test rig is required to demonstrate the feasibility of using compressed air to clean commercial scale PV panels and to validate the full system dynamic mathematical model established in Chapter 4. The main functional requirements have been identified and the resulting test rig has been outlined, with the elements of the test rig described in detail.

The constructed test rig can generate an irradiance value of up to 547 Wm^{-2} over a panel bed that can accommodate a commercial scale solar PV panel, inclinable up to 45°. The rig additionally can heat the panels through the installed heat lamps. An established compressed air system allows the operator to blow air over the panels at high speed. The PV panel is connected to a programmable DC load and voltage and current of the PV panel can be measured. The temperature of the panel and of the ambient environment is measured from an array of thermocouples. The pressure of the CAES system and volumetric flowrate of the air being delivered to the panel is additionally measured. The system is controlled via a central control platform and a LABVIEW interface has been established to monitor the measured data in real-time. The interaction of the sensors and control elements of the test rig are highlighted. Test-dust is acquired to emulate soiling effects that PV panels experience. MPPT has been established through the control platform and the programmable DC load to demonstrate the maximum effect of panel cleaning and cooling to the PV power output. The test rig is contained within a greenhouse containment unit to isolate the test rig from the external laboratory environment. The completed test rig is of a flexible nature that is easily adaptable and therefore is very useful in terms of potential testing functionality. The modular nature of the developed test rig allows for a multitude of testing options and investigations to be pursued. The specific individual components and hardware implemented in the test rig are given in Appendix C.

Chapter 6 – Mathematical Model Validation and System Performance Analysis

In this chapter, the dynamic mathematical model of the proposed PV-CAES system is validated by comparison to experimental results gathered from the constructed test rig. The validated model is subsequently used for a system performance analysis to assess the potential benefits that can be brought to PV generation from panel cleaning and cooling.

As with the mathematical model outlined in Chapter 4, elements contained within this chapter have been presented in the previously indicated publications [208,209].

6.1 Mathematical Model Validation

Experimental validation of the dynamic mathematical model described in Chapter 4 using data obtained from the test-rig described in Chapter 5 is presented in this section. The key parameters of the relevant devices and mechanisms for validation are presented in Appendix D. Parameters of the employed PV panel were measured experimentally from a characterisation test of the panel under standard conditions; comparison of the model prediction of the PV characteristic and the measured characteristic is also presented in Appendix D. Where parameters used in the modelling could not be directly measured, parameters were assumed, with these indicated within the relevant sections of model validation.

The individual mechanisms of the dynamic mathematical model are validated separately to assess accuracy and then compiled into a full system model of the PV cleaning and cooling system. The individual mechanisms that are validated experimentally in this section are listed:

- Natural convective effects on panel temperature
- Forced convective effects on panel temperature
- PV generation
- Panel soiling and effect on PV generation
- Panel cleaning and effect on PV generation
- Air tank discharging through established nozzle system

6.1.1 Panel Temperature and Generation

6.1.1.1 Natural Convective Effects

For the validation of the heating and cooling of the PV panel from natural convection, a 100W panel is placed horizontally in the test-rig and illuminated by the light-panel. The power output of the PV panel is measured throughout this period. For the validation test, the panel is powered by the light-panel for 1-hour and then the light is powered-off, with measurements continued for an additional 30 minutes. The panel is subjected to the maximum available irradiance from the test rig of 547 Wm^{-2} for the 1-hour generation period. As previously indicated, the parameters for the PV panel employed are provided in Appendix D. The measured ambient temperature was used as input for the simulation. The test was completed three times and the experimental results were averaged. The comparison of the model prediction and measured panel temperature is given in Figure 6-1.

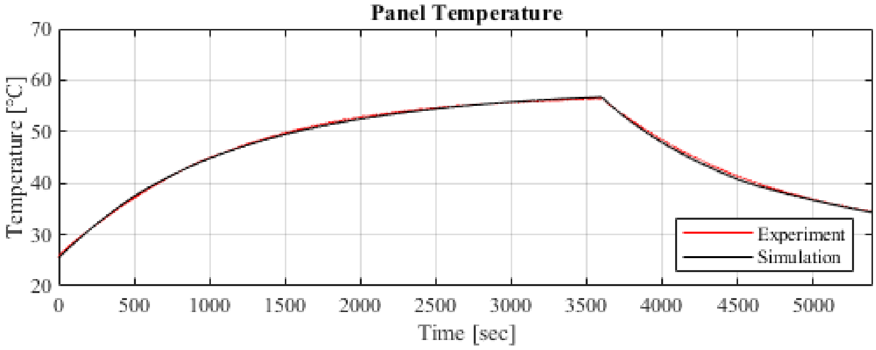

Figure 6-1. Panel temperature comparison

As can be observed in Figure 6-1, the panel temperature increases throughout the 1-hour period when the light-panel is illuminated (t=0 to t=3600s) and decreases when the panel is not illuminated (t > 3600). There is a good fit between the model prediction and experimental measurements for both the periods where the panel is subject to the illumination as well as after the light-panel is switched-off. The maximum recorded panel temperature from the experimentation is 56.4°C and the maximum temperature predicted by the model is 56.7°C; the final measured panel temperature is 34.5°C with the model predicting 34.3°C. The average relative error between the measured and simulated temperature is 0.56% for the period of the test[10].

The PV panel power generation is additionally modelled during this period, with the simulated temperature used as the input for the PV generation model. Measured resistance load values from the DC load during the experiment, while running the P&O MPPT algorithm, were digitally filtered and used as input for the mathematical model. Figure 6-2 to Figure 6-4

---

[10] The average relative error between the experimental results and the simulation is determined through the relative error equation: $\left|\frac{x-x_{sim}}{x}\right|$ and provided in terms of %, for each measured point and simulated value at the same corresponding time. The mean value of these errors is then taken to determine the average relative error.

demonstrate the comparison of the model output to the voltage, current and power measurements respectively.

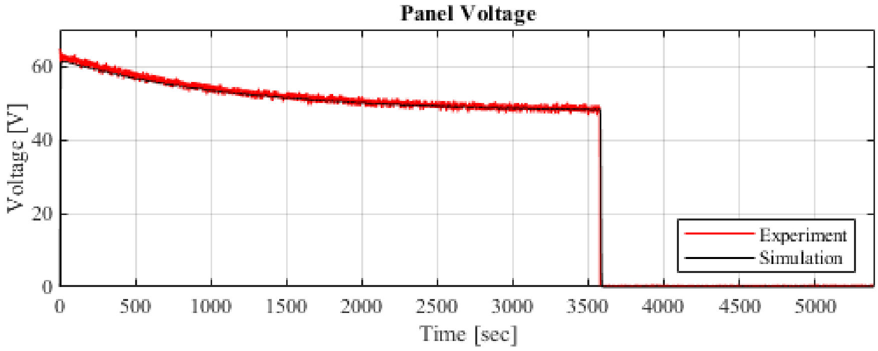

Figure 6-2. Panel voltage comparison

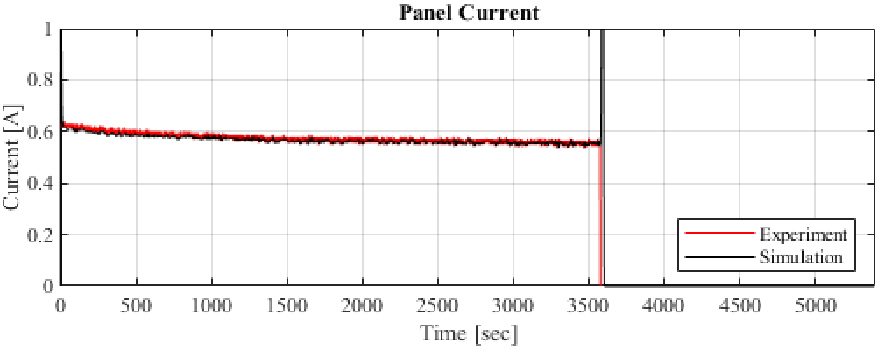

Figure 6-3. Panel current comparison

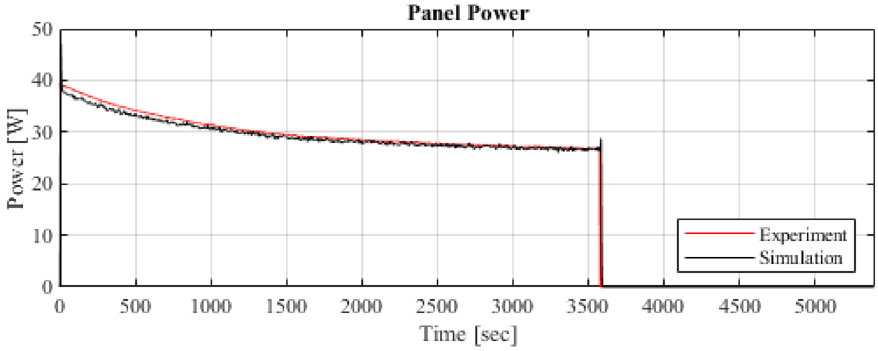

Figure 6-4. Panel power comparison

Observing Figures 6-2 to 6-4, the PV mathematical model predicts the measured panel output to a high accuracy. Note, the decrease in voltage, current and power during the heating phase of the panel, with no voltage, current and power measured at the point at which the lighting-panel is switched-off. There is a large spike in simulated current at the point at which the input radiation is removed; this is attributable to the rapid drop in calculated voltage causing a reduction in the calculated diode saturation current and causing output current calculation to spike for a short duration. The simulated current spike does not affect the overall accuracy of the model. The average relative errors, between the simulated PV performance and measured performance of the voltage, current and power are 1.4%, 1.6% and 1.9% respectively. A summary of the average relative errors is provided in Table 6-1, with the relative error between the predicted total energy generation during the period and the total measured energy generation, across the period is given in Table 6-2.

Table 6-1. Average relative errors for natural convective effects

Compared Mechanism	**Average relative error [%]**
Panel temperature	0.56
Panel voltage	1.4
Panel current	1.6
Panel power	1.9

Table 6-2. Comparison of experimental and simulated energy generation

Experimental Energy [kWh]	**Simulated Energy [kWh]**	**Relative Error [%]**
0.0299	0.0294	1.7

Observing Tables 6-1 and 6-2, the mathematical model of the natural convective effects and its influence on the PV generation provides a satisfactory representation of the physical system. When incorporated into a full-system model for further analysis, these mechanisms can be trusted to give an accurate simulation of the panel subjected to the natural convective effects.

6.1.1.2 Forced Convective Effects

Experimental validation of the forced convection mathematical model is demonstrated. Nozzles are arranged in the manner demonstrated in Figure 6-5. Two nozzles were affixed to the top edge of the panel with a combined nozzle outlet area of 15.4 mm^2; nozzles were mounted one-third of the width of the panel from the edge with the same distance again between the other nozzle. The specific nozzle is listed in Appendix C as part of the test rig hardware.

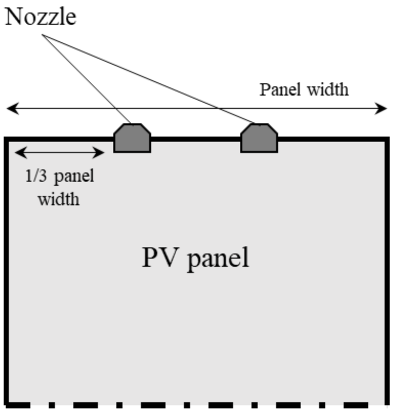

Figure 6-5. Nozzle orientation for mathematical model validation

As with the natural convection mathematical model validation, the panel is placed horizontally in the test-rig and subjected to radiation from the light-panel. The panel was heated to a temperature of 50°C and then subjected to airflow at a rate of 800 Lmin^{-1} for a period of 3-minutes, whilst continuing to be illuminated by the light-panel at the maximum deliverable irradiance value. The measured flowrate data was used as input for forced convection model with the panel air velocity calculated. The procedure was completed three times, with the average of the results used for comparison. The comparison of the experimental and simulated temperature comparison is given in Figure 6-6.

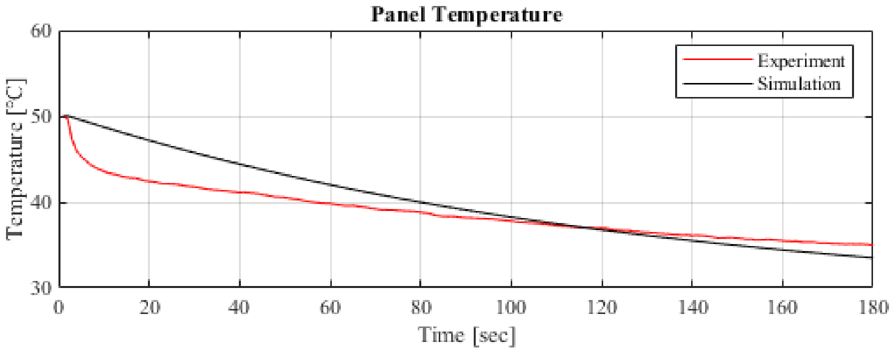

Figure 6-6. Panel temperature comparison for forced convective cooling

Figure 6-6 demonstrates the experimental versus simulated temperature of the PV panel across the 3-minute cooling duration at 800 Lmin^{-1}. The final measured panel temperature is 35.0°C and the final simulated temperature is 33.5°C. Initially, the experimental temperature decreases at a high rate, this is likely attributable to the measurements from the thermocouples affixed to the upper surface of the panel are cooler than the panel itself, relative to the thermocouples on the underside of the panel. The average relative error between the panel temperature over the measurement period is 4.4%.

The forced convective panel cooling is additionally validated in conjunction with the natural convective panel heating and PV power generation. As in Section 6.1.1.1, with the natural convective effect validation, the panel is subjected to the maximum deliverable by the test rig for a period of 1-hour. The panel is subsequently subjected to 3-minutes of cooling at 800 Lmin^{-1} flowrate with the panel continued being powered by the light panel. The test is continued for an additional 27-minutes, with the temperature and panel output measured for the remainder of this time. The airflow was fed from the mains air supply, to sustain a constant flowrate, which would drop over time given a fixed supply of air. The comparison between the experimental and simulated temperature subject to cooling are shown in Figure 6-7. The measured flowrate data was used as input for the simulation for the air velocity determination and the measured resistive load values were digitally filtered and used as input to the simulation for panel power calculation. As before, the test was undertaken three times and the averaged data was compared.

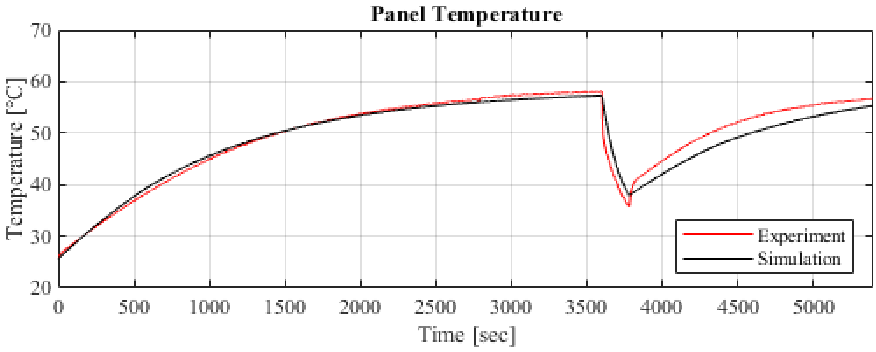

Figure 6-7. Panel temperature comparison with 3-minute cooling period

Figure 6-7 shows a good fit between the predicted temperature and measured temperature from the test. The panel temperature increases throughout the 1-hour period when the light-panel is illuminated (t=0 to t=3600s). At the point at which the airflow beings, the panel temperature is reduced in both the experimental results and the simulated results. During the cooling period, the measured panel temperature reduced from 58.1°C to 35.7°C, with the simulated temperature from 56.9°C to 38.0°C. After the 3-minute cooling period, the panel temperature increases for the remainder of the test in both measured data and simulated. The final temperature measured at the end of the test is 56.8°C, with the simulated value being 55.3°C. The average relative error between the measured and simulated temperature with the inclusion of forced convective cooling is 2.5%.

The PV panel output is additionally measured during the test period. The voltage, current and power generated by the PV panel throughout the test, along with the model prediction is given in Figures 6-8 to 6-10.

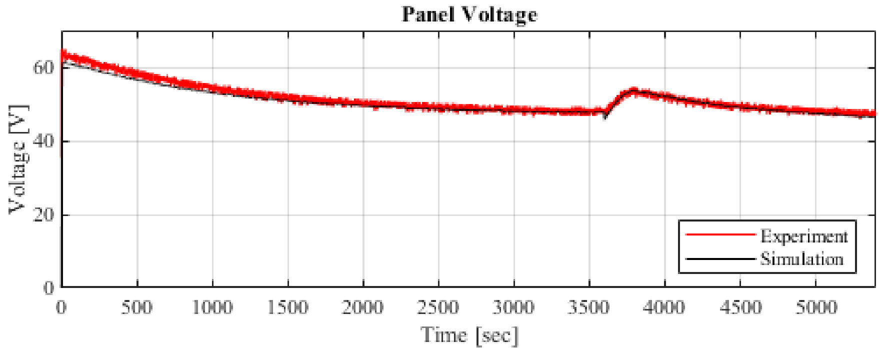

Figure 6-8. Panel voltage comparison with cooling

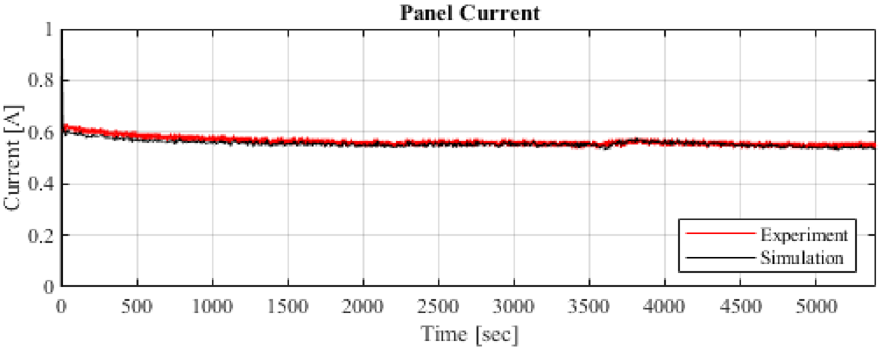

Figure 6-9. Panel current comparison with cooling

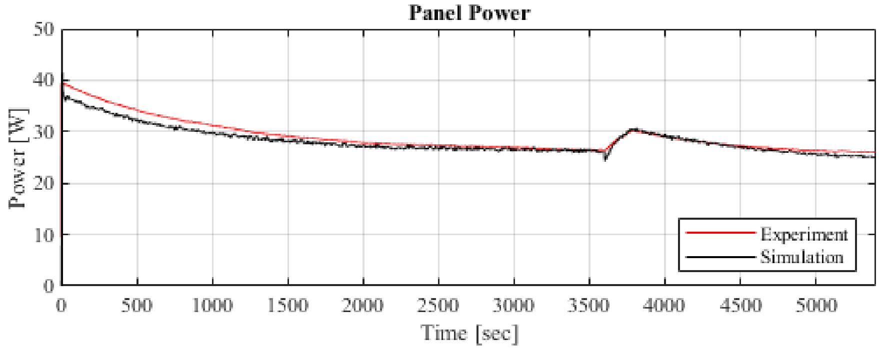

Figure 6-10. Panel power comparison with cooling

Observing Figures 6-8 to 6-10, the PV mathematical model fits the panel performance well subject to the forced convective cooling from the airflow. An increase in power output from the PV panel is measured because of the cooling of the PV from the compressed air flow. The test rig recorded an increase in power output because of the cooling from 26.5W to 30.2 W, whereas the model predicted an increase of 26.1W to 30.5W. The dynamic mathematical model slightly overpredicts the benefit of the panel cooling to the PV generation. However, the average relative errors between the simulated PV performance and measured performance of the voltage, current and power are low, determined to be 1.9%, 2.1% and 3.4% respectively. These errors, along with the relative error of temperature are summarised in Table 6-3.

Table 6-3. Average relative errors for forced convective cooling

Compared Mechanism	Average relative error [%]
Panel temperature	2.5
Panel voltage	1.9
Panel current	2.1
Panel power	3.4

The total energy generated by the PV panel during the test is compared in Table 6-4.

Table 6-4. Comparison of experimental and simulated energy capture

Experimental Energy [kWh]	Simulated Energy [kWh]	Relative Error [%]
0.0434	0.0423	2.8

The low average relative errors of the panel temperature and energy generation by the PV panel owing to the cooling effect of the compressed air blowing indicates that the mathematical models for the PV generation, natural convection and forced convection are validated and can be used for further analysis of the system performance.

6.1.2 Soiling Effect, Compressed-air Cleaning and PV Generation

The mathematical model of panel soiling and cleaning impact to PV power generation is validated experimentally in this section, from data acquired from the test rig. The same 100 W panel used for temperature modelling validation was placed in the test rig with the same nozzle arrangement as displayed in Figure 6-5. Again, the relevant parameters pertaining to the PV panel used for mathematical model validation are given in Appendix D. The panel was inclined to 30° for the tests.

The acquired talc used for testing possesses an average diameter of 20μm as discussed in Section 5.2.5. From the modelling study presented in Section 4.3 and using the specific panel parameters, the required velocity for particle detachment is estimated. This is presented in Figure 6-11. Note, the particle adhesion validation was conducted in dry conditions, therefore capillary forces are negated, with only electrostatic and Van der Waals forces impacting to overall adhesion force.

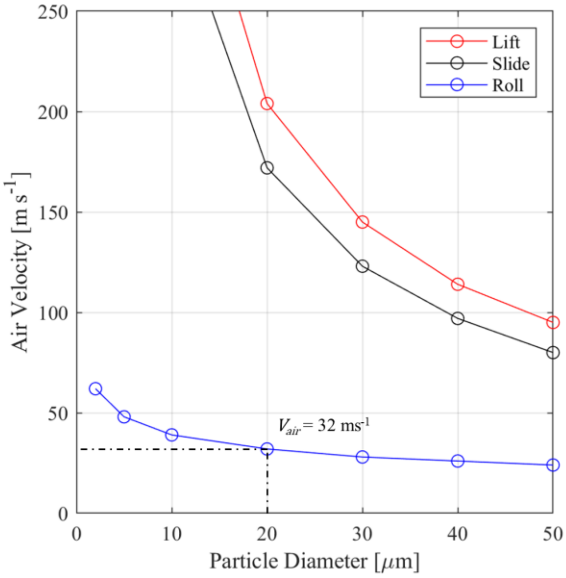

Figure 6-11. Required detachment velocity for particles and panel established in test rig

From the analysis, detachment will occur at an air velocity of 32 ms^{-1} for the rolling detachment criteria. With the established nozzle installation, this corresponds to a flowrate of 745.3 Lmin^{-1}. Talc was deposited on the surface of the PV panel uniformly through a sieve and the voltage and current output was measured under the greatest deliverable irradiance of 547 Wm^{-2}. Quantities of 5.2g, 10.4g and 15.6g of dust were deposited on the panel surface. At a soiling rate of 0.5 g m^{-2} day^{-1} and for the established panel dimensions, this corresponds to the equivalent of 2-weeks, 4-weeks and 6-weeks of dust accumulation. The panel was subjected to 10 s airflow through the nozzles, to prevent the redeposition of the adhered particles and give sufficient the removal along the length of the panel. For each test, the initial panel temperature was established at 30°C. The power output of the panel was recorded during the test period.

Tests at each of the soiling levels was repeated three times and the data was aggregated. The power recovery from the airflow to the panel surface is summarised in Table 6-5.

Table 6-5. Power recovery from compressed air cleaning of PV panel

Mass of Deposited Dust [g]	**5.2**	**10.4**	**15.6**
Initial Soiled Power [W]	34.43	32.02	29.11
Cleaned Power [W]	37.59	35.65	35.59
Soiled Power [% of unsoiled]	86.5	80.5	73.1
Cleaned Power [% of unsoiled]	94.4	89.6	89.4
Recovered Power [% of unsoiled]	58.8	46.7	60.1

As Table 6-5 indicates, the compressed airflow is successful at improving the power output of the PV module by removing dust present on the panel surface. However, the test indicates that the compressed air cleaning does not result in full cleaning of the panel as the model predicts, this can be observed in Figure 6-12 demonstrating the impact of the cleaning process on the PV panel. Furthermore, observing Table 6-5, the data suggests that the system can only clean the panel to a certain level. For example, the power recovery percent is lower for a 10.4 g soiling rate, than the 15.6 g soiling rate. This is because the system removes dust to the same degree, but this means the recovery percent is higher for the more heavily initially soiled panel.

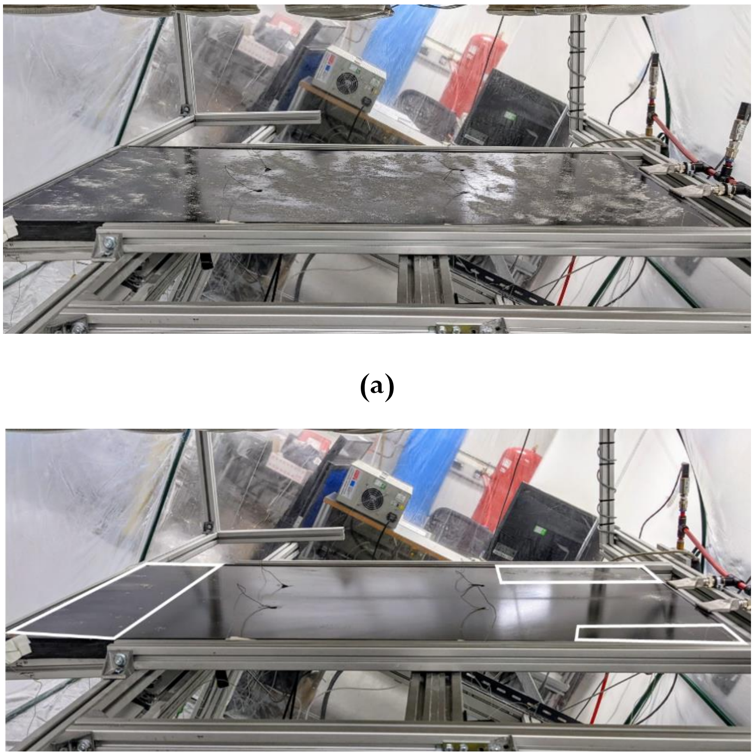

(a)

(b)

Figure 6-12. (a) Panel before cleaning (b) Panel after cleaning. Note: the white-bordered regions indicate visible residual dust on the panel surface after blowing

After each test there is still visible dust present on the surface of the panel. This is particularly evident for the upper corners, to the side of the nozzles, and the far edge of the panel where some dust accumulated. Additionally, some dust remained on the surface of the panel as it is likely of a diameter too small to be removed by the implemented flowrate. These factors account that full power recovery is not achieved. For the tests across all particle deposition rates, the average power recovery of the unsoiled power value was 55% from the soiled value after the air discharging across the panel surface. This factor is subsequently incorporated into the mathematical model such that if the detachment criteria are met, 55% of the dust on the panel surface is removed rather than full particle mass detachment.

For the model validation, the measured flowrate during the tests was used as the input for simulation for the velocity calculation. Additionally, the measured resistive load data was filtered and used as input for the model. The previously validated temperature model is additionally operating simultaneously, however over the short test period, temperature effects do not produce a great impact on the PV output.

Figure 6-13 to 6-15 compare the dynamic model prediction to the experimental prediction for amounts of deposited dust on the panel surface, with the incorporated cleaning factor.

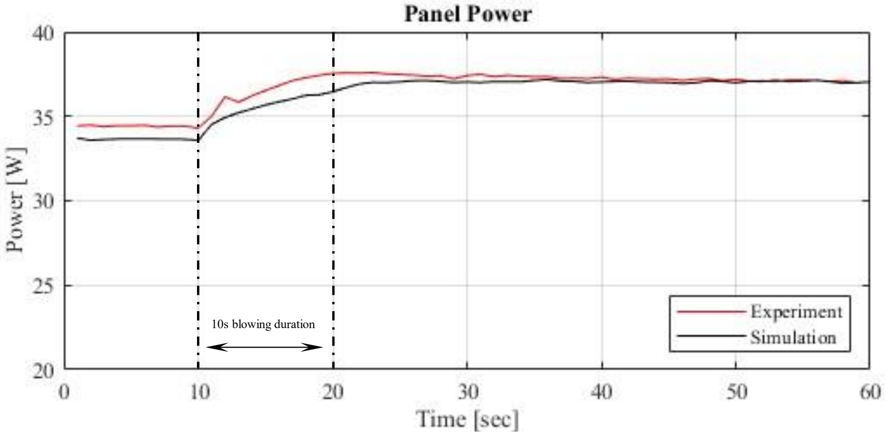

Figure 6-13. Panel power with 5.2g deposited followed by cleaning

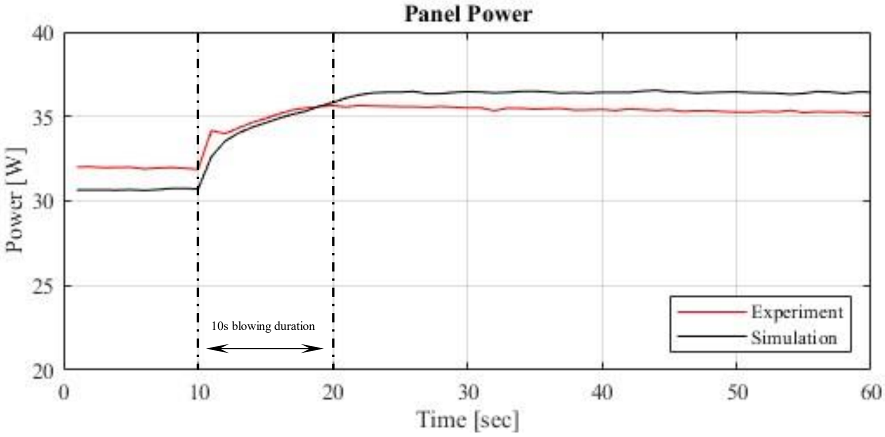

Figure 6-14. Panel power with 10.4g deposited followed by cleaning

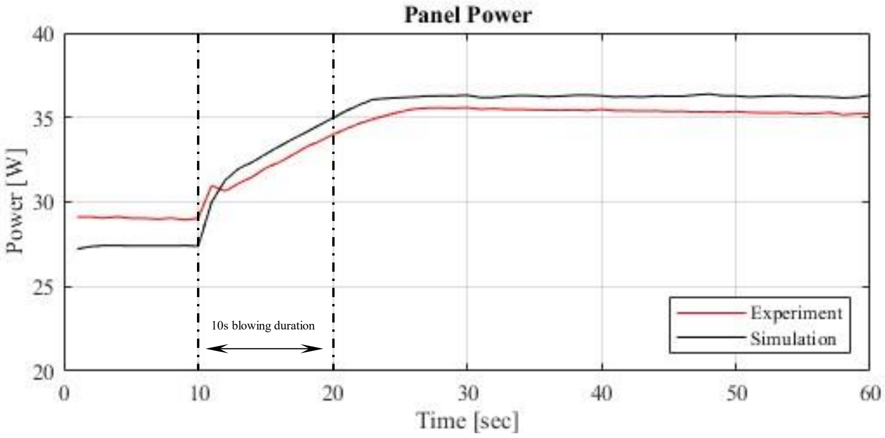

Figure 6-15. Panel power with 15.6g deposited followed by cleaning

Observing the comparisons of predicted soiling and cleaning effects in Figures 6-13 to 6-15, it can be determined that at the low soiling rate, as in Figure 6-13, the model gives a good approximation of the impact of soiling and the cleaning benefit, at the higher soiling levels as in Figure 6-14 and Figure 6-15, the model overestimates the reduction in panel power output and additionally overestimates the benefit to the panel cleaning from the compressed air blowing, though with the established cleaning factor, the overall prediction in power improvement is good. The errors between the model and the experimental values are given in Table 6-6. The continuing power output increase for the period after the panel cleaning is finished, most pronounced at the 15.6 g deposition mass, as in Figure 6-15, is attributable to the MPPT algorithm which is continuously altering the operating voltage and has not yet established to optimum post-cleaning operating voltage owing to the large change in perceived radiation to the panel.

Table 6-6. Summary of cleaning modelling validation

Mass of Deposited Dust [g]		**5.2**	**10.4**	**15.6**
Initial Power	Measured [W]	34.43	32.02	29.11
	Simulated [W]	33.71	30.70	27.22
	Rel. Error [%]	**2.1**	**4.1**	**6.5**
Cleaned Power	Measured [W]	37.59	35.65	35.59
	Simulated [W]	37.04	36.47	36.32
	Rel. Error [%]	**1.5**	**2.3**	**2.1**

Average relative error [%]	1.2	2.7	3.1

Table 6-6 demonstrates the relative errors between the panel power prediction from the soiling model to cleaned model after the cleaning factor has been incorporated. The relative errors are low, though increases at higher soiling rates. For low levels of soiling, the soiling and detachment model can be assumed to give a reasonable representation of the experimental system.

6.1.3 Tank Discharging

The final experimental validation of the dynamic mathematical model element is tank discharging. The 200 L air tank was charged to 7 bar gauge. The outlet valve subsequently fully opened and the air allowed to flow from the tank through the nozzle outlet. The tank pressure and flowrate through the pipe system was measured during this time. The simulated tank discharge for the same initial conditions is demonstrated along with the experimental measurements in Figure 6-16.

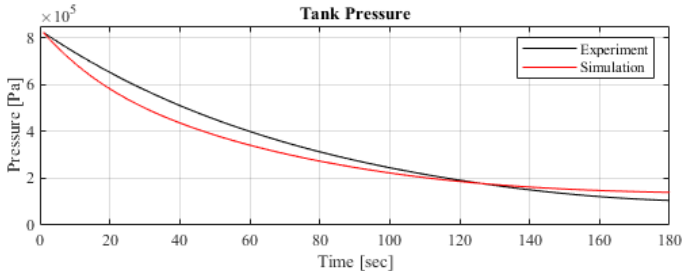

(a)

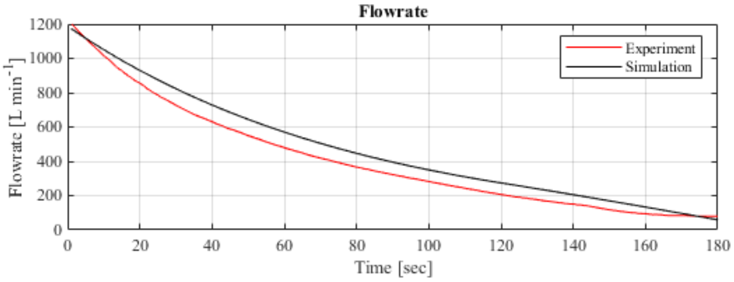

(b)

Figure 6-16. (a) Discharging tank pressure comparison (b) Flowrate comparison

Figure 6-16(a) demonstrates the discharging tank comparison of for the air tank pressure. The model prediction is a reasonable fit. Pressure values are provided in absolute value, with 7 bar gauge equivalent to 8.1 × 10^5 Pa. The experiment was concluded after 180 s with the final measured pressure reaching 1.4 × 10^5 Pa and the model predicting 1.3 × 10^5 Pa. The average relative errors between the model values 12.5%. Figure 6-16(b) shows the flowrate comparison between the discharging air tank. As with pressure, the model gives a reasonable prediction. The initial measured flow rate is 1173 $Lmin^{-1}$ and the final flow rate being 59 $Lmin^{-1}$, the model predicts 1233 $Lmin^{-1}$ and 109 $Lmin^{-1}$ for the same values respectively. The model generally overestimates the flowrate compared to the measured value, possibly attributable to the simplifications made in the air component modelling by not accounting for pipe friction. The average relative error between the experimental and simulated data is 12.3%. Table 6-7 provides the average relative errors for the air system measurements.

Table 6-7. Average relative errors for air system

Compared Mechanism	Average relative error [%]
Tank Pressure	12.5
Flowrate	12.3

The average relative errors for these mechanisms are greater than that of the other mechanisms, though the model still predicts a reasonable fit of the experimental measurements. The overall duration and final measurements are predicted to a satisfactory degree and are incorporated into the full system model.

6.2 System Performance Analysis

The elements of the dynamic mathematical model have been experimentally validated. The validated model components are used for a broader system performance analysis to determine the possible benefit to PV generation from the system operation and to advise a strategy for operation.

Solar irradiance data for a single December day in Kharagpur, India is taken for analysis and used as input for the full system mathematical model; the solar data was measured locally using a reference cell-based irradiance sensor, recording at an interval of 5 minutes. The same panel parameters used for experimental validation are employed for the system analysis, these are contained in Appendix D. The developed model can be used to simulate the operation of the system across long periods. The temperature achieved by the panel and power output are calculated. Furthermore, to demonstrate to benefit of the potential cleaning effects to the PV generation, a simulated mass of 5.2 g of dust is deposited onto the surface of the panel and the power simulated again; this is equivalent to a typical soiling rate of 0.5 g·m^{-2}day^{-1} for two weeks of exposure without cleaning. Particle size of 20 μm was again implemented as in the validation simulations. A 30° angle of inclination was set for the panel. Throughout the simulated day, maximum power point tracking is operational to ensure the PV is generating to its maximum potential. The parameters for the dust and soiling modelling are also contained in Appendix D. The input solar irradiance data and determined panel temperature for an unsoiled panel are demonstrated in Figure 6-17. The difference in power generation from the 100 W panel between soiled and unsoiled is shown in Figure 6-18.

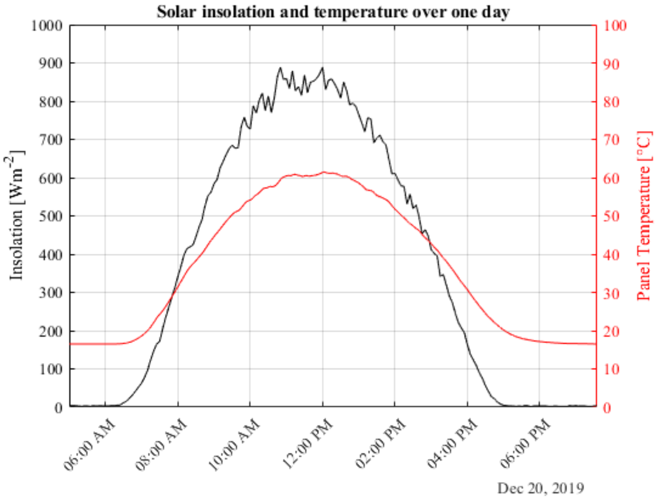

Figure 6-17. Input irradiance and panel temperature

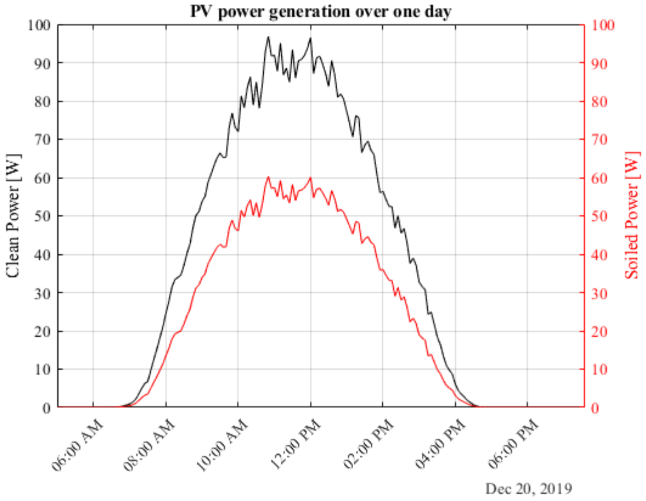

Figure 6-18. Panel power output across one day. The soiled panel is subject to 5.2g of dust on the panel surface.

Observing Figure 6-17, solar irradiance data for the period ranges from 0 – 900 Wm^{-2} and is representative of a clear day with little variation from the standard expected daily profile. The modelled peak temperature of the unsoiled PV panel mimics the profile of the solar generation but is offset with the peak temperature occurring marginally later than the peak solar value owing to the thermal inertia of the panel. The range of temperature of the PV panel is from 16°C – 60°C. The effects of the panel soiling can also be seen from the simulation results shown in Figure 6-18. Subject to the 5.2g of soil on the panel surface, a reduction in peak power output of 37% is observed, with the peak power reduced from 96.0 W to 60.8 W. This difference in power output between the two presented cases is the maximum that can be recovered from full cleaning of the panels.

With the soiling and temperature modelling demonstrated, it is of interest to assess the procedure of operation of the cleaning and cooling system that will give the greatest benefit. Given a fixed volume of compressed air at a given pressure, there are several discharging strategies that will impose different impacts to the panel:

- A high discharging flowrate will result in greater velocity flow blowing over the panel surface, however the blowing duration will be short as the stored air is discharged faster. Greater velocity flow will remove adhered particles more easily and will result in a greater drop in panel temperature, but for a shorter period.
- A low discharging flowrate will result in a slower air velocity across the panel surface; however the blowing duration will be extended as the stored air discharges at a slower rate. A lesser temperature drop will be achieved, but the cooled panel temperature will be maintained for a longer period.

This balance between air velocity and duration can be observed in Figure 6-19; a single 200 L air tank at 7 bar gauge is used for the demonstration, with parameters set for the same nozzle implementation as used for the validation and displayed in Figure 6-5.

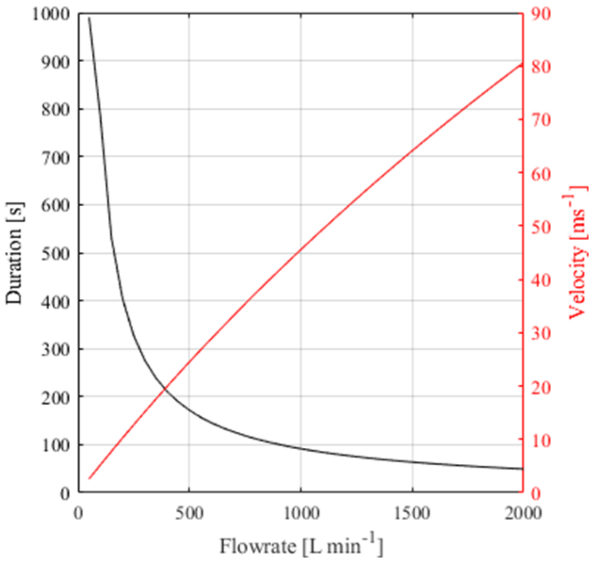

Figure 6-19. System flowrate determining discharge duration and air velocity

The balance between blowing duration and blowing velocity and the relative benefits to the PV panel generation from cooling and cleaning is therefore of interest. The time throughout the day at which the system is operated will also impact the benefit of the PV-CAES system, as the temperature profile of the panel varies across the day. The total energy generation from one PV panel over one day is established as the metric for assessing the increase in performance from the different discharging conditions. The same solar profile and input parameters as used for Figure 6-17 were used for the simulation as was the single air tank at 7 bar demonstrated in Figure 6-19. The study for assessing the cleaning and cooling benefits is undertaken for both a soiled and clean panel.

The system is simulated, subject to the solar irradiance data for Kharagpur day in December. As each day is simulated the conditions are the same at the beginning of the simulated day cycle. On each cycle, a single parameter is changed, either the flowrate or the start-time at which the air release is begun. The flowrate is varied from 400 Lmin^{-1} to 2000 Lmin^{-1} in increments of 100 Lmin^{-1}, and the start-time is varied between 7am to 6pm in periods of 30 minutes. The overall energy generated by the PV panel over the one-day period is recorded and stored. Figures 6-20 and 6-21 compare the impact of the air discharging on the PV panel generation for a soiled and clean panel. The soiled panel has simulated 5.2 g present on the surface.

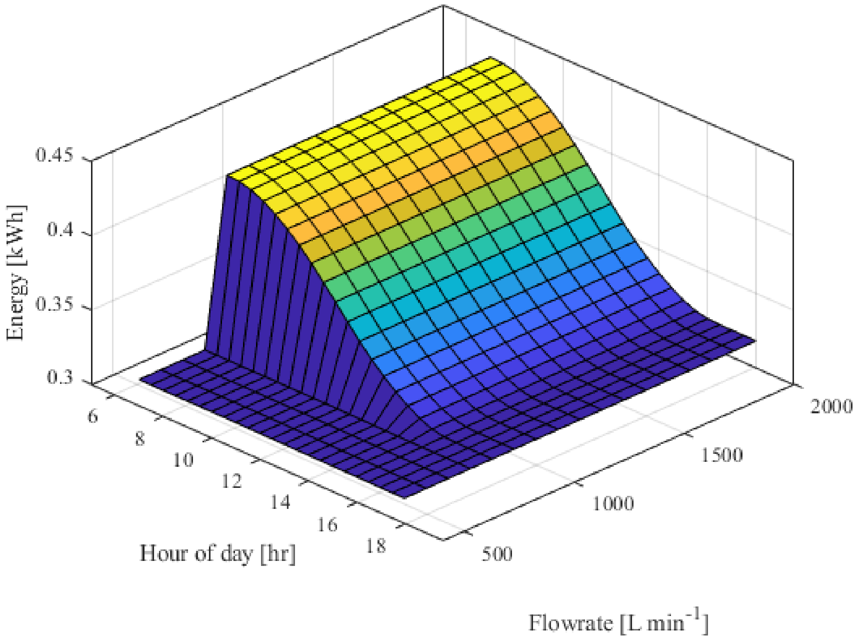

Figure 6-20. Impact of blowing duration and start-time on energy generation for a soiled panel

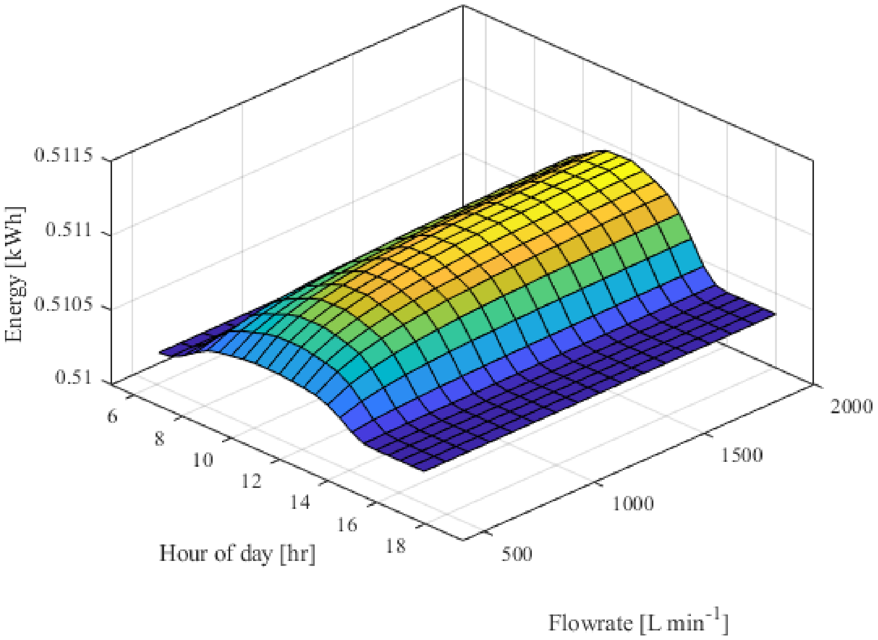

Figure 6-21 Impact of blowing duration and start-time on energy generation for a clean panel

Figure 6-20 demonstrates the simulation study of the cleaning and cooling for a soiled panel with the impact of flowrate and system start-time. To capture the most energy, releasing the air and therefore cleaning the panel is most effective when conducted earlier in the day. This gives the greatest length of time that the clean panel surface can absorb solar radiation unimpacted by dust particles. The overall difference in energy capture from the single day ranges from 0.318 – 0.429 kWh for the panel of study, depending on the time of day the air is discharged. Additionally, for the established parameters, the lowest flowrates and corresponding slower air velocities were not sufficient to remove the dust with the specified particle radius from the panel's surface. A flowrate of 800 $Lmin^{-1}$ was required to meet the detachment criteria and remove the particles from the panel surface at the 30° inclination angle. This corresponds with Figures 6-11 and 6-19 where a velocity threshold of 32 ms^{-1} is required for particle detachment, with this corresponded to flowrates in excess of 750 $Lmin^{-1}$. The power improvement arising from temperature benefits from the system are negligible compared to the cleaning benefits; the greatest energy generation from the system occurs when a flowrate of 2000 $Lmin^{-1}$ is used at the time of 7am.

A clean panel is assessed in the second scenario, presented in Figure 6-21. The increase in captured energy from the PV panel in this study only accounts for the benefits from cooling of the panel from the compressed air flow as there is initially no dust present on the panel surface. A larger amount of energy is captured when the panel is cooled during the periods where solar radiation is greater around solar noon. Additionally, a larger flowrate, corresponding to a shorter blowing duration and faster velocity air achieves a greater energy improvement, with the optimum flowrate of 2000 $Lmin^{-1}$ at 12:30pm. A greater temperature drop for a shorter duration provides the better energy benefit. The range of energy capture for the different scenarios is from 0.510 – 0.511 kWh. This is equivalent to a 0.2% improvement in power generation between the minimum and maximum obtainable values. The energy improvement from panel cooling is significantly lower than the potential energy benefit from panel cleaning. Therefore, the system should be operated with cleaning as the primary function and cooling as a possible secondary benefit if there is lack of free or surplus energy from the PV generation.

The difference in energy capture from these different scenarios of the cleaning and cooling system can be observed in Figure 6-22.

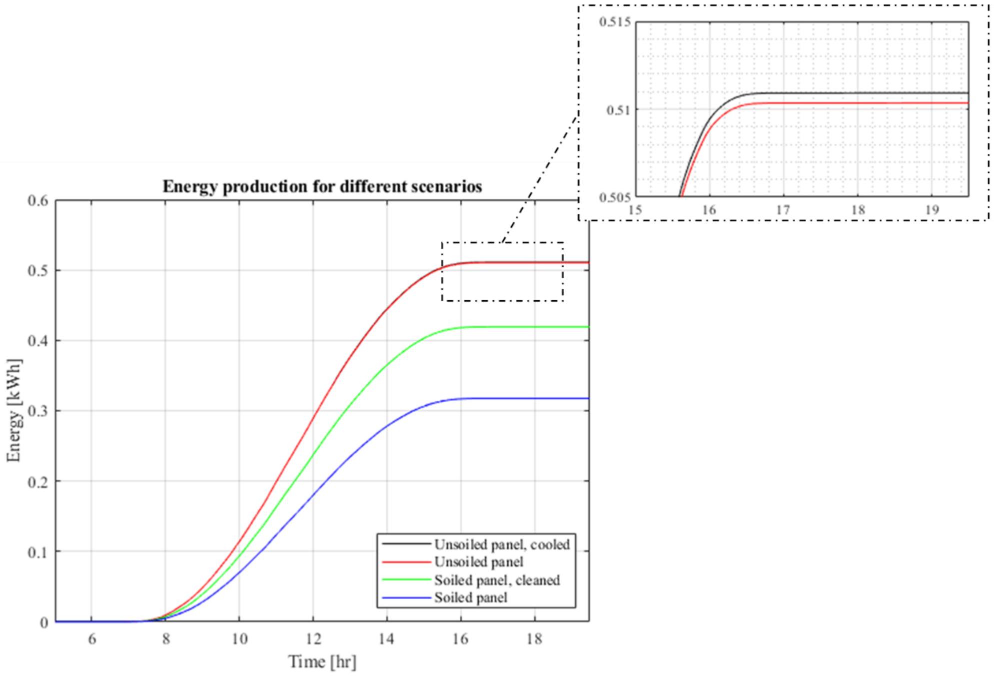

Figure 6-22. Panel energy production under different scenarios

Figure 6-22 indicates the difference in performance from the single PV panel of study under the same input solar radiation for different scenarios over a one-day period. The simulated scenarios along with the energy generated by the panel in that scenario are describe in Table 6-8:

Table 6-8. Simulated scenarios

Scenario	Energy Generation [kWh]
An unsoiled panel with discharging air	0.511
An unsoiled panel with no discharging air	0.510
An initially soiled panel, subject to discharging air	0.429
An initially soiled panel with no discharging air	0.318

The unsoiled panel subject to air discharged is cooled at the optimum time and flowrate (2000 Lmin^{-1} and 12:30pm observed from Figure 6-21) to achieve maximum energy capture. With the soiling rate is again set to 14 days equivalent as previously indicated, the initially soiled panel subject to air discharge is also operated at the optimum time and flowrate (2000 Lmin^{-1} and 7am observed from Figure 6-20). Cleaning effects from the compressed air system can be observed to be the most contributing factor to increasing energy capture, a 34.9% increase from a soiled panel. As previously stated, using the system to cool an already clean panel results in a 0.2% power improvement. Therefore, the removal of dust from the panel results in a greater improvement to energy generation than the cooling of the panel. Note, the full recovery in power performance from the cleaning system is not achieved as the cleaning factor of 55% was introduced from the soiling modelling validation work. The contribution of cleaning on the improvement in power generation is 2 orders of magnitude greater that than the potential cooling power improvement.

6.2.1 System Energy ROI

The potential power improvement from the system has been discussed, but it is advantageous to consider the benefit in terms of the return on investment of energy input to achieve the energy improvement (Energy ROI). The energy ROI, ROI_E, gives an indication of benefit in performance across a fixed period for the proposed system and is calculated with Equation (6.1).

$$ROI_E = \frac{E_{CC} - E_S}{E_{COMP}} \tag{6.1}$$

where:

ROI_E	Energy return on investment	[-]
E_{CC}	Energy production with system operation	[kWh]
E_S	Energy production without system operation	[kWh]
E_{COMP}	Compression energy	[kWh]

If the system is charged with '*free*' energy, energy that would be otherwise curtailed, then the ROI is effectively infinite. In other instances, it is worth considering the potential return as operating the system as a routine cleaning strategy.

The motor and scroll compressor model with parameters outlined in Appendix D is used to simulate the compression of air into a 200 L air tank as was discharged across the panel surface. Figure 6-23 indicates the compressor operation.

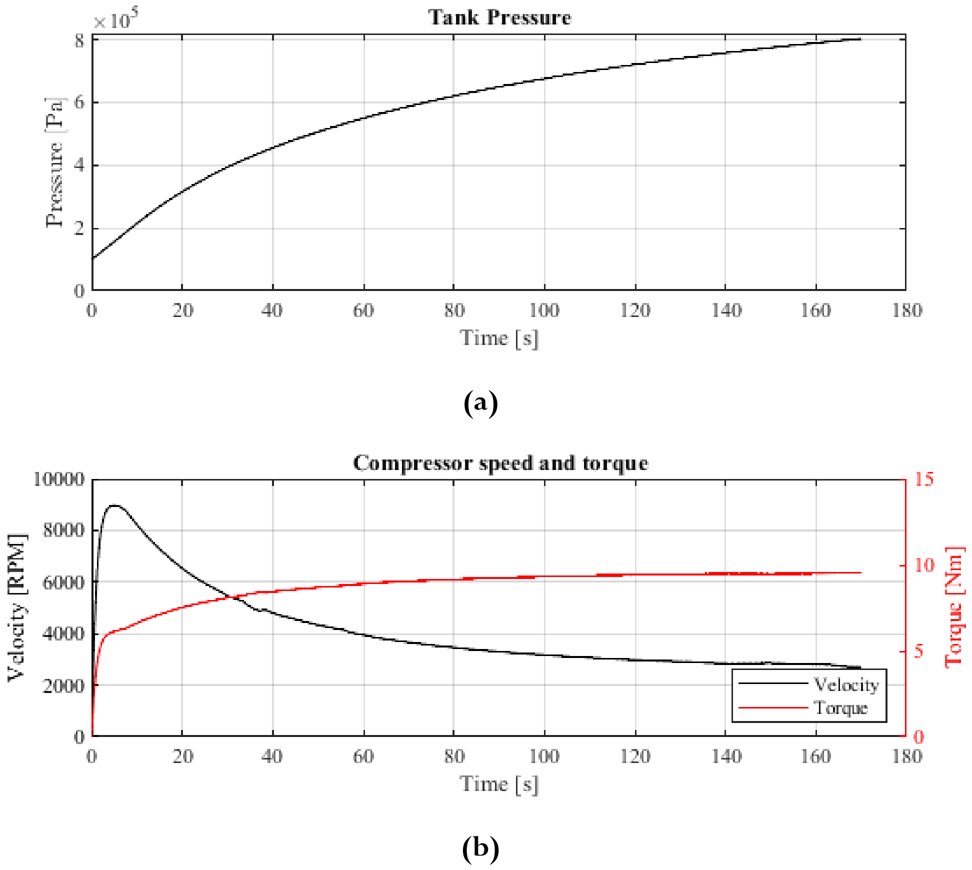

(a)

(b)

Figure 6-23. Compressor simulation characteristics

The energy required is determined from the simulated electrical energy input to the DC motor. The time period to assess the energy ROI for is chosen as 14 days, as this is mass of soiling rate that has been established; after a 14-day soiling period the panel has the same mass of dust present on the surface than prior to cleaning on the first day. A comparative uncleaned panel by the system is simulated, with the same soiling rate established. These results are displayed in Table 6-9 and Figure 6-24.

Table 6-9. Energy ROI for 14 days of PV generation

Energy, clean E_{CC} [kWh]	Energy, soiled E_S [kWh]	Energy difference [kWh]	Compressor energy E_{COMP} [kWh]	Energy ROI
4.613	3.288	1.325	0.171	7.749

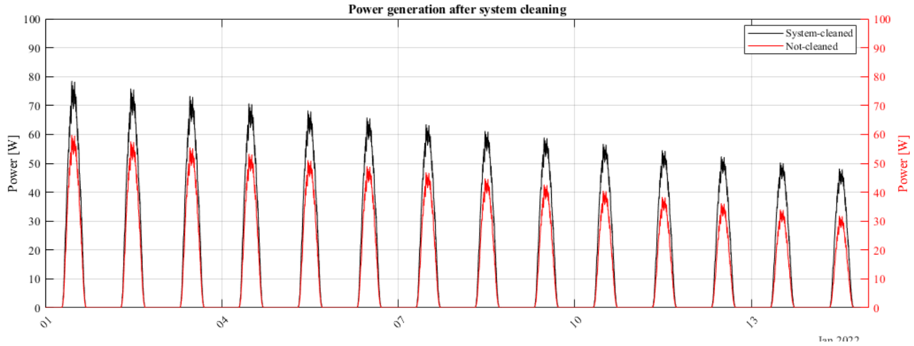

Figure 6-24. Power production across two-week period for panel cleaned and not cleaned by the system

As with the previous cases, simulation of a single air tank used to clean the panel on the first day of study. The power generation over the course of 14 days can subsequently be observed in Figure 6-24, which also displays the power generation from the panel over a 14-day period if the panel is uncleaned on the first day. The panel soiling rate was again set to 5.2 g. The difference in power generation during this time is determined. The overall power generation from the cleaned panel was 40.3% higher than that of the uncleaned. An energy ROI arising from the cleaning of the panels from the system is calculated as 7.749. This ROI is almost entirely attributable to cleaning as panel cooling is only conducted once with the air discharge on the first day of study. To provide additional efficiency improvement from cooling, the compressor would need to continuously operate, this would significantly lower the overall energy ROI because of the consumed energy driving the compressor. From the earlier analysis however, it is highly unlikely that a positive ROI can be achieved when regarding cooling effects it provides a relatively low power improvement, and the benefit arising from temperature effects are short-lasting. Implementing the cleaning strategy and achieving large ROI from cleaning demonstrates the potential for eliminating the requirement of regular manual cleaning. Additionally, variation of air pressure and store sizes would influence the energy ROI of the system. A larger air store and higher air pressures would allow for greater flowrates and blowing durations, as well as more flexible or recurring operation, but would therefore require significantly more energy to compress the air. Optimisation of the air store size and pressure therefore could be undertaken.

6.3 Summary

The dynamic mathematical model of the proposed PV-CAES system has been validated experimentally using the constructed test rig. The model has been shown to give an accurate prediction of the temperature of PV modules and their power generation, with small relative errors. Furthermore, conducted tests have validated the soiling effect model and power improvement arising from the cleaning of PV panels with the compressed air system. The general alignment and fit between the models and system measurements are satisfactory, as it is unrealistic to achieve a perfect fit to mathematical model with a large number of parameters. The validated mathematical model is used to perform a study to determine the benefit that the proposed system can provide to PV generation improvement through panel cleaning and cooling. Scenarios examining the power generation of a single PV panel have been simulated subject to different air blowing durations, speeds and start-times. It is concluded that for a heavily soiled panel, cleaning with air as early as possible in the day is advantageous for greatest energy capture. Alternatively, if the PV module is recently cleaned, the greatest benefit to the power improvement by cooling occurs when a high flowrate is used at a time when solar insolation values are most abundant. It is concluded that action of cleaning PV modules provides a greater benefit to the power production of the PV modules than the cooling effects generated by the system. Therefore, panel cooling from the compressed air system should only be considered as a secondary benefit and not a primary function for the total power improvement; however, system cooling could be advantageous in prolonging system lifetime if otherwise curtailed renewable electrical power is used as the source of the compressed air generation. The simulation results indicate an estimated 40.3% increase in power production can be achieved across a two-week period when using the system, compared to the power production of a soiled panel over the same period. The validated mathematical model is in a generic form such that continued further study can be undertaken easily.

Chapter 7 – Conclusions and Further Work

7.1 Conclusions

Arising from the impacts and future threats of global climate change, many nations are undergoing transformations in their electrical power generation networks as they are scaling back their dependence on fossil fuel-based generation. This conventional form of generation, in many cases, is being replaced by renewable power generation technologies, primarily wind and solar. These expanding variable generation technologies introduce instabilities into power networks owing to the discrepancy between immediate generation and power demand. The integration of electrical energy storage technologies (EES) into electrical grids is regarded as one of the primary solutions to this issue. The main contributions of the thesis are:

- ***The thesis has clarified underground CAES storage resources in India and the UK, addressing the storage volume requirement owing to the inherent low energy storage density of CAES systems.***

  Of the several competing EES technologies, compressed air energy storage (CAES) is one of the most mature EES technologies that excels, when compared to competing EES, in terms of range of system size, system lifetime and storage duration. The dependency of CAES on underground formations for storage is a key barrier to the adoption of the technology. A methodology for the assessment of the potential for underground compressed air energy storage and its integration with renewable energy generation is presented, with a study conducted for India. The analysis indicates that CAES is unlikely to fulfil the EES needs for India even though there is an abundance of capacity. There is little coincidence of locations that possess good renewable generation potential and that will also allow for the formation of underground storage caverns. The methodology and conclusions from the assessment provide valuable information for technology choice and policy making.

- ***The thesis proved the feasibility of a new water-free solar PV panel cleaning and cooling technology utilising CAES.***

  Photovoltaic (PV) generation faces many sources of inefficiencies. Firstly, panel soiling accounts for a large reduction in potential generation and impacts the overall lifetime of the solar modules. Second, high panel temperatures limit PV generation's electrical conversion efficiency, which is compounded by the combination of high ambient temperatures and good solar availability. Finally, owing to the intrinsic variability and uncertainty in renewable output, potential power generation is lost because of curtailment owing to the inherent variability and uncertainty in renewable generation.

A new, integrated PV-CAES mechanism is proposed as a solution to the challenges of panel soiling, heating and variability. The high-pressure air produced for the CAES system is utilised to clean and cool the PV panels by releasing air across the panel surface, with the traditional benefits of EES integration with renewable energy also realised. The proposed concept is a water-free, automatable and self-powered technology that could be applied to a wide range of PV generation scales. The research revealed the technology can achieve effective cleaning and cooling with a net solar PV system energy conversion efficiency improvement. The work provided the fundamental evidence and feasible implementation, via a laboratory scale test rig, of the proposed new technology for further commercial exploitation.

- ***The thesis presented a full-system dynamic mathematical model of the PV-CAES system and numerical simulation implementation.***

  The mathematical model and the subcomponent models of which it is comprised is validated experimentally with data acquired by the test rig and is an accurate representation of the physical system. The model is used to study particle adhesion mechanism, thermal dynamic effects on power conversion and temperature variations and the initial investigation of system setting. The model has been used to determine the benefit that the PV-CAES system could provide in terms of improving PV generation through panel cleaning and cooling. Scenarios examining the power generation of a single PV panel have been simulated subject to different air blowing durations, speeds and start-times.

- ***A laboratory scale test rig is established, and provided the essential data for model validation, system performance testing and helped to establish the potential implementation for future commercial exploitation.***

  The test rig is considered as the essential step towards proving the feasibility of the proposed system. Several new structures and configurations are proposed to best realisation of the proposed research idea. From use of the flexible test rig, the cleaning and cooling effects of airflow upon PV generation are demonstrated.

- ***The thesis has proposed an operation strategy for the proposed system based upon a system simulation study based upon real-world scenarios.***

Through the system level study and test, it is concluded that for a soiled panel, cleaning with air as early as possible in the day is advantageous for greatest energy capture. Alternatively, if the PV module is recently cleaned, the greatest benefit to the power improvement by cooling occurs when a high flowrate is used at a time when solar insolation values are most abundant. It is concluded that action of cleaning PV modules provides a greater benefit to the overall power production of the PV modules than the cooling effects generated by the system. The conducted system performance analysis indicates that the additional power generation from the cleaned PV, is greater than the power requirement for the compression of the air so a positive energy return on investment can be achieved.

Overall, the concept of the integrated PV-CAES system for efficiency improvement through panel cleaning and cooling has been proven, with efficiency gains to PV generation achieved through both cleaning and cooling mechanisms. However, power improvement from system cooling effects alone are small, and it is unlikely to be feasible as a method for PV panel temperature regulation. This notwithstanding, the use of high-pressure air to clean PV modules shows promise as an automatable strategy for soiling mitigation.

7.2 Further Work

Aspects of the research presented in this thesis could benefit from additional work. The constructed test rig was intentionally designed to be flexible and modular such that many additional experiments can be performed. Optimisation of the nozzle mechanism, e.g. number, position, angle, etc. would be the most valuable future experimental activity, as in this study a sole nozzle arrangement was implemented for experimentation and model validation. It is expected that different nozzle arrangements will have different cooling and cleaning benefits relative to their air consumption.

With the full-system model of the PV-CAES system established, there are several future activities of interest. Refinements to the mathematical model, with the consideration of the velocity profile of the air across the panel. In this study, uniform air velocity and cleaning is assumed; thus, this can be enhanced with additional consideration of air behaviour. Furthermore, the current model assumes a uniform particle size distribution resulting in a uniform removal of the particles modified by the experimentally determined cleaning factor; to enhance the accuracy of the model, a distribution in particle size and density on the panel surface could be adopted. Thus, different size particles would require different velocities to detach, thus different power improvement from cleaning would be observed. Additionally, different cooling and cleaning strategies can be investigated. For the analysis contained within this thesis, a single fixed volume of compressed air at a constant starting pressure was assumed, and the best power improvement from this scenario was determined. The mathematical model can be used to determine the optimum size of components with regard to compressed air volume, installed PV capacity, etc., and the long-term operation of such a system must also be considered, as a single clear day is examined in this study. For the long-term operation of PV arrays, the frequency and time of the regulation could be optimised considering the variation of solar radiation and load demand, and weather conditions etc., to achieve more energy benefit, from this economic analysis could be conducted, which would provide great insights into potential commercialisation of the concept.

References

[1] U.S. Global Change Research Program. Climate science special report: Fourth national climate assessment, volume I. US Global Change Research Program 2018;1:470. https://doi.org/10.7930/J0J964J6.

[2] US EPA. Sources of Greenhouse Gas Emissions 2022. https://www.epa.gov/ghgemissions/sources-greenhouse-gas-emissions (accessed May 27, 2022).

[3] Department for Business E& IS. 2020 UK Greenhouse Gas Emissions, Final Figures. n.d.

[4] Emissions – Global Energy & CO2 Status Report 2019 – Analysis - IEA n.d. https://www.iea.org/reports/global-energy-co2-status-report-2019/emissions (accessed May 27, 2022).

[5] United Nations Framework Convention on Climate Change (UNFCCC). Paris Agreement 2015.

[6] SolarPower Europe. Global Market Outlook For Solar Power 2021 - 2025. 2021.

[7] Mithhu MMH, Rima TA, Khan MR. Global analysis of optimal cleaning cycle and profit of soiling affected solar panels. Applied Energy 2021;285:116436. https://doi.org/10.1016/J.APENERGY.2021.116436.

[8] King M, Jain A, Bhakar R, Mathur J, Wang J. Overview of current compressed air energy storage projects and analysis of the potential underground storage capacity in India and the UK. Renewable and Sustainable Energy Reviews 2021;139:110705. https://doi.org/10.1016/J.RSER.2021.110705.

[9] Geth F, Brijs T, Kathan J, Driesen J, Belmans R. An overview of large-scale stationary electricity storage plants in Europe: Current status and new developments. Renewable and Sustainable Energy Reviews 2015;52:1212–27. https://doi.org/10.1016/J.RSER.2015.07.145.

[10] Department of Energy (DOE) Global Energy Storage Database 2021. https://sandia.gov/ess-ssl/gesdb/public/projects.html (accessed January 31, 2022).

[11] Barbour E, Wilson IAG, Radcliffe J, Ding Y, Li Y. A review of pumped hydro energy storage development in significant international electricity markets. Renewable and Sustainable Energy Reviews 2016;61:421–32. https://doi.org/10.1016/J.RSER.2016.04.019.

[12] Crotogino F, Mohmeyer KU, Scharf R. Huntorf CAES: More than 20 Years of Successful Operation. 2001.

[13] Luo X, Wang J, Dooner M, Clarke J. Overview of current development in electrical energy storage technologies and the application potential in power system

operation. Applied Energy 2015;137:511–36. https://doi.org/10.1016/J.APENERGY.2014.09.081.

[14] Barbour E. Adiabatic Compressed Air Energy Storage n.d. http://www.eseslab.com/research-CAES (accessed February 2, 2022).

[15] Guess M. How compressed-air storage could give renewable energy a boost. Ars Technica 2019. https://arstechnica.com/science/2019/01/how-compressed-air-storage-could-give-renewable-energy-a-boost/ (accessed February 2, 2022).

[16] Budt M, Wolf D, Span R, Yan J. A review on compressed air energy storage: Basic principles, past milestones and recent developments. Applied Energy 2016;170:250–68. https://doi.org/10.1016/J.APENERGY.2016.02.108.

[17] Liu W, Liu L, Zhou L, Huang J, Zhang Y, Xu G, et al. Analysis and Optimization of a Compressed Air Energy Storage—Combined Cycle System. Entropy 2014, Vol 16, Pages 3103-3120 2014;16:3103–20. https://doi.org/10.3390/E16063103.

[18] Chen H, Cong TN, Yang W, Tan C, Li Y, Ding Y. Progress in electrical energy storage system: A critical review. Progress in Natural Science 2009;19:291–312. https://doi.org/10.1016/J.PNSC.2008.07.014.

[19] Albawab M, Ghenai C, Bettayeb M, Janajreh I. Sustainability Performance Index for Ranking Energy Storage Technologies using Multi-Criteria Decision-Making Model and Hybrid Computational Method. Journal of Energy Storage 2020;32:101820. https://doi.org/10.1016/J.EST.2020.101820.

[20] Mongird K, Viswanathan V, Balducci P, Alam J, Fotedar V, Koritarov V, et al. An Evaluation of Energy Storage Cost and Performance Characteristics. Energies 2020, Vol 13, Page 3307 2020;13:3307. https://doi.org/10.3390/EN13133307.

[21] Jannelli E, Minutillo M, Lubrano Lavadera A, Falcucci G. A small-scale CAES (compressed air energy storage) system for stand-alone renewable energy power plant for a radio base station: A sizing-design methodology. Energy 2014;78:313–22. https://doi.org/10.1016/J.ENERGY.2014.10.016.

[22] Donadei S, Schneider GS. Compressed Air Energy Storage in Underground Formations. Storing Energy: With Special Reference to Renewable Energy Sources 2016:113–33. https://doi.org/10.1016/B978-0-12-803440-8.00006-3.

[23] He W, Wang J. Optimal selection of air expansion machine in Compressed Air Energy Storage: A review. Renewable and Sustainable Energy Reviews 2018;87:77–95. https://doi.org/10.1016/J.RSER.2018.01.013.

[24] He Y, Chen H, Xu Y, Deng J. Compression performance optimization considering variable charge pressure in an adiabatic compressed air energy storage system. Energy 2018;165:349–59. https://doi.org/10.1016/J.ENERGY.2018.09.168.

[25] Zhou Q, Du D, Lu C, He Q, Liu W. A review of thermal energy storage in compressed air energy storage system. Energy 2019;188:115993. https://doi.org/10.1016/J.ENERGY.2019.115993.

[26] Olabi AG, Wilberforce T, Ramadan M, Abdelkareem MA, Alami AH. Compressed air energy storage systems: Components and operating parameters – A review. Journal of Energy Storage 2021;34:102000. https://doi.org/10.1016/J.EST.2020.102000.

[27] Koohi-Fayegh S, Rosen MA. A review of energy storage types, applications and recent developments. Journal of Energy Storage 2020;27:101047. https://doi.org/10.1016/J.EST.2019.101047.

[28] Weiqing X, Ziyue D, Xiaoshuang W, Maolin C, Guanwei J, Yan S. Isothermal piston gas compression for compressed air energy storage. International Journal of Heat and Mass Transfer 2020;155:119779. https://doi.org/10.1016/J.IJHEATMASSTRANSFER.2020.119779.

[29] Chen H, Peng Y hang, Wang Y ling, Zhang J. Thermodynamic analysis of an open type isothermal compressed air energy storage system based on hydraulic pump/turbine and spray cooling. Energy Conversion and Management 2020;204:112293. https://doi.org/10.1016/J.ENCONMAN.2019.112293.

[30] Odukomaiya A, Kokou E, Hussein Z, Abu-Heiba A, Graham S, Momen AM. Near-isothermal-isobaric compressed gas energy storage. Journal of Energy Storage 2017;12:276–87. https://doi.org/10.1016/J.EST.2017.05.014.

[31] ARES North America. Our Company 2022. https://aresnorthamerica.com/our-company/ (accessed February 2, 2022).

[32] Gravity Energy Storage Technology | Energy Vault 2021. https://www.energyvault.com/gravity (accessed February 2, 2022).

[33] Projects - Renewable energy storage | Gravitricity projects n.d. https://gravitricity.com/projects/ (accessed February 2, 2022).

[34] Li X, Palazzolo A. A review of flywheel energy storage systems: state of the art and opportunities. Journal of Energy Storage 2022;46:103576. https://doi.org/10.1016/J.EST.2021.103576.

[35] Mousavi G SM, Faraji F, Majazi A, Al-Haddad K. A comprehensive review of Flywheel Energy Storage System technology. Renewable and Sustainable Energy Reviews 2017;67:477–90. https://doi.org/10.1016/J.RSER.2016.09.060.

[36] Robson P, Bonomi D, Research D. Growing The Battery Storage Market 2020. 2020.

[37] Díaz-González F, Sumper A, Gomis-Bellmunt O, Villafáfila-Robles R. A review of energy storage technologies for wind power applications. Renewable and

Sustainable Energy Reviews 2012;16:2154–71. https://doi.org/10.1016/J.RSER.2012.01.029.

[38] Hornsdale Power Reserve | South Australia's Big Battery n.d. https://hornsdalepowerreserve.com.au/ (accessed February 2, 2022).

[39] Expansion complete at world's biggest battery storage system in California - Energy Storage News 2021. https://www.energy-storage.news/expansion-complete-at-worlds-biggest-battery-storage-system-in-california/ (accessed February 2, 2022).

[40] Yilmaz M, Krein PT. Review of the impact of vehicle-to-grid technologies on distribution systems and utility interfaces. IEEE Transactions on Power Electronics 2013;28:5673–89. https://doi.org/10.1109/TPEL.2012.2227500.

[41] Leung P, Shah AA, Sanz L, Flox C, Morante JR, Xu Q, et al. Recent developments in organic redox flow batteries: A critical review. Journal of Power Sources 2017;360:243–83. https://doi.org/10.1016/J.JPOWSOUR.2017.05.057.

[42] Mayyas A, Wei M, Levis G. Hydrogen as a long-term, large-scale energy storage solution when coupled with renewable energy sources or grids with dynamic electricity pricing schemes. International Journal of Hydrogen Energy 2020;45:16311–25. https://doi.org/10.1016/J.IJHYDENE.2020.04.163.

[43] Mekhilef S, Saidur R, Safari A. Comparative study of different fuel cell technologies. Renewable and Sustainable Energy Reviews 2012;16:981–9. https://doi.org/10.1016/J.RSER.2011.09.020.

[44] Bailera M, Lisbona P, Romeo LM, Espatolero S. Power to Gas projects review: Lab, pilot and demo plants for storing renewable energy and CO2. Renewable and Sustainable Energy Reviews 2017;69:292–312. https://doi.org/10.1016/J.RSER.2016.11.130.

[45] He W, King M, Luo X, Dooner M, Li D, Wang J. Technologies and economics of electric energy storages in power systems: Review and perspective. Advances in Applied Energy 2021;4:100060. https://doi.org/10.1016/j.adapen.2021.100060.

[46] Rahman MM, Oni AO, Gemechu E, Kumar A. Assessment of energy storage technologies: A review. Energy Conversion and Management 2020;223:113295. https://doi.org/10.1016/J.ENCONMAN.2020.113295.

[47] Gür TM. Review of electrical energy storage technologies, materials and systems: challenges and prospects for large-scale grid storage. Energy & Environmental Science 2018;11:2696–767. https://doi.org/10.1039/C8EE01419A.

[48] Succar S, Williams RH. Compressed Air Energy Storage: Theory, Resources And Applications for Wind Power. 2008.

[49] Cassell B. Ohio board revokes approval for 2,700-MW compressed air project | Transmission Intelligence Service. Transmission Hub 2013.

https://www.transmissionhub.com/articles/2013/10/ohio-board-revokes-approval-for-2700-mw-compressed-air-project.html (accessed March 22, 2022).

[50] Rettberg J. Seneca Advanced Compressed Air Energy Storage (CAES) 150 MW Plant Using an Existing Salt Cavern 2010.

[51] NETL. Seneca Compressed Air Energy Storage (CAES) Project: Final Phase 1 Technical Report. 2012.

[52] Wang J, Lu K, Ma L, Wang J, Dooner M, Miao S, et al. Overview of Compressed Air Energy Storage and Technology Development. Energies 2017, Vol 10, Page 991 2017;10:991. https://doi.org/10.3390/EN10070991.

[53] Bethel Energy Center | APEX CAES. Apex CAES 2022. http://www.apexcaes.com/bethel-energy-center (accessed March 1, 2022).

[54] Discover renewable energy technology with compressed air energy storage. PG&E 2022. https://www.pge.com/en_US/about-pge/environment/what-we-are-doing/compressed-air-energy-storage/compressed-air-energy-storage.page (accessed March 1, 2022).

[55] Medeiros M, Booth R, Fairchild J, Imperato D, Stinson C, Ausburn M, et al. Technical Feasibility of Compressed Air Energy Storage (CAES) Utilizing a Porous Rock Reservoir 2018. https://doi.org/10.2172/1434251.

[56] Goderich Energy Storage Facility 2022. https://www.hydrostor.ca/goderich-a-caes-facility/ (accessed March 1, 2022).

[57] Spence A. Canadians pull plug on Strathalbyn energy storage project 2021. https://indaily.com.au/news/2021/01/21/canadians-pull-plug-on-strathalbyn-energy-storage-project/ (accessed March 22, 2022).

[58] Bollinger B. Demonstration of Isothermal Compressed Air Energy Storage to Support Renewable Energy Production 2015. https://doi.org/10.2172/1178542.

[59] st. John J. SustainX to Merge With General Compression, Abandon Above-Ground CAES Ambitions | Greentech Media 2015. https://www.greentechmedia.com/articles/read/sustainx-to-merge-with-general-compression-abandon-above-ground-caes-ambiti (accessed March 1, 2022).

[60] Geissbühler L, Becattini V, Zanganeh G, Zavattoni S, Barbato M, Haselbacher A, et al. Pilot-scale demonstration of advanced adiabatic compressed air energy storage, Part 1: Plant description and tests with sensible thermal-energy storage. Journal of Energy Storage 2018;17:129–39. https://doi.org/10.1016/J.EST.2018.02.004.

[61] Becattini V, Geissbühler L, Zanganeh G, Haselbacher A, Steinfeld A. Pilot-scale demonstration of advanced adiabatic compressed air energy storage, Part 2: Tests with combined sensible/latent thermal-energy storage. Journal of Energy Storage 2018;17:140–52. https://doi.org/10.1016/J.EST.2018.02.003.

[62] ALACAES n.d. https://alacaes.com/ (accessed March 1, 2022).

[63] Construction Begins on "Salt Cave Compressed Air Energy Storage National Test and Demonstration Project" — China Energy Storage Alliance 2020. https://en.cnesa.org/new-blog/2020/9/26/construction-begins-on-salt-cave-compressed-air-energy-storage-national-test-and-demonstration-project-c7mcp (accessed March 1, 2022).

[64] Xu Y. Design of non-supplemental combustion compressed air energy storage system based on STAR-90 simulation. AIP Conference Proceedings 2019;2066:020051. https://doi.org/10.1063/1.5089093.

[65] Compressed Air Energy Storage: The Path to Innovation — China Energy Storage Alliance. 2019 n.d. https://en.cnesa.org/latest-news/2019/9/29/compressed-air-energy-storage-becoming-a-leading-energy-storage-technology (accessed March 1, 2022).

[66] Luo X, Wang J, Dooner M, Clarke J, Krupke C. Overview of Current Development in Compressed Air Energy Storage Technology. Energy Procedia 2014;62:603–11. https://doi.org/10.1016/J.EGYPRO.2014.12.423.

[67] New Power. NI compressed-air energy storage application withdrawn | New Power 2019. https://www.newpower.info/2019/08/ni-compressed-air-storage-application-withdrawn/ (accessed March 1, 2022).

[68] RWE Power. ADELE - Adiabatic Compressed-Air Energy Storage For Electricity Supply. 2010.

[69] Chen L, Zheng T, Mei S, Xue X, Liu B, Lu Q. Review and prospect of compressed air energy storage system. Journal of Modern Power Systems and Clean Energy 2016;4:529–41. https://doi.org/10.1007/S40565-016-0240-5/FIGURES/5.

[70] China Energy Storage Network News Center. Gezhouba 50MW/300MWh Compressed Air Energy Storage Power Station is included in the list of major projects in Shandong Province 2020. http://escn.com.cn/news/show-809293.html (accessed March 1, 2022).

[71] O'Meara S, Ye Y. Four Research Teams Powering China's Net-Zero Energy Goal. Nature 2022;603:S41–3.

[72] Matos CR, Carneiro JF, Silva PP. Overview of Large-Scale Underground Energy Storage Technologies for Integration of Renewable Energies and Criteria for Reservoir Identification. Journal of Energy Storage 2019;21:241–58. https://doi.org/10.1016/J.EST.2018.11.023.

[73] Adavale Basin Salt Cavern Storage Potential - Innovative Energy … n.d. https://www.yumpu.com/en/document/read/39912073/adavale-basin-salt-cavern-storage-potential-innovative-energy- (accessed March 1, 2022).

[74] Evans DJ, Reay DM, Riley NJ, Mitchell WI, Busby J. Appraisal of underground energy storage potential in Northern Ireland. 2006.

[75] Crotogino F, Schneider G-S, Evans DJ. Renewable energy storage in geological formations. Journal of Power and Energy 2017;232:100–14. https://doi.org/10.1177/0957650917731181.

[76] Donadei S, Schneider GS. Compressed Air Energy Storage in Underground Formations. Storing Energy: With Special Reference to Renewable Energy Sources 2016:113–33. https://doi.org/10.1016/B978-0-12-803440-8.00006-3.

[77] Blanco H, Faaij A. A review at the role of storage in energy systems with a focus on Power to Gas and long-term storage. Renewable and Sustainable Energy Reviews 2018;81:1049–86. https://doi.org/10.1016/J.RSER.2017.07.062.

[78] Beckingham LE, Winningham L. Critical Knowledge Gaps for Understanding Water–Rock–Working Phase Interactions for Compressed Energy Storage in Porous Formations. ACS Sustainable Chemistry & Engineering 2019;8:2–11. https://doi.org/10.1021/ACSSUSCHEMENG.9B05388.

[79] Federal Energy Regulatory Commission. Current State of and Issues Concerning Underground Natural Gas Storage. 2004.

[80] Li Y, Liu Y, Hu B, Dong J. Numerical investigation of a novel approach to coupling compressed air energy storage in aquifers with geothermal energy. Applied Energy 2020;279:115781. https://doi.org/10.1016/J.APENERGY.2020.115781.

[81] Mansson L, Marion P. The LRC concept and the demonstration plant in Sweden - A new approach to commerical gas storage. 2003.

[82] Foley A, Díaz Lobera I. Impacts of compressed air energy storage plant on an electricity market with a large renewable energy portfolio. Energy 2013;57:85–94. https://doi.org/10.1016/J.ENERGY.2013.04.031.

[83] Jiang Z, Li P, Tang D, Zhao H, Li Y. Experimental and Numerical Investigations of Small-Scale Lined Rock Cavern at Shallow Depth for Compressed Air Energy Storage. Rock Mechanics and Rock Engineering 2020;53:2671–83. https://doi.org/10.1007/S00603-019-02009-X/FIGURES/22.

[84] Barnes FS, Levine JG. Large Energy Storage Systems Handbook. Taylor and Fracis Group, LLC; 2011.

[85] Zhou S, Xia C, Zhou Y. Long-term stability of a lined rock cavernfor compressed air energy storage: thermo-mechanical damage modeling. European Journal of Environmental and Civil Engineering 2018;24:2070–93. https://doi.org/10.1080/19648189.2018.1499556.

[86] Cătuţi M, Egenhofer C, Elkerbout M. The future of gas in Europe: Review of recent studies on the future of gas. 2019.

[87] Menéndez J, Ordóñez A, Álvarez R, Loredo J. Energy from closed mines: Underground energy storage and geothermal applications. Renewable and Sustainable Energy Reviews 2019;108:498–512. https://doi.org/10.1016/J.RSER.2019.04.007.

[88] Infrastructure Partnerships Australia. Broken Hill Energy Storage 2020. https://infrastructurepipeline.org/project/broken-hill-energy-storage (accessed March 22, 2022).

[89] Schmidt F, Menéndez J, Konietzky H, Pascual-Muñoz P, Castro J, Loredo J, et al. Converting closed mines into giant batteries: Effects of cyclic loading on the geomechanical performance of underground compressed air energy storage systems. Journal of Energy Storage 2020;32:101882. https://doi.org/10.1016/J.EST.2020.101882.

[90] Department of Economic and Social Affairs. World Population Prospects 2019 Highlights. New York: 2019.

[91] Ali S. The Future of Indian Electricity Demand: How much, by whom, and under what conditions? 2018.

[92] Ministry of New and Renewable Energy. Annual Report 18-19. 2019.

[93] Department for Business Energy and Industrial Strategy, Skidmore C. UK becomes first major economy to pass net zero emissions law 2019. https://www.gov.uk/government/news/uk-becomes-first-major-economy-to-pass-net-zero-emissions-law (accessed May 27, 2022).

[94] Tong Z, Cheng Z, Tong S. A review on the development of compressed air energy storage in China: Technical and economic challenges to commercialization. Renewable and Sustainable Energy Reviews 2021;135:110178. https://doi.org/10.1016/J.RSER.2020.110178.

[95] Li L, Liang W, Lian H, Yang J, Dusseault M. Compressed air energy storage: Characteristics, basic principles, and geological considerations. Advances in Geo-Energy Research 2018;2:135–47. https://doi.org/10.26804/ager.2018.02.03.

[96] Parkes D, Evans DJ, Williamson P, Williams JDO. Estimating available salt volume for potential CAES development: A case study using the Northwich Halite of the Cheshire Basin. Journal of Energy Storage 2018;18:50–61. https://doi.org/10.1016/J.EST.2018.04.019.

[97] Aghahosseini A, Breyer C. Assessment of geological resource potential for compressed air energy storage in global electricity supply. Energy Conversion and Management 2018;169:161–73. https://doi.org/10.1016/J.ENCONMAN.2018.05.058.

[98] Hartmann J, Moosdorf N, Hartmann J, Moosdorf N. The new global lithological map database GLiM: A representation of rock properties at the Earth surface.

Geochemistry, Geophysics, Geosystems 2012;13:12004. https://doi.org/10.1029/2012GC004370.

[99] Geological Survey of India. Map Series 2022. https://www.gsi.gov.in/webcenter/portal/OCBIS/pageMAPS/pageMapsSeries?_afrLoop=46237738486047968&_adf.ctrl-state=l7ze2iksi_35#!%40%40%3F_afrLoop%3D46237738486047968%26_adf.ctrl-state%3Dl7ze2iksi_39 (accessed March 1, 2022).

[100] World-wide Hydrogeological Mapping and Assessment Programme. Large Aquifers. UNESCO 2022. https://www.whymap.org/whymap/EN/Maps_Data/Additional_maps/whymap_largeaquifers_g.html (accessed June 5, 2022).

[101] Renewables.ninja 2022. https://www.renewables.ninja/ (accessed March 1, 2022).

[102] Vikram solar. Solivo smart: Grand ultima series. Data Sheet n.d.;VSL/ENG/SC/186.

[103] Solar Radiation Data. SoDa 2022. https://www.soda-pro.com/web-services (accessed March 1, 2022).

[104] Suzlon. S111. Data Sheet 2022.

[105] He W, Luo X, Evans D, Busby J, Garvey S, Parkes D, et al. Exergy storage of compressed air in cavern and cavern volume estimation of the large-scale compressed air energy storage system. Applied Energy 2017;208:745–57. https://doi.org/10.1016/J.APENERGY.2017.09.074.

[106] Tiewsoh LS, Jirásek J, Sivek M. Electricity Generation in India: Present State, Future Outlook and Policy Implications. Energies 2019, Vol 12, Page 1361 2019;12:1361. https://doi.org/10.3390/EN12071361.

[107] Jain A, Das P, Yamujala S, Bhakar R, Mathur J. Resource potential and variability assessment of solar and wind energy in India. Energy 2020;211:118993. https://doi.org/10.1016/J.ENERGY.2020.118993.

[108] He W, Dooner M, King M, Li D, Guo S, Wang J. Techno-economic analysis of bulk-scale compressed air energy storage in power system decarbonisation. Applied Energy 2021;282:116097. https://doi.org/10.1016/J.APENERGY.2020.116097.

[109] Dooner M, Wang J. Potential Exergy Storage Capacity of Salt Caverns in the Cheshire Basin Using Adiabatic Compressed Air Energy Storage. Entropy 2019, Vol 21, Page 1065 2019;21:1065. https://doi.org/10.3390/E21111065.

[110] Mouli-Castillo J, Wilkinson M, Mignard D, McDermott C, Haszeldine RS, Shipton ZK. Inter-seasonal compressed-air energy storage using saline aquifers. Nature Energy 2019 4:2 2019;4:131–9. https://doi.org/10.1038/s41560-018-0311-0.

[111] British Geological Survey. Mineral Planning Factsheet: Underground Storage. 2008.

[112] Wolfe PR. The Solar Generation: Childhood and Adolescence of Terrestrial Photovoltaics. Wiley-IEEE Press; 2018.

[113] Breeze P. An Introduction to Solar Power. Solar Power Generation, Elsevier; 2016, p. 1–8. https://doi.org/10.1016/B978-0-12-804004-1.00001-4.

[114] IEA. Solar PV – Analysis - IEA 2021. https://www.iea.org/reports/solar-pv (accessed February 6, 2022).

[115] International Energy Agency (IEA). Renewable Energy Market Update - Outlook for 2021 and 2022. 2021.

[116] World Energy Council. World Energy Scenarios: Composing energy futures to 2050. 2013.

[117] Yang J, Yuan X, Ji L. Solar Photovoltaic Power Generation. De Gruyter; 2020. https://doi.org/10.1515/9783110524833.

[118] International Energy Agency (IEA). Concentrated Solar Power (CSP) 2021. https://www.iea.org/reports/concentrated-solar-power-csp (accessed January 24, 2022).

[119] Rathore N, Panwar NL, Yettou F, Gama A. A comprehensive review of different types of solar photovoltaic cells and their applications. International Journal of Ambient Energy 2019;42:1200–17. https://doi.org/10.1080/01430750.2019.1592774.

[120] Kalogirou SA. Photovoltaic Systems. Solar Energy Engineering, Elsevier; 2014, p. 481–540. https://doi.org/10.1016/B978-0-12-397270-5.00009-1.

[121] Wilson GM, Al-Jassim M, Metzger WK, Glunz SW, Verlinden P, Xiong G, et al. The 2020 photovoltaic technologies roadmap. Journal of Physics D: Applied Physics 2020;53:493001. https://doi.org/10.1088/1361-6463/AB9C6A.

[122] O'Shaughnessy E, Cruce JR, Xu K. Too much of a good thing? Global trends in the curtailment of solar PV. Solar Energy 2020;208:1068. https://doi.org/10.1016/J.SOLENER.2020.08.075.

[123] Statista. Solar photovoltaic power curtailment rate in China from 2014 to 2020 2021. https://www.statista.com/statistics/973698/china-pv-power-curtailment-rate/ (accessed February 5, 2022).

[124] Kim D, Kim H, Won D. Operation strategy of shared ESS based on power sensitivity analysis to minimize PV curtailment and maximize profit. IEEE Access 2020;8:197097–110. https://doi.org/10.1109/ACCESS.2020.3034339.

[125] Bird L, Lew D, Milligan M, Carlini EM, Estanqueiro A, Flynn D, et al. Wind and solar energy curtailment: A review of international experience. Renewable and

Sustainable Energy Reviews 2016;65:577–86. https://doi.org/10.1016/J.RSER.2016.06.082.

[126] Ilse KK, Figgis BW, Naumann V, Hagendorf C, Bagdahn J. Fundamentals of soiling processes on photovoltaic modules. Renewable and Sustainable Energy Reviews 2018;98:239–54. https://doi.org/10.1016/J.RSER.2018.09.015.

[127] Sayyah A, Horenstein MN, Mazumder MK. Energy yield loss caused by dust deposition on photovoltaic panels. Solar Energy 2014;107:576–604. https://doi.org/10.1016/J.SOLENER.2014.05.030.

[128] Ilse K, Micheli L, Figgis BW, Lange K, Daßler D, Hanifi H, et al. Techno-Economic Assessment of Soiling Losses and Mitigation Strategies for Solar Power Generation. Joule 2019;3:2303–21. https://doi.org/10.1016/J.JOULE.2019.08.019.

[129] Bergin MH, Ghoroi C, Dixit D, Schauer JJ, Shindell DT. Large Reductions in Solar Energy Production Due to Dust and Particulate Air Pollution. Environmental Science and Technology Letters 2017;4:339–44. https://doi.org/10.1021/ACS.ESTLETT.7B00197/SUPPL_FILE/EZ7B00197_SI_001.PDF.

[130] Appels R, Lefevre B, Herteleer B, Goverde H, Beerten A, Paesen R, et al. Effect of soiling on photovoltaic modules. Solar Energy 2013;96:283–91. https://doi.org/10.1016/J.SOLENER.2013.07.017.

[131] Ovrum O, Marchetti JM, Kelesoglu S, Marstein ES. Comparative Analysis of Site-Specific Soiling Losses on PV Power Production. IEEE Journal of Photovoltaics 2021;11:158–63. https://doi.org/10.1109/JPHOTOV.2020.3032906.

[132] Mayhoub M. Cleaning innovative daylighting systems: Review and suggested methods. Lighting Research and Technology 2017;49:1015–33. https://doi.org/10.1177/1477153516669969.

[133] Klugmann-Radziemska E, Rudnicka M. Decrease in Photovoltaic Module Efficiency because of the Deposition of Pollutants. IEEE Journal of Photovoltaics 2020;10:1772–9. https://doi.org/10.1109/JPHOTOV.2020.3013971.

[134] Sarver T, Al-Qaraghuli A, Kazmerski LL. A comprehensive review of the impact of dust on the use of solar energy: History, investigations, results, literature, and mitigation approaches. Renewable and Sustainable Energy Reviews 2013;22:698–733. https://doi.org/10.1016/J.RSER.2012.12.065.

[135] Tanesab J, Parlevliet D, Whale J, Urmee T, Pryor T. The contribution of dust to performance degradation of PV modules in a temperate climate zone. Solar Energy 2015;120:147–57. https://doi.org/10.1016/J.SOLENER.2015.06.052.

[136] Schill C, Brachmann S, Koehl M. Impact of soiling on IV-curves and efficiency of PV-modules. Solar Energy 2015;112:259–62. https://doi.org/10.1016/J.SOLENER.2014.12.003.

[137] Zeedan A, Barakeh A, Al-Fakhroo K, Touati F, Gonzales ASP. Quantification of PV Power and Economic Losses Due to Soiling in Qatar. Sustainability 2021, Vol 13, Page 3364 2021;13:3364. https://doi.org/10.3390/SU13063364.

[138] Javed W, Guo B, Figgis B, Aïssa B. Dust potency in the context of solar photovoltaic (PV) soiling loss. Solar Energy 2021;220:1040–52. https://doi.org/10.1016/J.SOLENER.2021.04.015.

[139] Younis A, Alhorr Y. Modeling of dust soiling effects on solar photovoltaic performance: A review. Solar Energy 2021;220:1074–88. https://doi.org/10.1016/J.SOLENER.2021.04.011.

[140] Gupta V, Sharma M, Pachauri RK, Dinesh Babu KN. Comprehensive review on effect of dust on solar photovoltaic system and mitigation techniques. Solar Energy 2019;191:596–622. https://doi.org/10.1016/J.SOLENER.2019.08.079.

[141] Chiteka K, Arora R, Sridhara SN, Enweremadu CC. A novel approach to Solar PV cleaning frequency optimization for soiling mitigation. Sci Afr 2020;8:e00459. https://doi.org/10.1016/J.SCIAF.2020.E00459.

[142] Bessa JG, Micheli L, Almonacid F, Fernández EF. Monitoring photovoltaic soiling: assessment, challenges, and perspectives of current and potential strategies. IScience 2021;24:102165. https://doi.org/10.1016/J.ISCI.2021.102165.

[143] Hanifi H, Khan MZ, Jaeckel B, Hagendorf C, Schneider J, Abdallah A, et al. Optimum PV module interconnection layout and mounting orientation to reduce inhomogeneous soiling losses in desert environments. Solar Energy 2020;203:267–74. https://doi.org/10.1016/J.SOLENER.2020.04.025.

[144] Maghami MR, Hizam H, Gomes C, Radzi MA, Rezadad MI, Hajighorbani S. Power loss due to soiling on solar panel: A review. Renewable and Sustainable Energy Reviews 2016;59:1307–16. https://doi.org/10.1016/J.RSER.2016.01.044.

[145] Olalla C, Nazmul Hasan M, Deline C, Maksimovi D. Mitigation of Hot-Spots in Photovoltaic Systems Using Distributed Power Electronics 2018. https://doi.org/10.3390/en11040726.

[146] Hajjaj C, Bouaichi A, Zitouni H, Alami Merrouni A, Ghennioui A, Ikken B, et al. Degradation and performance analysis of a monocrystalline PV system without EVA encapsulating in semi-arid climate. Heliyon 2020;6:e04079. https://doi.org/10.1016/J.HELIYON.2020.E04079.

[147] Song Z, Liu J, Yang H. Air pollution and soiling implications for solar photovoltaic power generation: A comprehensive review. Applied Energy 2021;298:117247. https://doi.org/10.1016/J.APENERGY.2021.117247.

[148] Miller DC, Alnuaimi A, John JJ, Simpson LJ, Engtrakul C, Einhorn A, et al. The Abrasion of Photovoltaic Glass: A Comparison of the Effects of Natural and Artificial Aging. IEEE Journal of Photovoltaics 2020;10:173–80. https://doi.org/10.1109/JPHOTOV.2019.2947029.

[149] Abu-Naser M, Abu-Naser M. Solar Panels Cleaning Frequency for Maximum Financial Profit. Open Journal of Energy Efficiency 2017;6:80–6. https://doi.org/10.4236/OJEE.2017.63006.

[150] Hammad B, Al-Abed M, Al-Ghandoor A, Al-Sardeah A, Al-Bashir A. Modeling and analysis of dust and temperature effects on photovoltaic systems' performance and optimal cleaning frequency: Jordan case study. Renewable and Sustainable Energy Reviews 2018;82:2218–34. https://doi.org/10.1016/J.RSER.2017.08.070.

[151] Shah AH, Hassan A, Laghari MS, Alraeesi A. The Influence of Cleaning Frequency of Photovoltaic Modules on Power Losses in the Desert Climate. Sustainability 2020, Vol 12, Page 9750 2020;12:9750. https://doi.org/10.3390/SU12229750.

[152] Deb D, Brahmbhatt NL. Review of yield increase of solar panels through soiling prevention, and a proposed water-free automated cleaning solution. Renewable and Sustainable Energy Reviews 2018;82:3306–13. https://doi.org/10.1016/J.RSER.2017.10.014.

[153] Khan MU, Abbas M, Khan MM, Kousar A, Alam M, Massoud Y, et al. Modeling and design of low-cost automatic self cleaning mechanism for standalone micro PV systems. Sustainable Energy Technologies and Assessments 2021;43:100922. https://doi.org/10.1016/J.SETA.2020.100922.

[154] Ferretti N. PV Module Cleaning - Market Overview and Basics. 2018.

[155] Kumar NM, Sudhakar K, Samykano M, Sukumaran S. Dust cleaning robots (DCR) for BIPV and BAPV solar power plants-A conceptual framework and research challenges. Procedia Computer Science 2018;133:746–54. https://doi.org/10.1016/J.PROCS.2018.07.123.

[156] Alagoz S, Apak Y. Removal of spoiling materials from solar panel surfaces by applying surface acoustic waves. Journal of Cleaner Production 2020;253:119992. https://doi.org/10.1016/J.JCLEPRO.2020.119992.

[157] Kawamoto H, Guo B. Improvement of an electrostatic cleaning system for removal of dust from solar panels. Journal of Electrostatics 2018;91:28–33. https://doi.org/10.1016/J.ELSTAT.2017.12.002.

[158] Guo B, Javed W, Pett C, Wu CY, Scheffe JR. Electrodynamic dust shield performance under simulated operating conditions for solar energy applications. Solar Energy Materials and Solar Cells 2018;185:80–5. https://doi.org/10.1016/J.SOLMAT.2018.05.021.

[159] Guo B, Javed W, Khoo YS, Figgis B. Solar PV soiling mitigation by electrodynamic dust shield in field conditions. Solar Energy 2019;188:271–7. https://doi.org/10.1016/J.SOLENER.2019.05.071.

[160] Guo B, Javed W. Efficiency of electrodynamic dust shield at dust loading levels relevant to solar energy applications. IEEE Journal of Photovoltaics 2018;8:196–202. https://doi.org/10.1109/JPHOTOV.2017.2764890.

[161] Laarabi B, el Baqqal Y, Rajasekar N, Barhdadi A. Updated review on soiling of solar photovoltaic systems Morocco and India contributions. Journal of Cleaner Production 2021;311:127608. https://doi.org/10.1016/J.JCLEPRO.2021.127608.

[162] He G, Zhou C, Li Z. Review of Self-Cleaning Method for Solar Cell Array. Procedia Engineering 2011;16:640–5. https://doi.org/10.1016/J.PROENG.2011.08.1135.

[163] Zhong H, Hu Y, Wang Y, Yang H. TiO2/silane coupling agent composed of two layers structure: A super-hydrophilic self-cleaning coating applied in PV panels. Applied Energy 2017;204:932–8. https://doi.org/10.1016/J.APENERGY.2017.04.057.

[164] Conceição R, Vázquez I, Fialho L, García D. Soiling and rainfall effect on PV technology in rural Southern Europe. Renewable Energy 2020;156:743–7. https://doi.org/10.1016/J.RENENE.2020.04.119.

[165] Jiang Y, Lu L, Ferro AR, Ahmadi G. Analyzing wind cleaning process on the accumulated dust on solar photovoltaic (PV) modules on flat surfaces. Solar Energy 2018;159:1031–6. https://doi.org/10.1016/J.SOLENER.2017.08.083.

[166] Cuddihy EF. Theoretical considerations of soil retention. Solar Energy Materials 1980;3:21–33. https://doi.org/10.1016/0165-1633(80)90047-7.

[167] Conceição R, Silva HG, Fialho L, Lopes FM, Collares-Pereira M. PV system design with the effect of soiling on the optimum tilt angle. Renewable Energy 2019;133:787–96. https://doi.org/10.1016/J.RENENE.2018.10.080.

[168] Ullah A, Imran H, Maqsood Z, Butt NZ. Investigation of optimal tilt angles and effects of soiling on PV energy production in Pakistan. Renewable Energy 2019;139:830–43. https://doi.org/10.1016/J.RENENE.2019.02.114.

[169] Dubey S, Sarvaiya JN, Seshadri B. Temperature Dependent Photovoltaic (PV) Efficiency and Its Effect on PV Production in the World – A Review. Energy Procedia 2013;33:311–21. https://doi.org/10.1016/J.EGYPRO.2013.05.072.

[170] Augusto A, Herasimenka SY, King RR, Bowden SG, Honsberg C. Analysis of the recombination mechanisms of a silicon solar cell with low bandgap-voltage offset. Journal of Applied Physics 2017;121:205704. https://doi.org/10.1063/1.4984071.

[171] Dehghan M, Rahgozar S, Pourrajabian A, Aminy M, Halek FS. Techno-economic perspectives of the temperature management of photovoltaic (PV) power plants: A case-study in Iran. Sustainable Energy Technologies and Assessments 2021;45:101133. https://doi.org/10.1016/J.SETA.2021.101133.

[172] Dhouib A., Faliali S. Operating Temperatures Of Photovoltaic Panels. Energy and the Environment 1990:494–8. https://doi.org/10.1016/B978-0-08-037539-7.50085-5.

[173] Chandra S, Yadav A, Agrawal S, Chauhan DS. Material and temperature dependent performance parameters of solar PV system in local climate conditions. Materials Today: Proceedings 2020;26:878–82. https://doi.org/10.1016/J.MATPR.2020.01.124.

[174] Tripathi AK, Ray S, Aruna M. Analysis on photovoltaic panel temperature under the influence of solar radiation and ambient temperature. Proceedings of the 2021 1st International Conference on Advances in Electrical, Computing, Communications and Sustainable Technologies, ICAECT 2021 2021. https://doi.org/10.1109/ICAECT49130.2021.9392619.

[175] Nordmann T, Clavadetscher L. Understanding temperature effects of PV system performance. 3rd World Conference on Photovoltaic Energy Conversion, Osaka, Japan: 2003, p. 2243–6.

[176] Boussaid M, Belghachi A, Agroui K, Abdelaoui M, Otmani M. Solar cell degradation under open circuit condition in out-doors-in desert region. Results in Physics 2016;6:837–42. https://doi.org/10.1016/J.RINP.2016.09.013.

[177] Siecker J, Kusakana K, Numbi BP. A review of solar photovoltaic systems cooling technologies. Renewable and Sustainable Energy Reviews 2017;79:192–203. https://doi.org/10.1016/J.RSER.2017.05.053.

[178] Shukla A, Kant K, Sharma A, Biwole PH. Cooling methodologies of photovoltaic module for enhancing electrical efficiency: A review. Solar Energy Materials and Solar Cells 2017;160:275–86. https://doi.org/10.1016/J.SOLMAT.2016.10.047.

[179] Lupu AG, Homutescu VM, Balanescu DT, Popescu A. A review of solar photovoltaic systems cooling technologies. IOP Conference Series: Materials Science and Engineering 2018;444:082016. https://doi.org/10.1088/1757-899X/444/8/082016.

[180] Maleki A, Haghighi A, el Haj Assad M, Mahariq I, Alhuyi Nazari M. A review on the approaches employed for cooling PV cells. Solar Energy 2020;209:170–85. https://doi.org/10.1016/J.SOLENER.2020.08.083.

[181] Siah Chehreh Ghadikolaei S. Solar photovoltaic cells performance improvement by cooling technology: An overall review. International Journal of Hydrogen Energy 2021;46:10939–72. https://doi.org/10.1016/J.IJHYDENE.2020.12.164.

[182] Alami AH, Rabaia MKH, Sayed ET, Ramadan M, Abdelkareem MA, Alasad S, et al. Management of potential challenges of PV technology proliferation. Sustainable Energy Technologies and Assessments 2022;51:101942. https://doi.org/10.1016/J.SETA.2021.101942.

[183] Dwivedi P, Sudhakar K, Soni A, Solomin E, Kirpichnikova I. Advanced cooling techniques of P.V. modules: A state of art. Case Studies in Thermal Engineering 2020;21:100674. https://doi.org/10.1016/J.CSITE.2020.100674.

[184] Teo HG, Lee PS, Hawlader MNA. An active cooling system for photovoltaic modules. Applied Energy 2012;90:309–15. https://doi.org/10.1016/J.APENERGY.2011.01.017.

[185] Farshchimonfared M, Bilbao JI, Sproul AB. Channel depth, air mass flow rate and air distribution duct diameter optimization of photovoltaic thermal (PV/T) air collectors linked to residential buildings. Renewable Energy 2015;76:27–35. https://doi.org/10.1016/J.RENENE.2014.10.044.

[186] Almuwailhi A, Zeitoun O. Investigating the cooling of solar photovoltaic modules under the conditions of Riyadh. Journal of King Saud University - Engineering Sciences 2021. https://doi.org/10.1016/J.JKSUES.2021.03.007.

[187] Mazón-Hernández R, García-Cascales JR, Vera-García F, Káiser AS, Zamora B. Improving the electrical parameters of a photovoltaic panel by means of an induced or forced air stream. International Journal of Photoenergy 2013;2013. https://doi.org/10.1155/2013/830968.

[188] Chow TT. A review on photovoltaic/thermal hybrid solar technology. Applied Energy 2010;87:365–79. https://doi.org/10.1016/J.APENERGY.2009.06.037.

[189] Hernandez-Perez JG, Carrillo JG, Bassam A, Flota-Banuelos M, Patino-Lopez LD. Thermal performance of a discontinuous finned heatsink profile for PV passive cooling. Applied Thermal Engineering 2021;184:116238. https://doi.org/10.1016/J.APPLTHERMALENG.2020.116238.

[190] Naghavi MS, Esmaeilzadeh A, Singh B, Ang BC, Yoon TM, Ong KS. Experimental and numerical assessments of underlying natural air movement on PV modules temperature. Solar Energy 2021;216:610–22. https://doi.org/10.1016/J.SOLENER.2021.01.007.

[191] Krauter S. Increased electrical yield via water flow over the front of photovoltaic panels. Solar Energy Materials and Solar Cells 2004;82:131–7. https://doi.org/10.1016/J.SOLMAT.2004.01.011.

[192] Raju M, Sarma RN, Suryan A, Nair PP, Nižetić S. Investigation of optimal water utilization for water spray cooled photovoltaic panel: A three-dimensional computational study. Sustainable Energy Technologies and Assessments 2022;51:101975. https://doi.org/10.1016/J.SETA.2022.101975.

[193] Nižetić S, Čoko D, Yadav A, Grubišić-Čabo F. Water spray cooling technique applied on a photovoltaic panel: The performance response. Energy Conversion and Management 2016;108:287–96. https://doi.org/10.1016/J.ENCONMAN.2015.10.079.

[194] Hadipour A, Rajabi Zargarabadi M, Rashidi S. An efficient pulsed- spray water cooling system for photovoltaic panels: Experimental study and cost analysis. Renewable Energy 2021;164:867–75. https://doi.org/10.1016/J.RENENE.2020.09.021.

[195] Bahaidarah H, Subhan A, Gandhidasan P, Rehman S. Performance evaluation of a PV (photovoltaic) module by back surface water cooling for hot climatic conditions. Energy 2013;59:445–53. https://doi.org/10.1016/J.ENERGY.2013.07.050.

[196] Velmurugan K, Kumarasamy S, Wongwuttanasatian T, Seithtanabutara V. Review of PCM types and suggestions for an applicable cascaded PCM for passive PV module cooling under tropical climate conditions. Journal of Cleaner Production 2021;293:126065. https://doi.org/10.1016/J.JCLEPRO.2021.126065.

[197] Chandel SS, Agarwal T. Review of cooling techniques using phase change materials for enhancing efficiency of photovoltaic power systems. Renewable and Sustainable Energy Reviews 2017;73:1342–51. https://doi.org/10.1016/J.RSER.2017.02.001.

[198] Michael Joseph Stalin P, Prasad KS, Kumar KP, Hemadri G, Rajesh M, Kumar KP. Performance improvement of solar PV through the thermal management using a nano-PCM. Materials Today: Proceedings 2021. https://doi.org/10.1016/J.MATPR.2021.09.111.

[199] Stropnik R, Stritih U. Increasing the efficiency of PV panel with the use of PCM. Renewable Energy 2016;97:671–9. https://doi.org/10.1016/J.RENENE.2016.06.011.

[200] Tang X, Quan Z, Zhao Y, Tang X, Quan Z, Zhao Y. Experimental Investigation of Solar Panel Cooling by a Novel Micro Heat Pipe Array. Energy and Power Engineering 2010;2:171–4. https://doi.org/10.4236/EPE.2010.23025.

[201] Moshfegh H, Eslami M, Hosseini A. Thermoelectric Cooling of a Photovoltaic Panel. Green Energy and Technology 2018:625–34. https://doi.org/10.1007/978-3-319-89845-2_44.

[202] Salehi R, Jahanbakhshi A, Reza Golzarian M, Khojastehpour M. Evaluation of solar panel cooling systems using anodized heat sink equipped with thermoelectric

module through the parameters of temperature, power and efficiency. Energy Conversion and Management: X 2021;11:100102. https://doi.org/10.1016/J.ECMX.2021.100102.

[203] Zhu L, Raman AP, Fan S. Radiative cooling of solar absorbers using a visibly transparent photonic crystal thermal blackbody. Proceedings of the National Academy of Sciences 2015;112:12282–7. https://doi.org/10.1073/PNAS.1509453112.

[204] Zhao B, Hu M, Ao X, Xuan Q, Pei G. Comprehensive photonic approach for diurnal photovoltaic and nocturnal radiative cooling. Solar Energy Materials and Solar Cells 2018;178:266–72. https://doi.org/10.1016/J.SOLMAT.2018.01.023.

[205] Liu Z, Li Z, Xie D, Wu H. Unsteady characteristic and flow mechanism of a scroll compressor in small-scale compressed air energy storage system. Journal of Energy Storage 2022;51:104368. https://doi.org/10.1016/J.EST.2022.104368.

[206] Peng B, Zhu B, Lemort V, Bin P, Bingguo Z. Theoretical and Experimental Analysis of Scroll Expander. 23rd International Compressor Engineering Conference, Purdue: 2016.

[207] Air Compressor Works Inc. Compressor Basics: Scroll Compressors 2017. https://aircompressorworks.com/compressor-basics-scroll/ (accessed May 25, 2022).

[208] Li D, King M, Dooner M, Guo S, Wang J. Study on the cleaning and cooling of solar photovoltaic panels using compressed airflow. Solar Energy 2021;221:433–44. https://doi.org/10.1016/J.SOLENER.2021.04.050.

[209] King M, Li D, Dooner M, Ghosh S, Nath Roy J, Chakraborty C, et al. Mathematical Modelling of a System for Solar PV Efficiency Improvement Using Compressed Air for Panel Cleaning and Cooling. Energies 2021, Vol 14, Page 4072 2021;14:4072. https://doi.org/10.3390/EN14144072.

[210] King M, Li D, Dooner M, Wang J. Modelling and control of the charging process of a PV-compressed air system for efficiency improvement from panel cleaning and cooling. 26th International Conference on Automation and Computing (ICAC) 2021:1–6. https://doi.org/10.23919/ICAC50006.2021.9594199.

[211] Nguyen XH, Nguyen MP. Mathematical modeling of photovoltaic cell/module/arrays with tags in Matlab/Simulink. Environmental Systems Research 2015 4:1 2015;4:1–13. https://doi.org/10.1186/S40068-015-0047-9.

[212] Humada AM, Hojabri M, Mekhilef S, Hamada HM. Solar cell parameters extraction based on single and double-diode models: A review. Renewable and Sustainable Energy Reviews 2016;56:494–509. https://doi.org/10.1016/J.RSER.2015.11.051.

[213] Olukan TA, Emziane M. A Comparative Analysis of PV Module Temperature Models. Energy Procedia 2014;62:694–703. https://doi.org/10.1016/J.EGYPRO.2014.12.433.

[214] Jakhrani AQ, Jakhrani AQ, Othman AK, Rigit ARH, Samo SR. Comparison of Solar Photovoltaic Module Temperature Models. World Applied Sciences Journal 2011;14:1–08.

[215] Holman JP, Lloyd J. Heat Transfer. 10th ed. McGraw-Hill; 2010.

[216] Moutinho HR, Jiang CS, To B, Perkins C, Muller M, Al-Jassim MM, et al. Adhesion mechanisms on solar glass: Effects of relative humidity, surface roughness, and particle shape and size. Solar Energy Materials and Solar Cells 2017;172:145–53. https://doi.org/10.1016/J.SOLMAT.2017.07.026.

[217] Leite FL, Bueno CC, da Róz AL, Ziemath EC, Oliveira ON. Theoretical Models for Surface Forces and Adhesion and Their Measurement Using Atomic Force Microscopy. International Journal of Molecular Sciences 2012, Vol 13, Pages 12773-12856 2012;13:12773–856. https://doi.org/10.3390/IJMS131012773.

[218] Brambilla S, Speckart S, Brown MJ. Adhesion and aerodynamic forces for the resuspension of non-spherical particles in outdoor environments. Journal of Aerosol Science 2017;112:52–67. https://doi.org/10.1016/J.JAEROSCI.2017.07.006.

[219] Crowley JM. Simple Expressions for Force and Capacitance for a Conductive Sphere near a Conductive Wall. ESA Annual Meeting on Electrostatics, 2008, p. D1.

[220] Hinds WC. Aerosol Technology: Properties, Behavior, and Measurement of Airborne Particles. 2nd ed. Wiley; 1999.

[221] Haraguchi Y, Michioka C, Ueda H, - al, Zhao X, Cuong Nguyen M, et al. Definitive equations for the fluid resistance of spheres. Proceedings of the Physical Society 1945;57:259. https://doi.org/10.1088/0959-5309/57/4/301.

[222] Ahmadi G, Guo S. Bumpy Particle Adhesion and Removal in Turbulent Flows Including Electrostatic and Capillary Forces. The Journal of Adhesion 2007;83:289–311. https://doi.org/10.1080/00218460701239174.

[223] Bird JO, Chivers PJ. Friction. Newnes Engineering and Physical Science Pocket Book 1993:235–7. https://doi.org/10.1016/B978-0-7506-1683-6.50031-X.

[224] Burdick GM, Berman NS, Beaudoin SP. Hydrodynamic particle removal from surfaces. Thin Solid Films 2005;488:116–23. https://doi.org/10.1016/J.TSF.2005.04.112.

[225] Reeks MW, Hall D. Kinetic models for particle resuspension in turbulent flows: theory and measurement. Journal of Aerosol Science 2001;32:1–31. https://doi.org/10.1016/S0021-8502(00)00063-X.

[226] Emhemed AAA, bin Mamat R. Modelling and Simulation for Industrial DC Motor Using Intelligent Control. Procedia Engineering 2012;41:420–5. https://doi.org/10.1016/J.PROENG.2012.07.193.

[227] Wang J, Yang L, Luo X, Mangan S, Derby JW. Mathematical modeling study of scroll air motors and energy efficiency analysis - Part I. IEEE/ASME Transactions on Mechatronics 2011;16:112–21. https://doi.org/10.1109/TMECH.2009.2036608.

[228] Wang J, Luo X, Yang L, Shpanin LM, Jia N, Mangan S, et al. Mathematical modeling study of scroll air motors and energy efficiency analysis - Part II. IEEE/ASME Transactions on Mechatronics 2011;16:122–32. https://doi.org/10.1109/TMECH.2009.2036607.

[229] Wang DJD, Pu J, Moore PR, Wang J. Modelling study, analysis and robust servocontrol of pneumatic cylinder actuator systems. IEE Proceedings - Control Theory and Applications 2001;148:35–42. https://doi.org/10.1049/ip-cta:20010238.

[230] Li Yang. Modelling and Energy Efficiency Analysis of Scroll Type Air Motor. University of Liverpool, 2008.

[231] Kushnir R, Ullmann A, Dayan A. Thermodynamic Models for the Temperature and Pressure Variations Within Adiabatic Caverns of Compressed Air Energy Storage Plants. Journal of Energy Resources Technology 2012;134. https://doi.org/10.1115/1.4005659.

[232] White FM. Fluid Mechanics Seventh Edition. McGraw-Hill 2011:826.

[233] Linares-Flores J, Reger J, Sira-Ramirez H. Load torque estimation and passivity-based control of a boost-converter/DC-motor combination. IEEE Transactions on Control Systems Technology 2010;18:1398–405. https://doi.org/10.1109/TCST.2009.2037809.

[234] Tomson T. Fast dynamic processes of solar radiation. Solar Energy 2010;84:318–23. https://doi.org/10.1016/J.SOLENER.2009.11.013.

[235] Mumtaz F, Zaihar Yahaya N, Tanzim Meraj S, Singh B, Kannan R, Ibrahim O. Review on non-isolated DC-DC converters and their control techniques for renewable energy applications. Ain Shams Engineering Journal 2021;12:3747–63. https://doi.org/10.1016/J.ASEJ.2021.03.022.

[236] Onat N. Recent developments in maximum power point tracking technologies for photovoltaic systems. International Journal of Photoenergy 2010;2010. https://doi.org/10.1155/2010/245316.

[237] Javed W, Guo B, Figgis B. Modeling of photovoltaic soiling loss as a function of environmental variables. Solar Energy 2017;157:397–407. https://doi.org/10.1016/J.SOLENER.2017.08.046.

[238] Figgis B, Ennaoui A, Ahzi S, Rémond Y. Review of PV soiling particle mechanics in desert environments. Renewable and Sustainable Energy Reviews 2017;76:872–81. https://doi.org/10.1016/J.RSER.2017.03.100.

[239] Sulaiman SA, Hussain HH, Leh NSHN, Razali MSI. Effects of Dust on the Performance of PV Panels. International Journal of Mechanical and Mechatronics Engineering 2011;5:2021–6.

[240] Sulaiman SA, Singh AK, Mokhtar MMM, Bou-Rabee MA. Influence of Dirt Accumulation on Performance of PV Panels. Energy Procedia 2014;50:50–6. https://doi.org/10.1016/J.EGYPRO.2014.06.006.

[241] Rao RR, Mani M, Ramamurthy PC. An updated review on factors and their inter-linked influences on photovoltaic system performance. Heliyon 2018;4:e00815. https://doi.org/10.1016/J.HELIYON.2018.E00815.

[242] Mineralogy Database. Talc Mineral Data. 2022 n.d. http://webmineral.com/data/Talc.shtml#.YD%209wqmj7SUn (accessed May 1, 2022).

Appendix A – Technical Characteristics of Current CAES Plants

Table A-1. Key technical characteristics of current conventional CAES facilities

	Huntorf, Germany	McIntosh, AL, USA
Operator	Uniper Kraftweke GmbH	Power South Energy Cooperative
Year Operational	1978	1991
Deliverable Power [MW]	290	110
Discharge Time [hr]	2	26
Efficiency [%]	29	36
Pressure [bar]	48-66	<76
Cavern Type	Two solution mined salt caverns	Single solution mined salt caverns

Appendix B – Results from CAES Potential in India Assessment

Table B-1. Result of analysis of CAES and renewable electricity integration in India (by 1° grid cells)

State	Local Latitude [°N]	Local Longitude [°E]	CAES Suitable Area [km^2]	Annual Capacity Factor (Solar)	Annual Capacity Factor (Wind)	Normalised Area Factor	Normalised Solar Factor	Normalised Wind Factor	Solar-CAES Factor	Wind-CAES Factor	Potential Factor
Madhya Pradesh	26.5	78.5	4974.9	0.193	0.090	1.00	0.94	0.18	0.935	0.185	0.173
Uttar Pradesh	25.5	78.5	4139.7	0.194	0.105	0.83	0.94	0.22	0.780	0.179	0.168
Uttar Pradesh	25.5	79.5	3809.4	0.189	0.094	0.77	0.91	0.19	0.700	0.148	0.136
Uttar Pradesh	25.5	83.5	3597.6	0.182	0.094	0.72	0.88	0.19	0.637	0.140	0.123
Uttar Pradesh	25.5	82.5	2599.2	0.183	0.098	0.52	0.88	0.20	0.462	0.105	0.093
Uttar Pradesh	25.5	81.5	2678.0	0.185	0.091	0.54	0.90	0.19	0.483	0.101	0.090
Uttar Pradesh	25.5	80.5	1680.7	0.186	0.091	0.34	0.90	0.19	0.304	0.063	0.057
West Bengal	23.5	87.5	928.3	0.175	0.088	0.19	0.85	0.18	0.158	0.034	0.028
Jharkhand	22.5	86.5	1090.8	0.174	0.068	0.22	0.84	0.14	0.185	0.031	0.026
Madhya Pradesh	25.5	77.5	448.4	0.197	0.131	0.09	0.95	0.27	0.085	0.024	0.023
Uttarakhand	29.5	79.5	568.6	0.204	0.068	0.11	0.99	0.14	0.081	0.016	0.016
Uttar Pradesh	26.5	79.5	442.6	0.189	0.090	0.09	0.92	0.18	0.113	0.016	0.015
Jharkhand	24.5	87.5	419.5	0.177	0.087	0.08	0.85	0.18	0.072	0.015	0.013
Rajasthan	29.5	74.5	370.6	0.197	0.073	0.07	0.95	0.15	0.071	0.011	0.011
Jammu and Kashmir	32.5	75.5	394.0	0.193	0.052	0.08	0.93	0.11	0.074	0.008	0.008
Punjab	33.5	73.8	323.7	0.202	0.056	0.06	0.98	0.11	0.041	0.008	0.007

Rajasthan	26.5	77.5	186.0	0.194	0.100	0.04	0.94	0.21	0.035	0.008	0.007
Jharkhand	24.5	83.5	229.3	0.186	0.082	0.05	0.90	0.17	0.063	0.007	0.007
Jammu and Kashmir	32.8	74.7	303.7	0.193	0.040	0.06	0.94	0.08	0.057	0.005	0.005
Punjab	30.5	74.5	228.1	0.191	0.051	0.05	0.93	0.10	0.042	0.005	0.004
Gujarat	23.6	68.7	12.2	0.201	0.487	0.00	0.97	1.00	0.002	0.002	0.002
Tripura	23.6	91.6	242.0	0.176	0.018	0.05	0.85	0.04	0.041	0.002	0.002
Rajasthan	29.4	73.6	38.3	0.198	0.083	0.01	0.96	0.17	0.475	0.001	0.001
Nagaland	26.5	94.5	2814.6	0.173	0.001	0.57	0.84	0.00	0.007	0.001	0.001
Jammu and Kashmir	33.5	74.5	7.5	0.207	0.069	0.00	1.00	0.14	0.019	0.000	0.000
Assam	27.5	94.5	126.0	0.160	0.003	0.02	0.78	0.01	0.001	0.000	0.000
Meghalaya	25.5	92.5	23.9	0.182	0.008	0.00	0.88	0.02	0.004	0.000	0.000
Nagaland	25.5	93.5	476.9	0.185	0.000	0.10	0.90	0.00	0.086	0.000	0.000
Assam	27.5	95.5	36.1	0.163	0.000	0.01	0.79	0.00	0.033	0.000	0.000
Punjab	30.5	76.5	2.1	0.192	0.081	0.00	0.93	0.17	0.005	0.000	0.000
Jammu and Kashmir	33.0	73.9	31.5	0.000	0.000	0.01	0.00	0.00	0.000	0.000	0.000
Nagaland	26.7	95.2	203.0	0.169	0.000	0.04	0.82	0.00	0.000	0.000	0.000

Appendix C – List of Test Rig Hardware

Table C-1. List of hardware in test rig

Item	Specification	Quantity
Low pressure air tank	Sealey SA200T 200 L	1
High pressure air tank	Abbott & Co. (Newark) Ltd. A59044 340 L	1
Booster compressor	Kaeser Kompressoren NB60.1	1
4000 K LED bulb	VTAC VT-247D	100
2700 K LED bulb	Integral LED ILGU10DC075	69
Heat Lamp	Philips Incandescent 230V PAR38	12
Proportional pressure regulator	FESTO MPPE-3-1/4-10-010-B	1
Manual pressure regulator	FESTO MS6-LFR-1/2-D8-E-R-M-AS-Z	1
Programmable electronic load	Höcherl & Hackl ZSAC426	1
DC power supply	digimess® Concept series SM10010	1
Thermocouples	LABFACILITY Z2-K-1M (IEC)	17
Pressure transducer	RS-PRO 797-5037	2
Pressure transducer	FESTO SPAW-P25R-612M-2PV-M12	1
Flow sensor	FESTO MS6-SFE-F5-P2U-M12	1
Air nozzles	Silvent 973F	2

Table C-2. List of control platform modules

Item	Specification	Quantity
Chassis	NI PXIe - 1082	1
Embedded controller	NI PXIe - 8133	1
Multifunction DAQ module	NI PXIe - 6358	1
Thermocouple module	NI TB - 4353	1
Digital multimeter module	NI PXI- 4065	1
AO module	NI PXIe - 6738	1

Appendix D – Parameters Used in Model Validation and System Study

Table D-1. PV panel parameters and constants

Parameter		**Value**	**Unit**
Short-circuit current	I_{sc}	2.15	[A]
Short-circuit temperature coefficient	k_i	0.023	[%·°C^{-1}]
Cell reference temperature	T_{ref}	298	[K]
Electron charge constant	q	1.60×10^{-19}	[C]
Semiconductor bandgap energy	E_{g0}	1.12	[eV]
Diode ideality factor	n	8.0	[-]
Boltzmann constant	K_b	1.38×10^{-23}	[m^2·kg·s^{-2}·K^{-1}]
Open-circuit voltage	V_{oc}	75	[-]
Cells in series connection	N_s	28	[V]
Series resistance	R_s	1.2	[Ω]
Shunt resistance	R_{sh}	800	[Ω]
Panel width	d_p	0.61	[m]
Panel length	l_p	1.22	[m]
Panel depth[11]		0.01	[m]
Panel density[11]		2329	[kg m^{-3}]
Panel specific heat	c_{pp}	0.7	[J kg^{-1} K^{-1}]
Nominal conversion efficiency	ϵ	0.131	[-]
Gravitational acceleration	g	9.81	[m·s^{-2}]

---

[11] Used for determining panel mass

Figures D-1 and D-2 illustrate the comparison between the characterised panel under standard conditions of 1000 Wm^{-2} and 25°C with the PV parameters implemented for the modelling study.

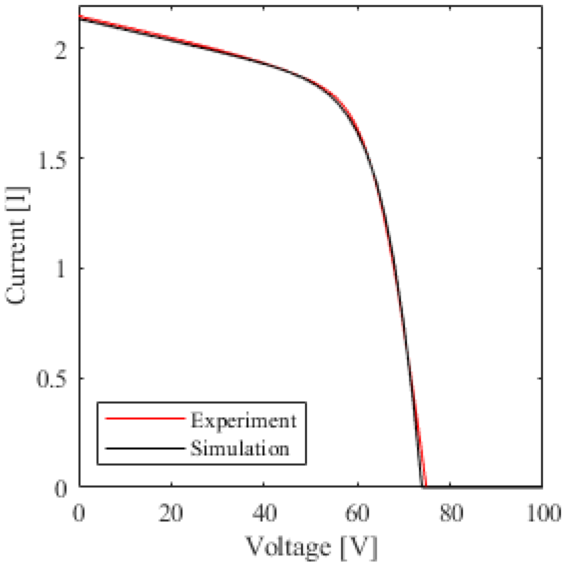

Figure D-1. I-V comparison of PV panel and model parameters

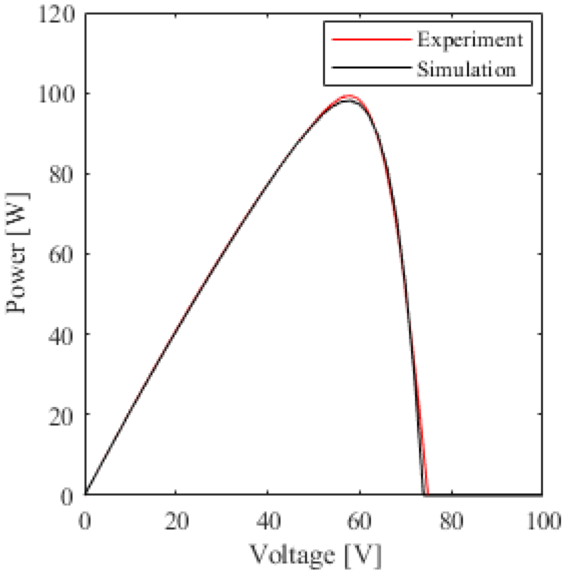

Figure D-2. P-V comparison of PV panel and model parameters

Table D-2. Panel soiling model parameters

Parameter		Value	Unit
Hamaker constant	A_h	7×10^{-20}	[J]
Particle radius	R_p	10×10^{-6}	[m]
Closest distance between surfaces	H_0	0.3×10^{-9}	[m]
Vacuum permittivity	ϵ_0	8.854×10^{-12}	[F·m^{-1}]
Wall coefficient	Γ	1.84	[-]
Near wall correction factor	f	1.7009	[-]
Molecular mean free path	λ	0.07×10^{-6}	[m]
Wall correction factor	f_m	0.944	[-]
Particle material density	ρ_d	2700	[kg·m^{-3}]
Coefficient of friction	μ	0.4	[-]
Absorption efficiency	E_{abs}	0.02	[m^2·g^{-1}]
Particle up-scatter fraction	β_f	0.02	[-]
Scattering efficiency	E_{scat}	1.0	[m^2·g^{-1}]

Table D-3. Air system parameters

Parameter		Value	Unit
Rotor inertia	J_m	0.00025	[kg·m^2]
Viscous damping factor	b	10^{-4}	[N·m·s]
Motor torque constant	K_t	0.05	[N·m·A^{-1}]
Circuit inductance	L_m	1.5×10^{-3}	[H]
Motor resistance	R_m	0. 5	[Ω]
Electromotive force constant	K_e	0.05	[V·s·rad^{-1}]
Boost converter inductance	L_b	10^{-4}	[H]

Boost converter capacitance	C_b	10^{-6}	[F]
Boost converter resistance	R_b	5	[Ω]
Motor orbit radius	r	5.5×10^{-3}	[m]
Initial radius of curvature	ρ_0	9.5×10^{-3}	[m]
Opening curvature value	k	3.2×10^{-3}	[m]
Total scroll volume	V_{total}	17.4×10^{-4}	[m^3]
Scroll blade height	z	0.10	[m]
Ratio of specific heats	γ	1.4	[-]
Discharge coefficient	C_d	0.8	[-]
Discharge coefficient	C_0	0.404	[-]
Compressor outlet area	A_{out}	1.13×10^{-4}	[m^2]
Discharge coefficient	C_r	0.5283	[-]
Discharge coefficient	C_k	3.864	[-]
Tank volume	V_t	0.2	[m^3]
Isochoric specific heat	c_v	0.718	[$J \cdot kg^{-1} \cdot K^{-1}$]
Specific heat of air in tank	$C_{p,air}$	1.006	[$J \cdot kg^{-1} \cdot K^{-1}$]
Nozzle outlet dimension		$22 \times 2 \times 0.001 \times 0.0035$	[mm]
Panel width	$d_{p,}$	0.62	[m]